A 64 CHANNEL TRANSMIT SYSTEM

FOR SINGLE ECHO ACQUISITION MRI

A Dissertation

by

KE FENG

Submitted to the Office of Graduate Studies of
Texas A&M University
in partial fulfillment of the requirements for the degree of

DOCTOR OF PHILOSOPHY

August 2011

Major Subject: Electrical Engineering

A 64 CHANNEL TRANSMIT SYSTEM

FOR SINGLE ECHO ACQUISITION MRI

A Dissertation

by

KE FENG

Submitted to the Office of Graduate Studies of
Texas A&M University
in partial fulfillment of the requirements for the degree of

DOCTOR OF PHILOSOPHY

Approved by:

Chair of Committee,	Steven M. Wright
Committee Members,	Mary Preston McDougall
	Jim Xiuquan Ji
	Laszlo B. Kish
Head of Department,	Costas N. Georghiades

August 2011

Major Subject: Electrical Engineering

ABSTRACT

A 64 Channel Transmit System
for Single Echo Acquisition MRI. (August 2011)

Ke Feng, B.S., Shandong University;
M.S., Texas A&M University
Chair of Advisory Committee: Dr. Steven M. Wright

Magnetic Resonance Imaging (MRI) is considered as a slow imaging technique. Various approaches to accelerate MRI imaging have been explored by researchers in the past decades. Earlier gradient based methods have reached the safety limit. Parallel receiving techniques achieve accelerations by reducing phase encoding steps. Among these methods, SEA Imaging achieved the highest possible acceleration by completely eliminating phase encoding. However, SEA imaging is limited to thin planar slices above the array due to the correction needed for the inherent phase cancellation caused by voxel-sized coils. A phase compensation gradient pulse is used for this correction in SEA imaging. This phase compensation is dependent on slice position and thickness as well as the orientation of the array elements, placing stringent restrictions on SEA imaging, limiting its applications. Converting the SEA system into Transmit / Receive (T/R) mode, which is the main purpose of this study, eliminates the requirement for phase compensation gradient because phase departed during transmit is refocused during receiving. Independent amplitude and phase control of RF pulse for each coil of a SEA array is achieved using a low cost scalable parallel transmit system design. The first 64-channel parallel transmitter for MRI in the world is constructed and tested. Software is also developed to control the phase and amplitude of all the 64 channels of RF excitation pulses independently through National Instruments DAQ system. The system consists of vector modulators controlled by digital controlled potentiometers, two-stage amplifiers and T/R switches on the transmit side. All these are combined with newly designed and constructed preamplifiers and the existing 64-channel parallel receivers on the receive side, leading to the only 64-channel parallel T/R system available for MRI. As a bonus, the system can be easily updated to full Transmit SENSE capability. Furthermore, simulations and images are done to synthesize transmit patterns thanks to the large channel count. Testing results show that the system is capable of 100W per channel simultaneous transmission. Using this system, transmit field can be synthesized by varying the phase and amplitude across channel without traditionally required complicated pulse sequences involving simultaneous RF and gradient fields. Curved slice excitation has conventionally been considered a difficult task for MRI, achievable only through complicated pulses sequences. Using this system and flexible array wrapped around the subject to be imaged, the system is able to excite curved slice using one shot. TR images indicate that the system is capable of high speed surface imaging at 200 frames per second following the surface of a flexible SEA array coil which has not been achieved using other methods in MRI.

DEDICATION

I dedicate this dissertation to my family, my loving wife, Rumei Zhao, and our sons, Dizhe Feng and Dihan Feng, for always being the source of inspiration whenever needed. My father, Xiaojun Feng, my mother, Yuezhi Zhang, and my brother Xuming Feng are always on my side and offer any help they can to provide constant encouragement. During the semesters without an assistantship, I got financial support from you using your hard earned money.

衷心感谢我所有的家人，只有你们的支持和帮助才是无私的，那一切已经无法用语言描述

ACKNOWLEDGEMENTS

I wish to thank each person who has supported me and contributed to make this work possible. There is not enough room to list the names here, let alone list the generous help and offers I received in details. A few of the most significant have been highlighted in the paragraphs below.

I would first like to thank my committee chair, Dr. Steven M. Wright, of the Department of Electrical and Computer Engineering at Texas A&M University. Dr. Wright served as the chair of my doctoral committee and was my principal advisor. Without his guidance and support throughout the course of this research, it would have been impossible to conduct the research described in these pages. Dr. Mary P. McDougall, Dr. Jim X. Ji and Dr. Laszlo B. Kish have been on my committee and always been responsive to questions and requests.

I thank all my colleagues at the Magnetic Resonance Systems Laboratory who have provided various help and assistance during the course of this research. In particular, the author wishes to acknowledge John C. Bosshard for all kinds of help and ideas whenever needed, Neal A. Hollingsworth for providing brainpower and hard work in the design and testing of the system, Chieh-Wei Chang and Katy L. Moody for exertion in the assembly of the system, and everyone else who has made my time at Texas A&M University a great experience. I also want to extend my gratitude to the

National Institute of Health for funding this project, with part of the money going toward my research assistantship for several semesters. Without any of you, this research would have been impossible.

NOMENCLATURE

ADC	Analog-to-Digital Converter
COM	Component Object Model
DAC	Digital-to-Analog Converter
DANTE	Delays Alternating with Nutation for Tailored Excitation
DAQ	Data Acquisition
DC	Direct Current
DIP	Dual In-line Package
GRAPPA	Generalized Autocalibrating Partially Parallel Acquisitions
GPIB	General Purpose Interface Bus
GUI	Graphic User Interface
I/O	Input / Output
LPF	Low Pass Filter
MR	Magnetic Resonance
MRI	Magnetic Resonance Imaging
MRSL	Magnetic Resonance Systems Laboratory
NI	National Instruments
pTx	Parallel Transmit
RF	Radio Frequency
R/O	Receive Only
SEA	Single Echo Acquisition

SENSE	Sensitivity Encoding
SMASH	Simultaneous Acquisition of Spatial Harmonics
SNR	Single to Noise Ratio
T/R	Transmit / Receive
VB	Visual Basic
VNA	Vector Network Analyzer

TABLE OF CONTENTS

Page

CHAPTER

LIST OF FIGURES

Page

Page

LIST OF TABLES

CHAPTER I

INTRODUCTION

Magnetic Resonance Imaging (MRI) has been widely used in clinical diagnostics due to its non-invasive and non-ionizing nature. High speed MRI has been of interest in the community for decades [1-9]. On one side, high speed means less time for a patient to be in the scanner, providing patient comfort and more throughput from the equipment and hospital service team. On the other side, high speed imaging provides additional capabilities, conquering problems such as motion blurs and ultimately made dynamic MRI possible [1, 3]. In this chapter, a brief introduction to high speed MRI, followed by a specific method called SEA [10-12] is briefly introduced. Its advantages and limitations are briefly stated. A solution to lift the limitation is given, which became the motivation and the content of this research. Later, a brief outline of this dissertation is given.

I.1 High Speed MRI

MRI is traditionally considered as a low speed imaging technique because of its “serial” nature. To acquire an image with resolution of M×N pixels with traditional MRI sequence, M or N phase encoding steps are required. A single k-space line is achieved at

---

This dissertation follows the style of *IEEE Transactions on Biomedical Engineering*.

a time, followed by a usually rather long time interval before the next k-space line is acquired. This is repeated until the full set is acquired. Faster pulse sequences have been developed, pushing to the limit of hardware systems. However, safety concerns put stringent limitations on this approach. Problems of peripheral nerve stimulations[13, 14] have been observed, preventing stronger gradient from clinical applications.

It is hard to give a number, saying that is the maximum speed possible, because there are many hardware configurations, pulse sequences and imaging parameters to choose from. It is often a matter of tradeoffs. One can often have higher speed by giving up either resolution or Signal to Noise Ratio (SNR). By carefully designing the pulse sequence and using an acceleration factor of 4, Tsao et al were able to do get temporal resolution of as high as 26mS[1]. This is fast enough that can eliminates breath holding, but when it comes to higher speed event, motion blurring is still there. This is analogous to traditional photographs using an optical camera. Acquiring one frame in 26mS indicates a shutter speed that is a little bit slower than 1/40 of a second. Capturing photos of moving objects with moderate velocity usually require at least a shutter speed of 1/125 of a second.

As a work around, worth noticing is that MRI has been successfully used to capture objects in recurrent motions by synchronizing the acquisition to the motion, acquiring a single k-space line at a recurrence of the motion using various gating system, such as [15, 16]. However, these methods are limited to recurrent event, such as breath or heart beating. Imaging of non-recurrent events, such as tissue ablation or nerve stimulation, still require the acquisition of each time frame to be short enough to “freeze” the motion of the subject.

In the past decade, parallel receiving techniques[5-8] became standard routines for clinical and research MRI imaging. The serial nature of MRI is partially changed to a parallel mode. These techniques achieve accelerations by reducing number of phase encoding steps by a number, called acceleration factor, which is typically 2 to 4, or in some special cases, 6 to 8[4]. The phase encoding steps is reduced by a factor of this number. Tsao’s research mentioned in the above section actually already uses a 4-fold acceleration factor.

The potential for using MRI to image extremely rapid, non-periodic or one-time events, which require higher speed than ever needed before, is of growing interest. Figure 1.1 shows different biological processes and the time scale. Note that the shutter speed cannot actually be on the same order as the biological process. For example, Turbo-Flash can be done in less than a second while heart beat period is about 1 second. Turbo-Flash still cannot be used to “freeze” the movement of heart beat. The shutter speed must be much higher than the biological process. Otherwise, motion blurs will be unavoidable.

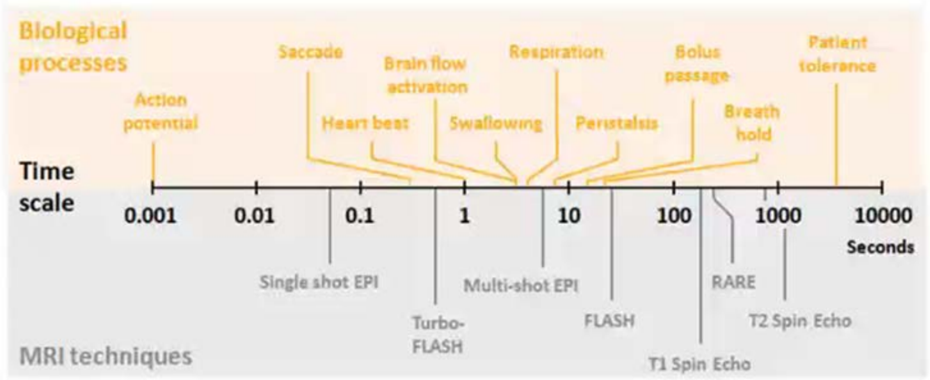

Figure 1.1 Biological Process Time Scales. Figure is reproduced from: http://airto.bmap.ucla.edu/BMCweb/SharedCode/SpeedLimit/SpeedLimit.html

Notably, the discovery of Blood-Oxygen-Level Dependence (BOLD) functional MRI (fMRI) imaging made MRI the choice of modality for neuroimaging. The full time course of a BOLD response to a briefly presented stimulus lasts about 15 seconds[17]. Illustration the BOLD signal evolution process requires dynamic MRI that is at least sub-second. The potential to study millisecond rate kinematics with MRI would open up a variety of potential applications. Turbulent flow in stenotic vessels and microfluidic lab-on-a-chip mixers are just a few examples of possible applications for sub-millisecond MRI.

I.2 Current R/O SEA Technology – Advantages and Limitations

The extreme of all parallel receiving methods is perhaps a technique developed by Wright et al, called Single Echo Acquisition (SEA)[11, 12, 18, 19]. In SEA imaging, the number of phase encoding steps is reduced to perhaps the minimum number possible, one. An image is reconstructed from a single echo received simultaneously by all elements of a 64-channel array[20], completely eliminating phase encoding. More details of this method will be discussed in Chapter II of this dissertation. Using SEA MRI, a frame rate of 1000 images per second has been successfully demonstrated[21].

High speed SEA imaging brings new possibilities for MRI, allowing imaging of dynamic processes which had previously been impossible. However, its reliance on phase compensation gradient limits the coil to a planar configuration [19, 22, 23], which constrains this potentially more powerful method from being used routinely. This restriction will be further elucidated in Chapter II of this dissertation.

Transforming the traditional SEA imaging method into a transmit / receive (T/R) mode makes it insensitive to the orientation of the coils and with the ability to excite and image curved slices parallel to a conformable array, only limitation would be that it should stay linear in the frequency encoding direction, which is normally the same direction as the main gradient field. Details will be covered in Chapter II of this dissertation. To clarify the difference of traditional SEA imaging with the one developed in this study, the text will later use two different names, Receive Only SEA (R/O SEA) and Transmit / Receive SEA (TR SEA).

I.3 Dissertation Organization

Because R/O SEA provides important backgrounds in TR SEA, it is summarized in Chapter II. The basic theory is first given. The requirement for phase compensation gradient is then explained, which is one of the main limiting factors for R/O SEA. The solution to the problem used in the research was operating SEA in TR mode. The elimination of phase compensation using TR mode for a single channel was verified using MR images.

The hardware system for the TR SEA consists of both the receiver side and the transmitter side. This dissertation focuses on the transmitter side because the receiver side had been covered in [24, 25]. A big picture of the transmitter system design will be laid out in Chapter III, followed by details of each part. The receiver side has been previously designed and constructed but will also be briefly introduced.

The software part was briefly summarized in Chapter IV, which is broken into two parts for two different kinds of applications. The first part covers the software for TR SEA which is the main focus of this dissertation. The second part briefly covers the software used for transmit SENSE.

To predict the transmit pattern of the array, a MATLAB based static simulation is provided which is described in Chapter V. Actual MR imaging results are shown for verification purposes.

With the system built, calibration, testing and verification are necessary, which are covered in Chapter VI. A few programs are written to automate the processes. Theory and results are shown.

A few unique applications of the large channel count transmit array are shown in Chapter VII. Because of the unique high channel count, some previously impossible methods have been explored.

Chapter VIII gives discussions of possible improvements and potential applications of the system and technique.

CHAPTER II

REVIEW OF R/O SEA AND BEYOND

R/O SEA was initially investigated by Wright et al[12, 18, 19]. A lot of work in the area has been performed afterwards, exploring its applications in flow[26, 27], elastography[28, 29] and pushing to even higher speed of 1000 frames per second[21]. This section will give a briefly introduction to R/O AEA. The introduction mainly focuses on the part that is closely related to TR SEA. For more details, the reader is encouraged to read [11, 12, 18-23, 26, 27, 30-34].

II.1 Basic Theory

A commonly seen gradient echo pulse sequence is shown in Figure 2.1. The number of phase encoding steps is the main limiting factor accounting for the time consumption for imaging. Between each echo is a repetition time, TR. While TR is relatively short, especially in gradient echo sequences, it needs to be repeated by the same number as the resolution of the image in the phase encoding direction. Various methods have been explored to receive multiple echoes using complex trajectory, such as fast spin echo, echo planar imaging (EPI), spiral EPI. Problem of these approaches were mainly from Peripheral nerve stimulations. Various parallel imaging methods uses reduced phase encoding steps instead to achieve acceleration without using stronger gradients.

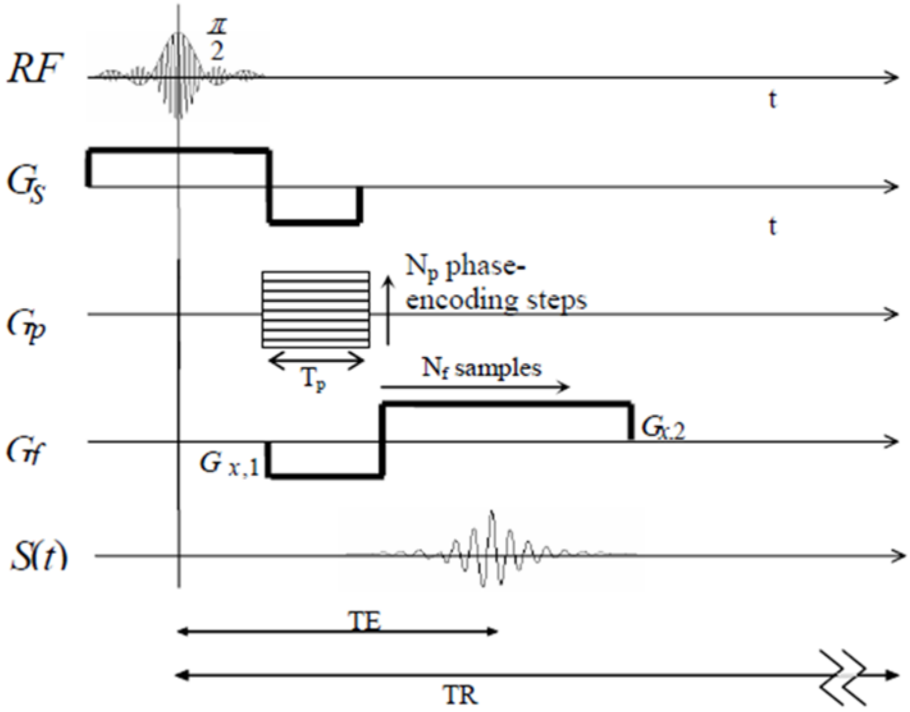

Figure 2.1 A Common Gradient Echo Pulse Sequence. Figure is reproduced from [31]. In the drawing, G_s is for slice selection gradient, G_p for phase encoding gradient table G_f is for frequency encoding. An N_p by N_f image requires N_p echoes to be sampled, each with N_f samples.

Parallel imaging methods have dominated the MRI world since the introduction of SENSE[6] and SMASH[5]. The word “parallel imaging”, although can literally mean either receiving or transmitting, has almost exclusively been used for parallel receiving in reality. These parallel imaging methods use reduced phase encoding steps to achieve accelerations, usually by a factor of 2-4, and in some special cases, 6-8[4]. Part of the burden for phase encoding, which is used for spatial information localization, is shared using the sensitivity patterns of the receive array. R/O SEA reduces phase encoding step to perhaps the minimum number allowed, one. Phase encoding has thus completely removed. Spatial localization in the phase encoding direction is achieved exclusive through the coil pattern. The principle is shown in Figure 2.2 below.

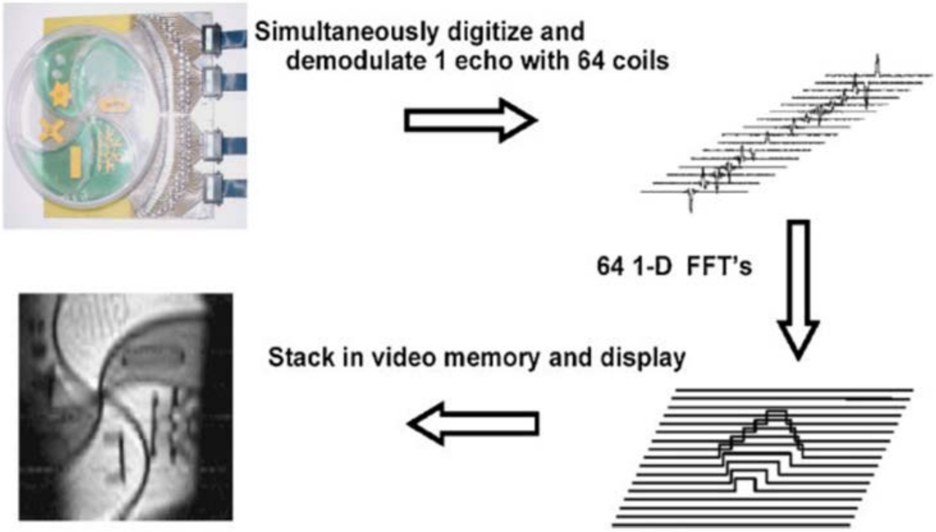

Figure 2.2 Illustrations of Principles of R/O SEA. This figure is reproduced from [11]. One image is formed from each echo by frequency encoding along the long axis of the elements of the array, and using the localization inherent in the RF sensitivity patterns of the elements to replace phase encoding. Slice selection is done as usual.

Gradient echo pulse sequence for R/O SEA is similar to that shown Figure 2.1, except that the phase encoding is fully eliminated. Instead, a fixed value is used which is called the phase compensation gradient [22, 23, 34]. In other words, the phase compensation gradient is a fixed phase encoding step. The necessity of phase compensation gradient is fundamentally caused by the fact that the voxel size is now on the same order as coil size in R/O SEA. The phase compensation gradient is closely related to coil design that is discussed in the next section, so it will be discussed later after that section.

II.2 Coil Design

R/O SEA uses long and narrow planar pair as the coil element [19, 20, 35], and placed evenly in the x direction. The direction in the narrow side is used for spatial localization of the original phase encoding direction. The long side is used for spatial localization of the frequency encoding direction. Both loop and planar pair designs were assessed in [31] for R/O SEA. Planar pair became the choice because of several advantages. First, it has less coupling, which was verified in method of moments simulations and bench measurements [19]. Also, it is less sensitive to loading, makes it easier to tune for 64 channels. The filed pattern is limited to the region above it, preventing signal from nearby areas to blur into the channel.

II.3 Phase Compensation Gradient in R/O SEA

With the coil designed, the transmit pattern and receive pattern of a single element is fully defined. Since it is more straightforward to think about it in the transmit domain, one often do the thinking and simulations in the transmit domain. The coil has a linear field. In MRI, circular polarization is desired. A linear field can be considered as two modes, one clockwise polarized (CP mode) and one counterclockwise polarized (CCP mode). The direction of the linear field becomes the phase of the circular polarization. For a planar array, this phase is dependent on the location. Figure 2.3 below shows the phase gradient along the phase encoding direction.

The phase gradient proposes a problem for receiving when the voxel size is on the same order as the coil size. Inside a voxel spins gives RF signals of different phases. The received RF signal becomes the vector sum of the sub regions. In order to get the maximum signal, an effort is necessary to bring all the spins into the same phase. Luckily, the phase gradient is quite linear in the region that gives the strongest signal. This means that a phase compensation gradient can be used. By applying this phase compensation gradient, the spins that are lagged in phase are given a pulse to advance, and the spins that lead are given a pulse to step back. RF signals from the sub regions are thus brought into roughly the same phase for a limited thickness above the array. Refocusing of the spins results in a much strongest RF signal which is received by the receiving RF coil.

Above is just a basic explanation of the phase compensation gradient. This subject has been fully examined in [22, 34] and should be referred to for additional details.

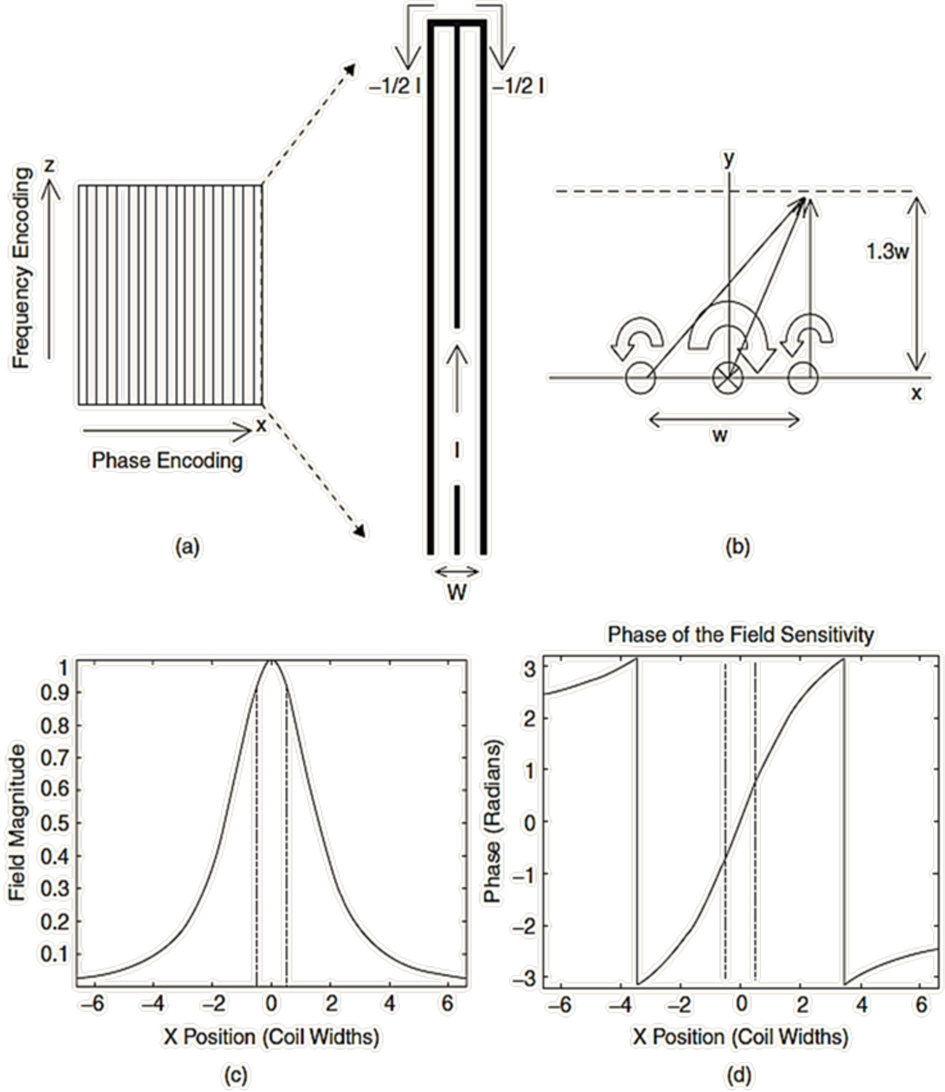

Figure 2.3 Phase Gradient in R/O SEA. Reproduced from [34]. (a) Diagram of planar pair element and enlarged in bold black in the upper middle, currents and width are labeled. b. cross section view of the coil, with an example calculation line marked. c. magnitude of magnetic field at a height 1.3 coil widths above the coil. d. the same plot as c, but showing phase instead of magnitude.

While the application of phase compensation gradient brings the signals in phase again, it has its limitations. First, phase compensation gradient is required to be a function of the distance from the coil for compensation in a volume. As discovered by Bosshard JC, it is mathematically forbidden to compensate for a whole volume with thick slice (unpublished). A variation of phase compensation gradient at different distance above the coil can be expressed as $\frac{\partial G_x}{\partial y}$, which is identical to $\frac{\partial G_y}{\partial x}$ because $G_x = \frac{\partial B_z}{\partial x}$ and $G_y = \frac{\partial B_z}{\partial y}$. In other words, it is theoretically impossible to create the desired y dependent x gradient without creating an x dependent y gradient which would bring additional phase effects. Second, phase compensation gradient for a SEA array is always in the narrow direction of the coil. This puts a stringent limit on the application of R/O SEA imaging, i.e., the array must be placed in a planar configuration. Otherwise it is impossible to do phase compensation for each coil. However, most living biological entities known to humans are not planar.

To lift these limitations, operating the SEA array in Transmit / Receive (T/R) mode is investigated as a solution to the problem. The phase imparted during the transmit window is expected to “refocus” during the receive window, thus eliminating the need for the required phase compensation gradient in R/O SEA. This will be further explained and verified using actual MR images, discussed in the next section of this dissertation.

II.4 Refocusing of Signal for a Single Channel Coil in T/R Mode - Theory

The theoretical background that when the received signal from all region is in phase when a single channel is used in TR mode has been well explained in [36]. Here, a brief explanation is provided in the text below.

When a single channel is operating in TR mode, the received signal can be expressed as:

$$\xi = 2\omega M_0 \sin(\gamma\tau|B_1^+|)\frac{-i\ B_1^+}{|B_1^+|}\widehat{B_1^-}$$

where

$$B_1{}^+ = \frac{B_x + jB_y}{\sqrt{2}}$$

and

$$B_1{}^- = \frac{B_x - jB_y}{\sqrt{2}}$$

note that the slight difference used for the definition of $B_1{}^-$ comparing to that shown in the Hoult's paper. His definition has an extra complex conjugate term, which is not used here. So the signal calculation done here removes the complex conjugate for the $B_1{}^-$ term which is shown in the original paper. The rest of the equation is the same as shown in that paper. Here, ω is Lamar frequency divided by 2π. M_0 is the equilibrium magnetization along the z direction. γ is the magnetogyric ratio and τ is the duration of transmit pulse. The circumflex accent above $B_1{}^-$ denotes fields due to unit current.

There is no circumflex accent above $B_1{}^+$ because it should be the actual excitation field, proportional to excitation current. The only terms that contain phases are B_1^+ and B_1^-. From the expressions of these two terms above, it is clear that they are complex conjugate when the frequency is not too high to bring full wave complications[37-43]. This results the received signal to be always in phase.

II.5 Refocusing of Signal for a Single Channel Coil in T/R Mode – MR Experiments

To verify the theory that the phase imparted from transmit is refocused during receiving, as stated in the previous section, MR images were taken. Fully encoded data sets of images were acquired. Instead of looking at the image space only, we would also look into the k-space raw data. A phase compensation gradient is required if the k-space data is off the center, i.e., if the DC component of the image has less energy than higher frequency part.

The most straightforward demonstration is a gradient echo image. A slightly modified Sgems sequence from Varian is used. Sgems is a slightly modified gradient echo sequence that works in the same principle as a normal gradient echo, but with reduced gradient requirement. The sequence is further modified to add blanking to the RF amplifiers, TR switches control and receiver gating to facilitate experiments later used for 64-channel TR SEA experiments. The results should remain identical to a straight gradient echo sequence. Two images were taken. The first image uses normal

R/O SEA setup. To remain a fair comparison with the next image, T/R switches are included in the setup, however, the transmitter is connected directly to the volume coil. The second image uses the same setup, but the T/R switches actually switch the transmitter and the receiver. Volume coil should be completely detuned for this image for SNR advantages and reduction of potential artifacts, but it was not done for the purpose of keeping the comparison with the first image fair. In one word, minimum differences in the setup were done for the two images for the fairest comparison. The parameters used are listed in Table 2.1 below followed by Figure 2.4 which shows the imaging results in both image space and k-space raw data.

While this is a relatively simple experiment using only commercially available parts from Varian Inova system, imaging results show several interesting points, revealing the basic underlying principle for this work and some cautions to be aware of that is important for the rest of the work.

First to notice from the above imaging results is difference in Signal to Noise Ratio (SNR). TR SEA give higher SNR, but the difference is related with imaging parameters. One can expect that the ratio to be higher when voxel size in x direction increase and vice versa. TR SEA gives higher SNR than R/O SEA because the imparted phase across the whole volume is fully recovered, which is not the case for R/O SEA. Even with phase compensation gradient, it is still expected to see higher SNR in TR

SEA because it is theoretically impossible to have the phase compensated at different height as analyzed in Section II.4.

Second to notice is that the TR image is sharper than the R/O image. The trace looks narrower. This is because that the TR image shows the transmit pattern multiplied with the receive pattern, while the R/O image shows the receive pattern. So the TR mode is roughly like square of the R/O image. A pulse when squared gets narrower.

Table 2.1 Pulse Sequence Parameters for Sgems Used for Verification of Elimination of Phase Compensation Gradient for TR SEA. These parameters were used for images shown in Figure 2.4.

Sequence	Sgems (modified)	Slice thickness / mm	0.5
TR /mS	100	Slice offset	1.5
TE / mS	8	Pulse duration / µS	4000
Average	1	90 deg pulse shape	Gauss
Readout	128	tpwr1 for TR SEA	20
Phase	128	tpwr1 for R/O SEA	20
FOV Readout / mm	90	Spectral width / kHz	100
FOV Phase / mm	90	Acquisition time / mS	1.28
Orientation	Coronal		

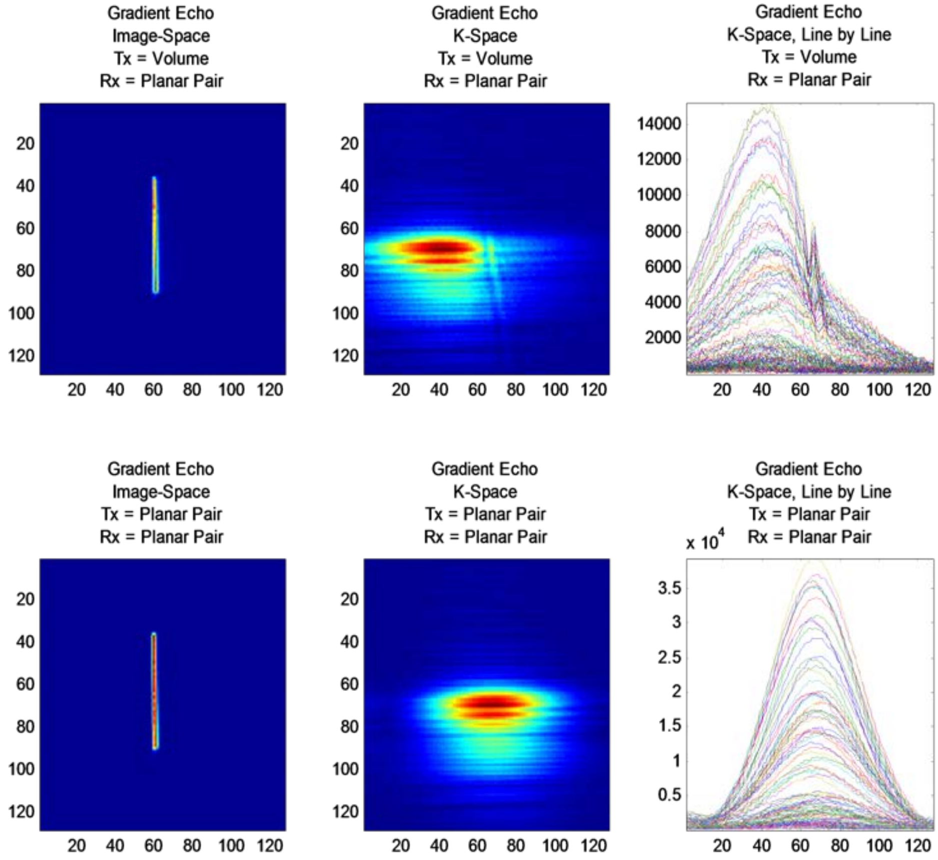

Figure 2.4 Results of Sgems Images Used for Verification of Elimination of Phase Compensation Gradient for TR SEA. The first row is for R/O SEA and the second row is for T/R SEA. The first column shows the results in image space. As expected, it is a long and narrow image. The second column shows the same results in k-space. The third column shows the same data as the second column, but plotting the data line by line in order to make the data more clearly visualized.

The third and the most important to note from the results above is that the k-space center shift disappears with TR mode, as expected, also because of the imparted phases get refocused later during receiving. This is exactly what we are looking for from the experiments. An off centered k-space picture indicates that the DC component has lower energy level and a gradient is necessary to move it to the center of k-space.

As a further investigation a sequence modified from Varian Ssems sequence is used. Ssems is a slightly modified spin echo sequence that works in the same principle as spin echo, but with reduced gradient requirement. We further modified it in a similar way we modified Sgems sequence. Two images were taken. The first image uses transmit with SEA array for “90°” pulse and receive with the same array, 180° pulses was through volume coil because it is impossible to achieve a uniform 180° flip using a planar pair coil. We refer to it as TR SEA here although it is not the normal TR SEA we do. The second image was a simple R/O SEA. Again, minimal changes were between the parameters for the two images for fairest possible comparisons. The parameters used for the two images are shown below in Table 2.2 and the results are shown in Figure 2.5.

The k-space center shift in the spin echo case actually doubled. This is because the 180° pulse flips the phases of all spins. To use a spin echo sequence for SEA imaging, one way is using double 180° pulses with a whole TE in between. This is, however, less practical. T/R SEA normally uses gradient echo for this reason.

Table 2.2 Pulse Sequence Parameters for Ssems Used for Verification of Theory of TR SEA.

Sequence	Ssems – modified	Slice offset / mm	1
TR / mS	300	90 deg pulse duration / µS	4000
TE / mS	30	90 deg pulse shape	Gauss
Average	1	tpwr1 for TR SEA	10
Readout	128	tpwr1 for traditional SEA	33
Phase	128	180° pulse duration / µS	4000
FOV Readout / mm	90	90° pulse shape	Gauss
FOV Phase / mm	90	tpwr2	39
Orientation	1.5	Spectral width / kHz	100
Slice thickness / mm	0.5	Acquisition time / mS	1.28

In order to use spin-echo, a double 180 pulse sequence is generated, called Ssems_dbl180. The center to center temporal interval between two 180 degree pulses should be TE/2, so that the spins get refocused. K-space data and images are shown in Figure 2.6.

With the basic concept for single channel TR SEA verified, a 64-channel TR SEA system is the next to investigate. But first, engineering work must be done to prepare the 64-channel transmitter.

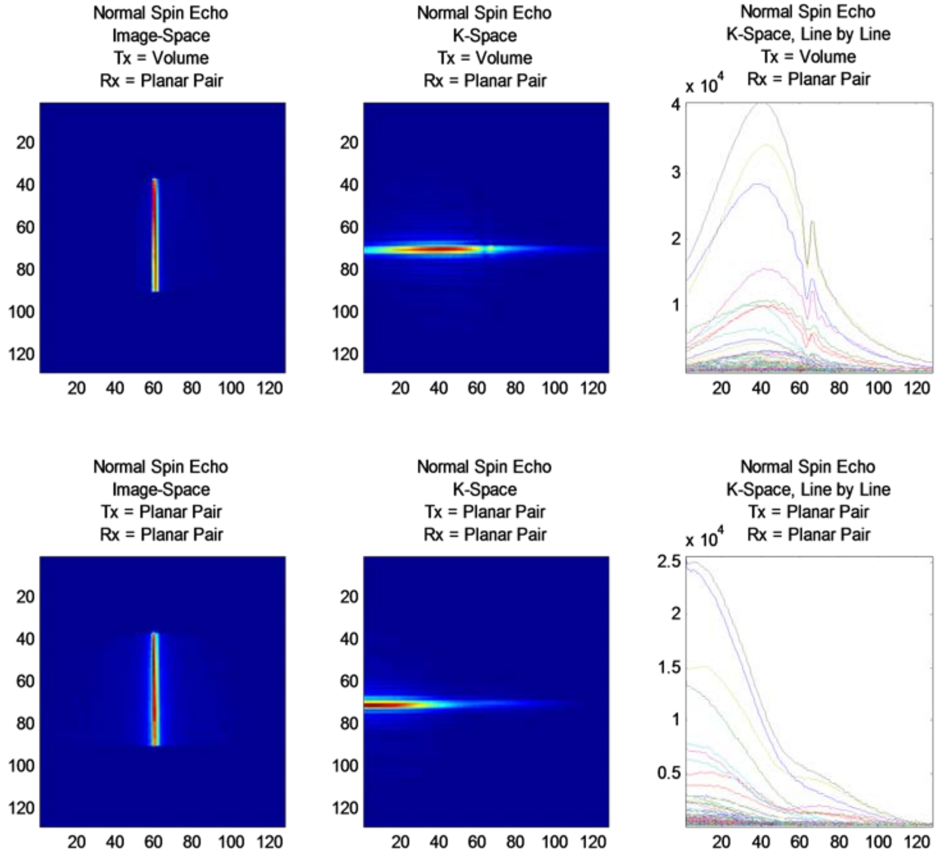

Figure 2.5 Results of Ssems Images Used for Testing of Elimination of Phase Compensation Gradient for TR SEA. The first row is for R/O SEA and the second row is for T/R SEA. The first column shows the results in image space. The second column shows the same results in k-space. The third column shows the same data as the second column, but plotting the data line by line in order to make the data more clearly visualized. Results show that TR SEA k-space off-center shifts even more with TR mode.

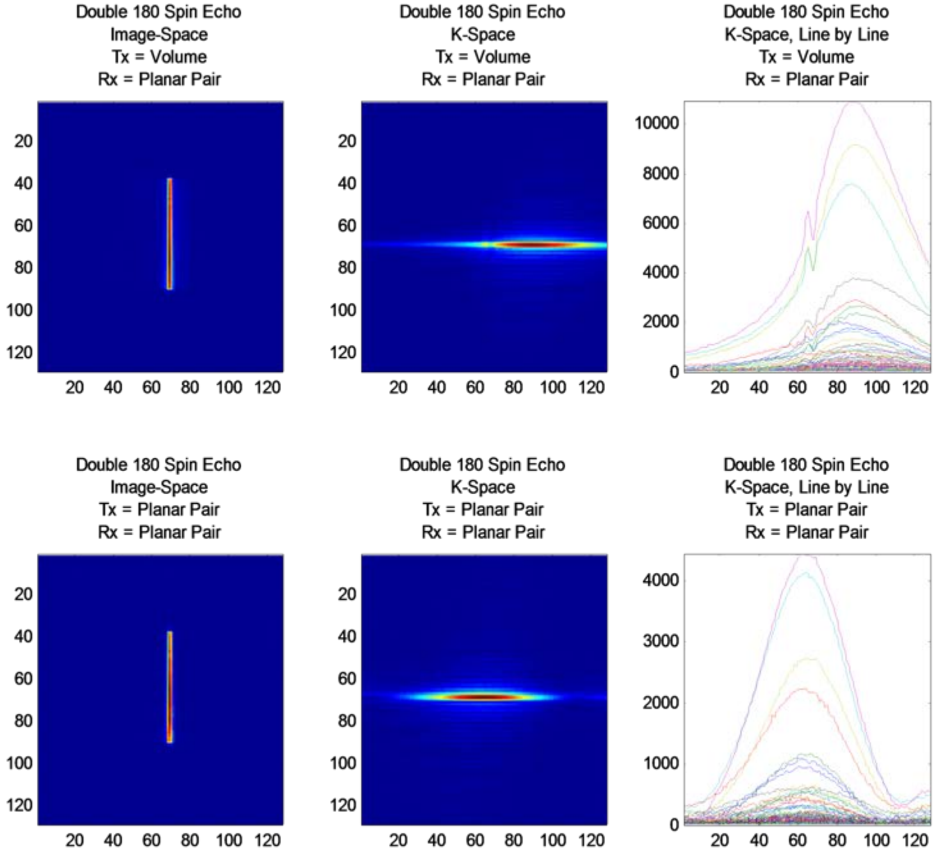

Figure 2.6 Results of Double 180 Spin-Echo Images Used for Testing of Elimination of Phase Compensation Gradient for TR SEA. The first row is for R/O SEA and the second row is for T/R SEA. The first column shows the results in image space. The second column shows the same results in k-space. The third column shows the same data as the second column, but plotting the data line by line in order to make the data more clearly visualized. Results show that TR SEA k-space off-center shifts even more with TR mode.

CHAPTER III

TRANSMITTER HARDWARE SYSTEM DESIGN

The receiver system has already been previously designed, constructed and used in the lab. This section will focus on the transmitter hardware, although the receiver is briefly introduced at the end of the section. The design considerations followed by each part of the transmitter will be introduced.

III.1 Considerations for Design

An important consideration for building a parallel transmitter is the associated cost. The total cost of a parallel transmitter array goes almost linearly with the number of channels. For this reason, even though simply purchasing 64 commercially available transmitters to form a 64-channel parallel transmitter is theoretically possible, cost issues make this solution impractical in reality for most researchers.

Maintenance should also be kept in mind in the designing stage. Failure rates are expected to increase more than linearly as the channel count is increased. Serviceability and debugging must be considered during the design phase. A modular design is a must to address these potential issues.

Calibration is another major consideration. When only a single channel transmitter is used, it is often unnecessary to know the exact phase or amplitude transmitted to the coil that is connected to it. In contrast, different channels of the parallel system will often need to have uniform gain and phase shifts.

Other practical factors, like heat, power and total size are all needed for consideration too. Commercial single channel transmit chains often require a full rack of equipment. This size of system would require unacceptable amounts of floor space for large array systems. Total power dissipated as heat also poses a significant problem. Passive, forced air or liquid cooling may be necessary if other thermal control methods are needed. Electrical supply requirements can also be quite large, but the infrastructure.

III.2 System Overall Design

The parallel transmit system uses the Varian Inova MR system's RF output before it is sent to the power amplifier. The RF is split between all 64 channels, modulated, and then amplified. Most current available systems use individual components to control the amplitude and phase. A vector modulator, which will be discussed in more details later, is used for each channel in this system because of reduced cost and simplicity in designing and construction. Two stages of amplification are used to boost the power to a maximum of 100W per channel. A very basic block diagram is shown in Figure 3.1.

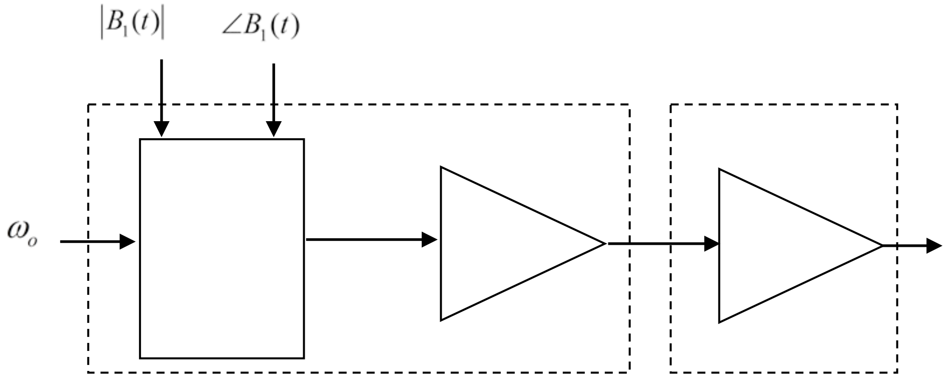

Figure 3.1 Big Picture of Transmitter System. RF input, which is labeled as $\omega_{0,}$ is effectively modulated by both amplitude, which is labeled as $|B_1(t)|$, and phase, which is labeled as ∠B1(t). After the modulation, two stages of RF power amplification are used to boost the power to the desired level of at least 40W per channel.

With the big picture in mind, the system is designed as a modular system. This part took the bulk of the project, predominantly because of the complexity of the system together with lack of human resources and problems of manufacturing and debugging. The system was designed to be highly modular, both to enable components to be changed out in the event of redesign or in the event of failure. More details of the design, with rough power level at each point through the RF signal chain, are shown in Figure 3.2. Information for each part of the system will be covered with more details through the rest of this chapter.

Figure 3.2 Transmitter System Block Diagram for a Single Channel with Rough Power Levels Labeled. The figure is shown in the next page. A system level block diagram is shown, together with rough power levels. The parallel transmit system can operate in either “static modulation” mode using a simple potentiometer based control solution as shown above, or in “dynamic modulation” mode with a DAC based control system. In either mode each channel is capable of producing 100W output, and the T/R switches make a full 64 channel transmit/receive system possible.

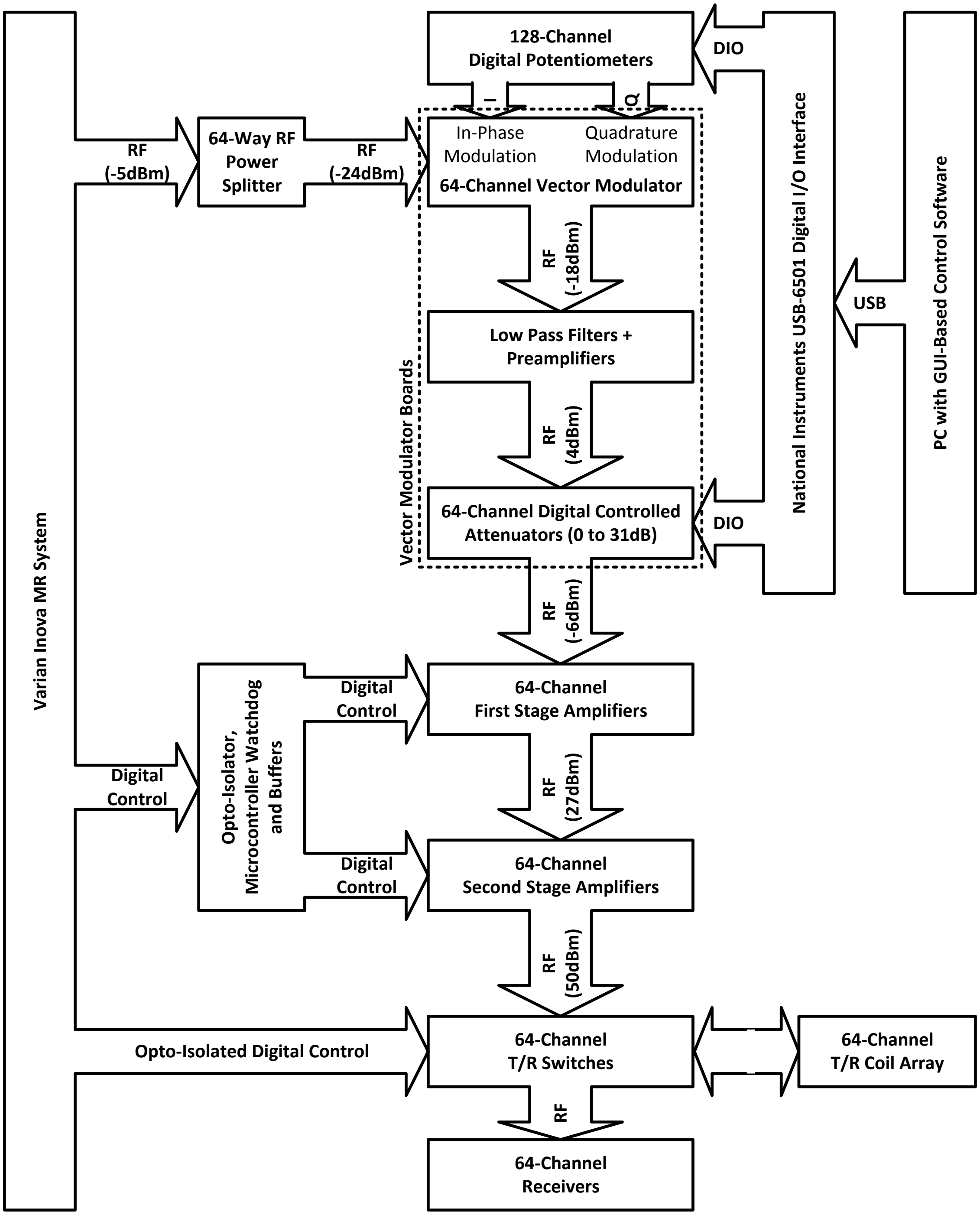
128-Channel
Digital Potentiometers
DIO
I
Q
RF
(-5dBm)
64-Way RF
Power
Splitter
RF
(-24dBm)
In-Phase
Modulation
Quadrature
Modulation
64-Channel Vector Modulator
RF
(-18dBm)
Low Pass Filters +
Preamplifiers
RF
(4dBm)
64-Channel Digital Controlled
Attenuators (0 to 31dB)
DIO
Vector Modulator Boards
National Instruments USB-6501 Digital I/O Interface
USB
PC with GUI-Based Control Software
Varian Inova MR System
RF
(-6dBm)
Digital
Control
64-Channel
First Stage Amplifiers
Digital
Control
Opto-Isolator,
Microcontroller Watchdog
and Buffers
RF
(27dBm)
Digital
Control
64-Channel
Second Stage Amplifiers
RF
(50dBm)
Opto-Isolated Digital Control
64-Channel
T/R Switches
64-Channel
T/R Coil Array
RF
64-Channel
Receivers

III.3 Vector Modulator at Component Level

A vector modulator is used as the core component for the modulation system. It can be made by a quadrature hybrid combiner, two amplitude modulators and an RF power combiner, as shown in Figure 3.3. The RF power is split evenly with a 90 degrees phase shift by the quadrature hybrid combiner. One of the outputs of the quad-hybrid is then mixed with the I input, and the other with the Q input. The mixing products are then combined to produce the output of the modulator. In this way both amplitude and phase control can be achieved simultaneously.

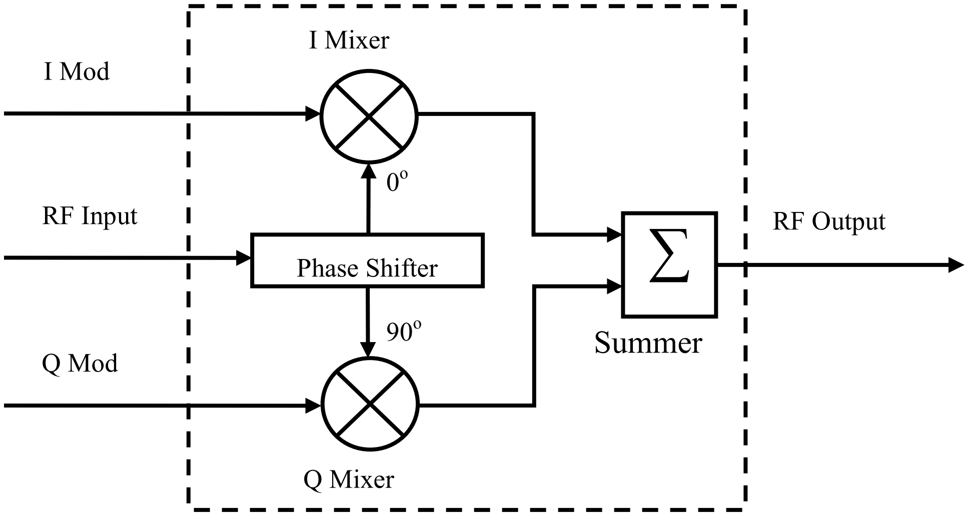

Figure 3.3 Basic Block Diagram of a Vector Modulator. The signal path has three inputs, which are RF input (LO), baseband in phase modulation (I Mod) and baseband quadrature modulation (Q Mod). One output for the signal path, which is RF output.

Although building such individual vector modulators is possible, such as successfully accomplished by Stang et al, single chip vector modulator solutions are available that reduce size and complexity of the circuit. RF components also tend to be more expensive, which is another advantage for ICs. Agilent HPMX-2005 is chosen in this research because it is low cost (less than $4 each), covers the frequency range we are considering using it for (64MHz, 128MHz and 200MHz) and is easy to use with the help of reference design circuit provided by Agilent in its data sheet.

The I and Q inputs are derived from two 128-position digital controlled potentiometers configured as simple voltage dividers. This configuration provides a linear phase and power level control. The usable dynamic range of is only 20dB otherwise the steps become too “coarse”. The addition of a 0 to 31dB digitally controlled attenuator with 1dB resolution increases the dynamic range of each channel to approximately 50dB for a given RF input level. The 64 channel transmit system has 16 vector modulator boards, where each board has four independent channels. Each of the board has one RF input that is split into four to supply the separate channels.

III.4 Four-Channel Vector Modulator Board

Despite the name of “vector modulator board”, it is actually much more than four vector modulators. The board is used to for several functions at low power level, including baseband signal conditioning, vector modulation, low pass filter, preamplifier and digital controlled attenuation.

Typical MR transmit systems use an architecture that requires one or more Intermediate Frequency (IF) stages prior to mixing to the final frequency. This makes it both expensive and complex to purchase additional modulation systems to increase the transmitter channel count, limiting the practicality of constructing high channel count systems. Only some of the newer MRI systems use a direct digital synthesizer to eliminate the hardware IF mixers before digital to analog conversion (DAC), this can avoid many of the imperfections in the analog mixer circuits and thus provide higher waveform fidelity[44].

Vector modulation based architecture is an attractive alternative that also provides simultaneous amplitude and phase modulation while avoiding much of the cost and complexity of typical systems. This scheme has been employed for MRI utilizing discrete components[45], however single chip Integrated Circuit (IC) vector modulators are becoming readily available due to extensive use in the telecommunications industry, allowing for faster, easier development of this type of modulator. These integrated solutions greatly reduce size, complexity, and cost of the system which are critical factors for large arrays. The Agilent HPMX-2005 was chosen in this research because it covers 1.5T (64MHz), 3T (128MHz) and 4.7T (200MHz) frequency that the system might be used for, and it requires few peripheral components. Additionally, it requires only three inputs: RF at the desired frequency as well as the In-phase (I) and Quadrature (Q) base band signals. It is possible to control the common phase of all channels for slice offset and phase cycling with the existing MR system because each modulator receives the same RF input signal. This eliminates the need for separate phase locked IF signals, reducing the complexity of the system.

Some care must still be taken in conditioning the input and output signals for the HPMX-2005 chip. The I and Q inputs for the modulator chip need to be 2.5V±0.75V. Theoretically I=2.5V and Q=2.5V gives zero amplitude output, I=3.25V and Q=2.5V gives maximum amplitude output, with the same phase as the RF input, I=2.5V and Q=3.25V gives the maximum amplitude output, with a 90-degree phase shift from the RF input. Most computer controlled DAC cards do not directly provide output in this range. An analog signal conditioning circuit was implemented on the modulator boards in order to best utilize the dynamic range of DAC cards. The op-amp based circuit was designed that takes the ±10V range signal generated by the NI-6713 and linearly converts it to the desired range using the circuit shown in Figure 3.4.

The condition circuit also provides for the minimization of the vector modulators' Local Oscillator (LO) leakage. Two fine adjustment (20 turn) mechanical trimmer potentiometers are used to control the offset voltage. The offset voltage is adjusted so that a zero value point in the waveform results in the minimum output signal from vector modulator. Error in the offset results in RF at the center frequency being transmitted, which will cause a zipper artifact in the image. Stang et al present an alternative approach to this calibration by providing the offset in software[46], a potentially more robust approach in terms of calibration as the analog offsets have been found to drift over time. We combine the techniques, using hardware for rough calibration and software for additional fine calibration when needed.

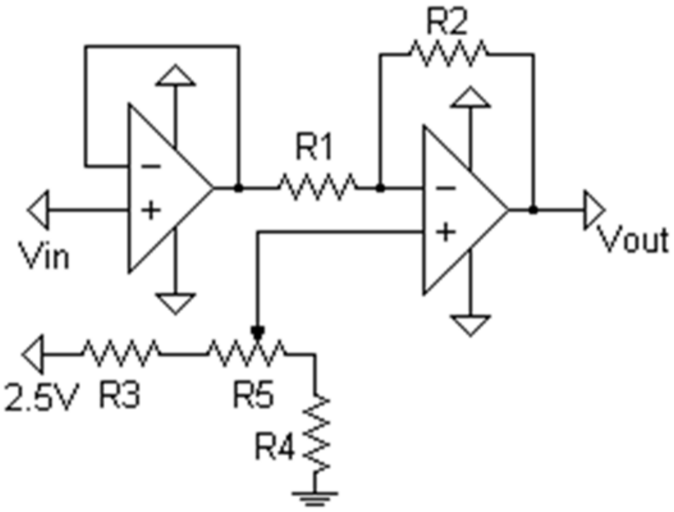

Figure 3.4 Baseband Signal Conditioning Circuit, i.e. DC Voltage Linear Transformer. This signal conditioning circuit is used to convert -10V to +10V input signal into 2.5-0.75V+ΔV to 2.5+0.75V+ΔV signal required by the vector modulator. By adjusting the position of R5, the offset, ΔV, can be controlled. This can be used to remove LO leakage caused by vector modulators.

Each channel includes a low pass filter at the output of the vector modulator chip in order to reduce higher order mixing products which could bring noises. Following this a low power gain stage is included to achieve the desired drive level for the power amplifier stages. The HPMX-2005 is only linear in power up to -15dBm output necessitating at least 10dB of gain to achieve the -5dBm output level that we desired. A Mini-circuit gali-74 monolithic gain stage followed by a digital step attenuator is used to meet the power requirements.

The inclusion of a 0 to 31dB digital step attenuator (Mini-Circuits, part number DAT-31R5-PP+) with 1dB resolution (the device allows 0.5dB step, but in this design, 1dB is used for simplicity in design) allows us to compensate for gain variation between channels and utilizes the full dynamic range of the digital controlled potentiometers or computer controlled DAC cards. Alternatively gain corrections could be made by adjusting the I and Q signal levels in software. The problem with this approach is that it reduces the utilized dynamic range of the vector modulator chips in effect reducing the resolution of the system.

A block diagram of one channel of a vector modulator board is shown in Figure 3.5, and a photo of the 4-channel vector modulator board using this design is shown in Figure 3.6.

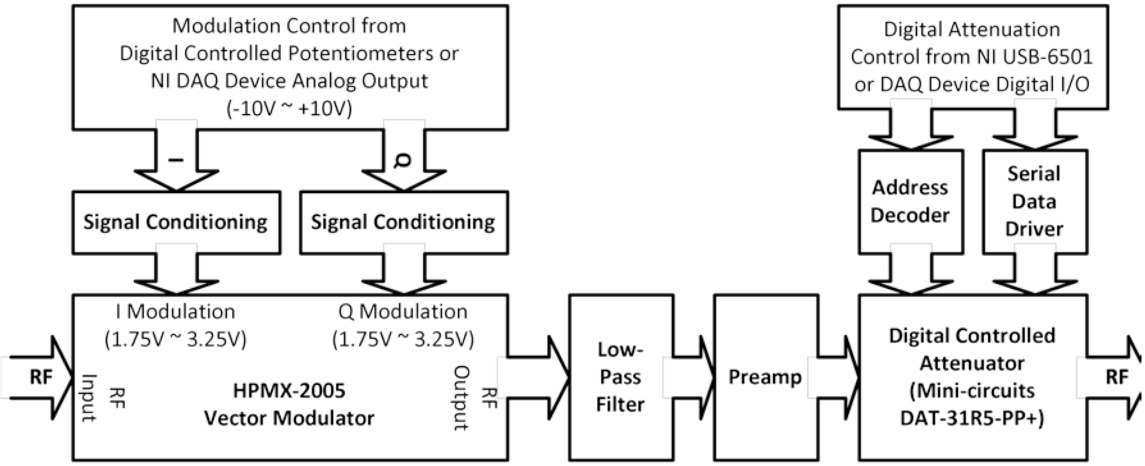

Figure 3.5 Vector Modulator Board Block Diagram for One Channel. The modulator is capable of both static and full modulation by simply providing the appropriate control on the baseband I and Q inputs. The output of the vector modulator is filtered to remove unwanted mixing products, followed by a digitally controlled attenuator that allow the dynamic range of the system to be best utilized. The system is reconfigurable. When static modulation is used, an NI USB-6501 is used to control both the digital controlled potentiometer boards and the on board attenuators. When full modulation is used, a high speed DAQ device with both analog and digital output is used to control both the modulation signals and attenuation controls.

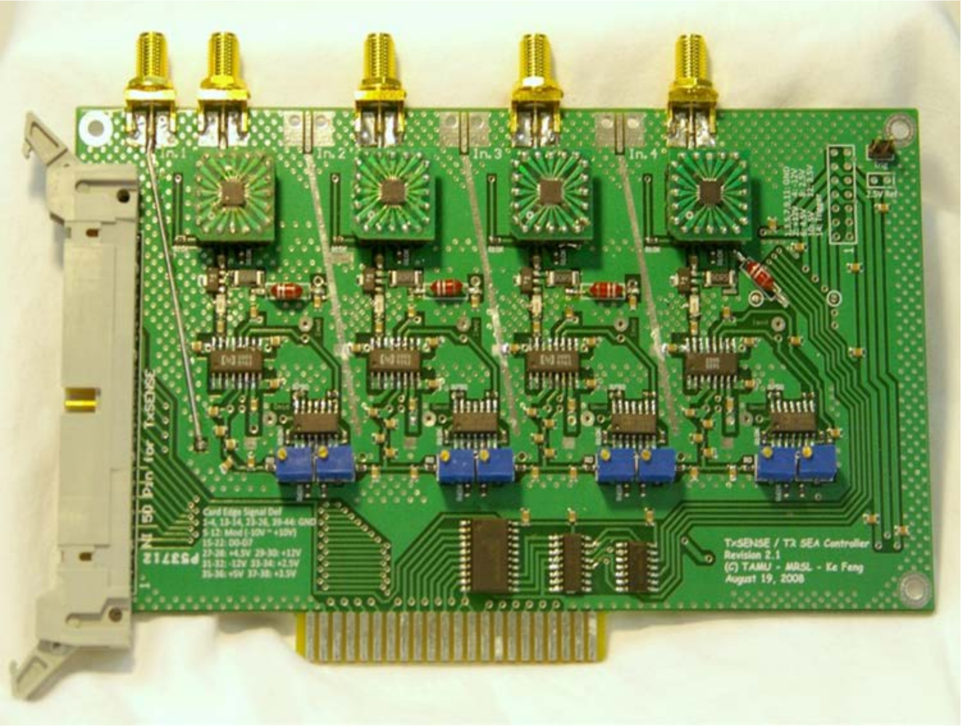

Figure 3.6 Photo of a Four-Channel Vector Modulator Board. Control and base-band modulation lines are available on both the left side connector for NI DAQ cards and the bottom side card edge connector use with the digital controlled potentiometer boards. Input RF signal enters on the top left SMA and is split four ways to feed each channel on the board. The modulated RF outputs are the remaining four SMA connectors. For convenience, the pin definitions for the card edge are printed on the bottom left corner of the board. For TR SEA or B1 shimming applications, the board sits on the motherboards of the 64-channel system. For Transmit SENSE, the board can be stand alone.

III.5 Digital Controlled Potentiometer Board

The digital controlled potentiometer board was originally designed for providing bias to varactors for the purpose of tuning large arrays, in particular, varactor tuned SEA receive arrays. For this reason, it was original named “digital tuning board”. Figure 3.7 shows a block diagram of the digital tuning system. Figure 3.8 shows the actual PCB board, together with a National Instruments (NI) Data Acquisition (DAQ) USB Input / Output (IO) device. Each board has 32 analog voltage outputs. They are based around a bank of Analog Devices AD7376 digital controlled potentiometers, providing 7-bits of resolution on each channel. Digital controlled potentiometers, which are often called digital rheostats in literatures too, were chosen for static modulation because they are low cost alternative for DACs. A digital controlled potentiometer works similarly to a mechanically adjustable one. It has two voltage terminals and a “wiper”. The wiper resistance of the AD7376 is set through a three wire Serial Peripheral Interface (SPI) as opposed to with a knob or slider that mechanical potentiometers use. It is possible to change the wiper resistance in 14 digital bits by setting it directly, as opposed to up to 128 digital “clicks” you might see when using the step control common in other digital controlled potentiometers, making it an order of magnitude faster in some cases. The AD7376 is also able to handle voltages beyond the ±10V range needed for this application, and had previously been used to provide DC control voltages to varactor diodes for tuning large RF coil arrays [15].

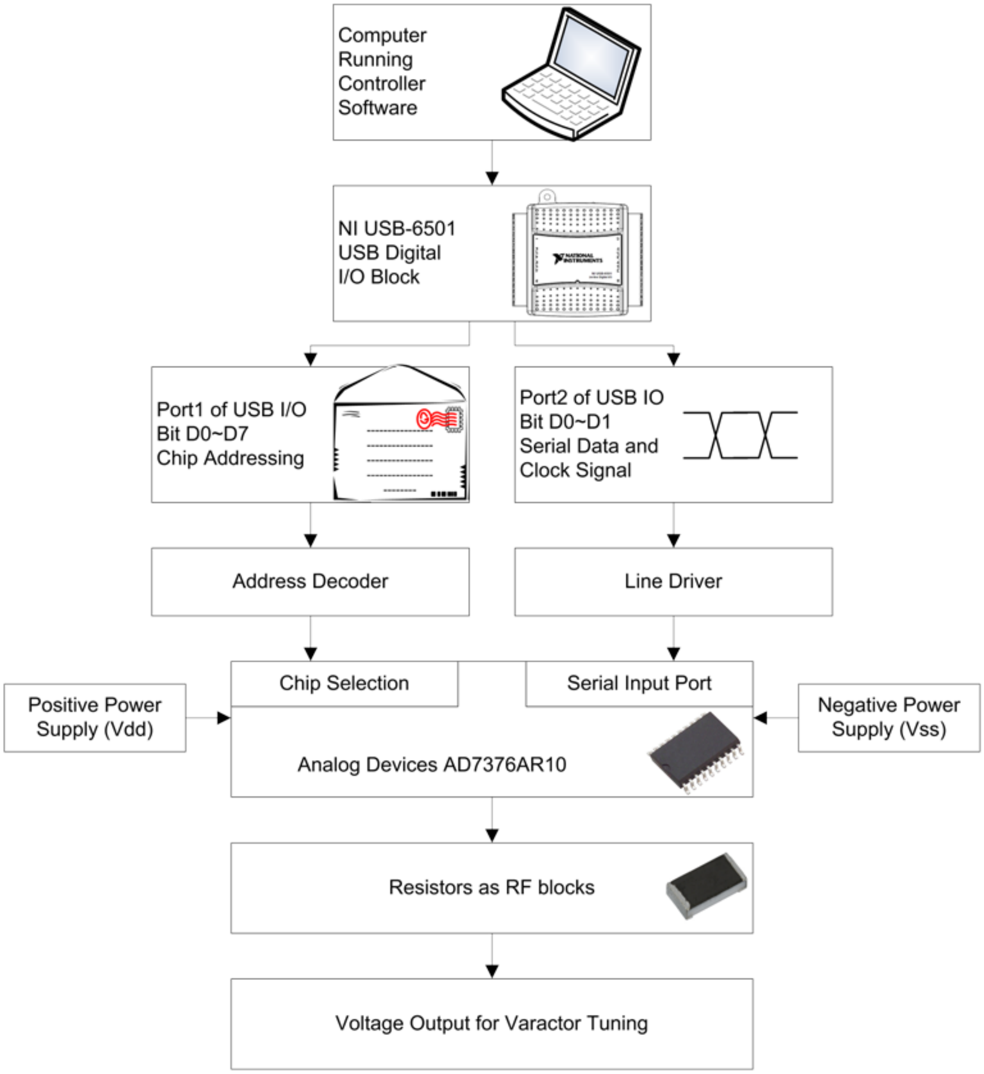

Figure 3.7 Block Diagram of a 32-Channel Digital Controlled Potentiometer Board. A computer communicates with the digital controlled potentiometers through a USB DAQ device. The digital controlled potentiometers are configured as voltage dividers. The wiper position is controlled by the computer. Voltage output can be set as one of the 128 positions evenly distributed between the two terminal voltages.

Figure 3.8 Photo of a 64-Channel Digital Controlled Potentiometer Board. Each digital controlled potentiometer board has 32 channels. They can be daisy-chained together for more channels. Each board needs a different jumper position though. The jumper is located on the bottom right side of the photo above. This 64-channel transmitter uses four such boards for 128 digital controlled potentiometers because each channel requires two modulation input, I and Q.

Control of the board requires ten digital lines which are provided by a National Instruments USB-6501 card. Eight of the lines are used to addresses the individual potentiometers through address decoders. Two lines provide a simulated SPI interface, i.e., clock signal (CLK) and serial data (SDI), needed to control the potentiometers. A detailed timing diagram is shown in Figure 3.9.

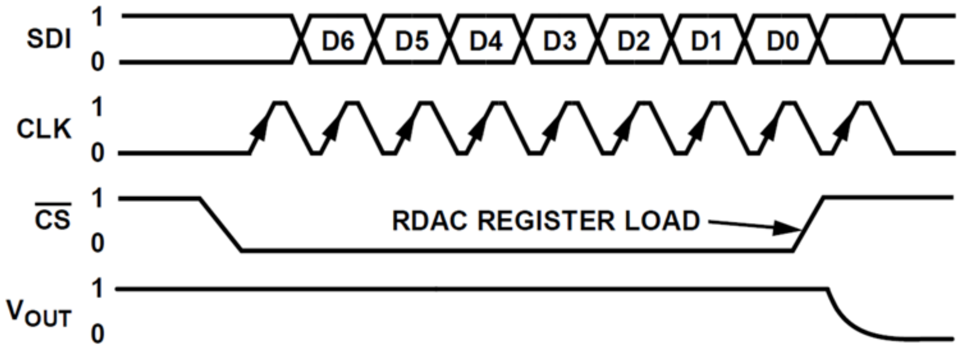

Figure 3.9 Analog Devices AD7376 Digital Interface Timing Diagram. Figure is reproduced from the data sheet of Analog Devices, AD7376. A clock signal (CLK) is used to synchronize the data receiving of the serial data. A chip select negative logic ($\overline{CS}$) is used to set the chip into receiving mode.

III.6 First Stage Amplifier

The first stage amplifier, shown in Figure 3.10 for schematic and Figure 3.11 for actual photo, is built around a commercial class A commercial amplifier module (Freescale MHW-1345N) with a peak output of up to 800mW output at 34dB of gain. The module is internally 50Ω matched for both input and output. By using the commercially available module, the design becomes relatively easy to implement. This module can be used directly but a few components are added here.

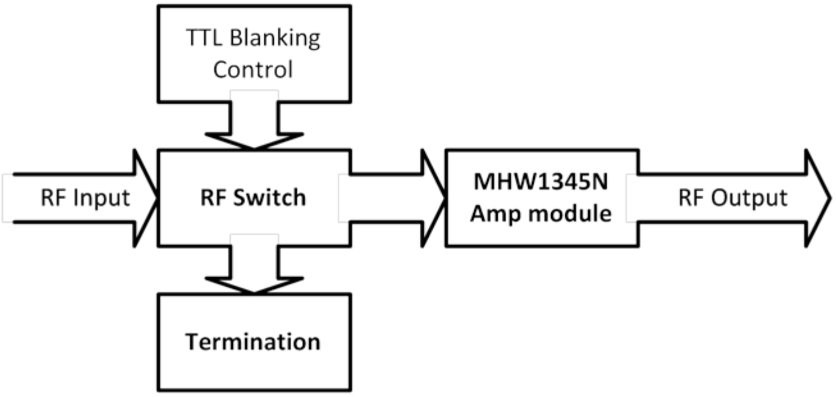

Figure 3.10 Block Diagram of First Stage Amplifier. The first stage amplifier uses a MHW1345N module to form a compact, low complexity module. A RF switch terminates the amplifier input in a 50Ω load except during the transmit window. This reduces the noise outside of the transmit window, most importantly during the receive window. 30dB reduction in out noise level is observed with this addition.

An important factor to consider for any amplifier design for MRI applications is noise blanking. An inexperienced designer might be able to make an amplifier, seeing everything performing perfectly on network analyzer or oscilloscope, but the system simply will not work for MRI imaging. This is because of huge dynamic range in power level in MR system. The transmit power is easily on the order of kilowatts. The received power, however, is constantly very low, easily 100dB lower than the transmitted power. If noise is not taken care of, a very small noise at the input of the amplifiers, often unavoidable such as thermal noise, will get amplified to a power level that is high enough to cover up all the received signals.

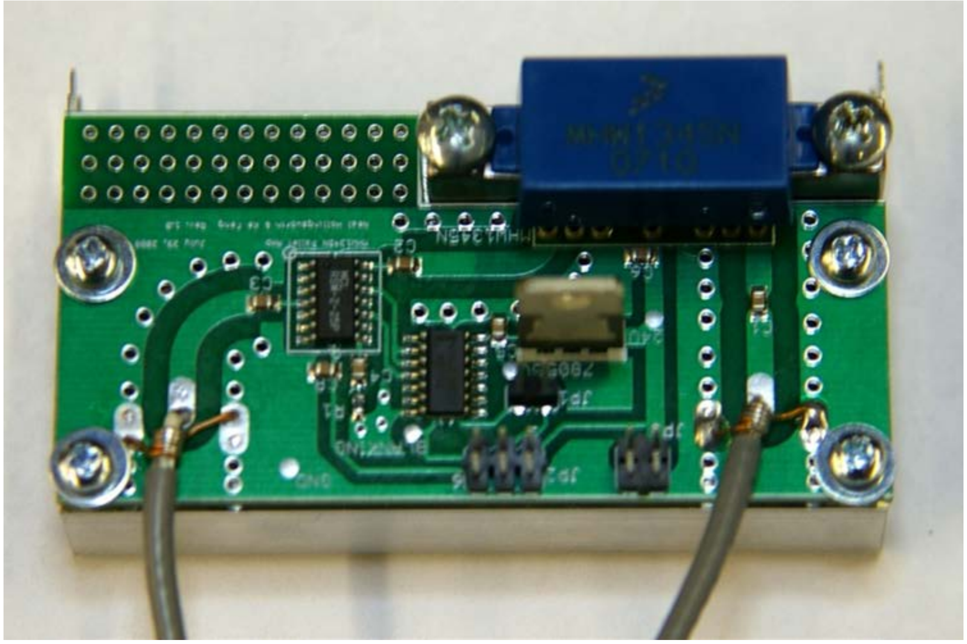

Figure 3.11 Photo of a First Stage Amplifier. FreeScale MHW1345N based first stage amplifier is a compact, 800mW output gain stage. Power and control lines are on the header pins shown at the bottom, with RF input (left) and output (right) on pigtailed coax. Connections of this type help to reduce the total cost of the system.

To address the noise issues, it is very important to have noise blanking considered at every amplifier stages. An RF switch (Mini-Circuits RSW-2-25P+) is used in the first stage amplifier at the input to provide noise blanking. During the transmit window, the RF is routed to the input of the module, at all other times it is shunted to a 50Ω load. Not as ideal as directing the output, it is much cheaper and easier. RF components are normally much cheaper and more widely available at lower power stages. The blanking provides about 40dB blanking. Making it negative gain for the first stage when blanked.

III.7 Second Stage Amplifier

The second stage amplifier uses a Laterally Diffused MOSFET (LDMOS) device (FreeScale MRF6V2150N), as shown in Figure 3.12. The amplifier is designed to work in class AB mode, with a maximum linear output of 100W and 24dB of gain.

Realizing input and output matching network using microstrip transmission lines and capacitors is unique for amplifier used for MRI. This design, shown in Figure 3.13, has several advantages. This topology eliminates the need for inductors in the matching networks and reduces variability between amplifier boards making it possible to achieve acceptable performance without hand-tuning each amplifier. The elimination of inductors from the matching networks also helps mitigate coupling between channels. The worst case isolation between neighboring channels of the whole transmitter chain was measured to be -31dB without the use of individual shielded enclosures for each amplifier, as compared to a previous design [26] which had -20dB isolation when the amplifiers were individually shielded and placed 2 inches apart. This made it possible to avoid individually shielding every amplifier, which helped with both serviceability of the system and with reducing complexity of construction.

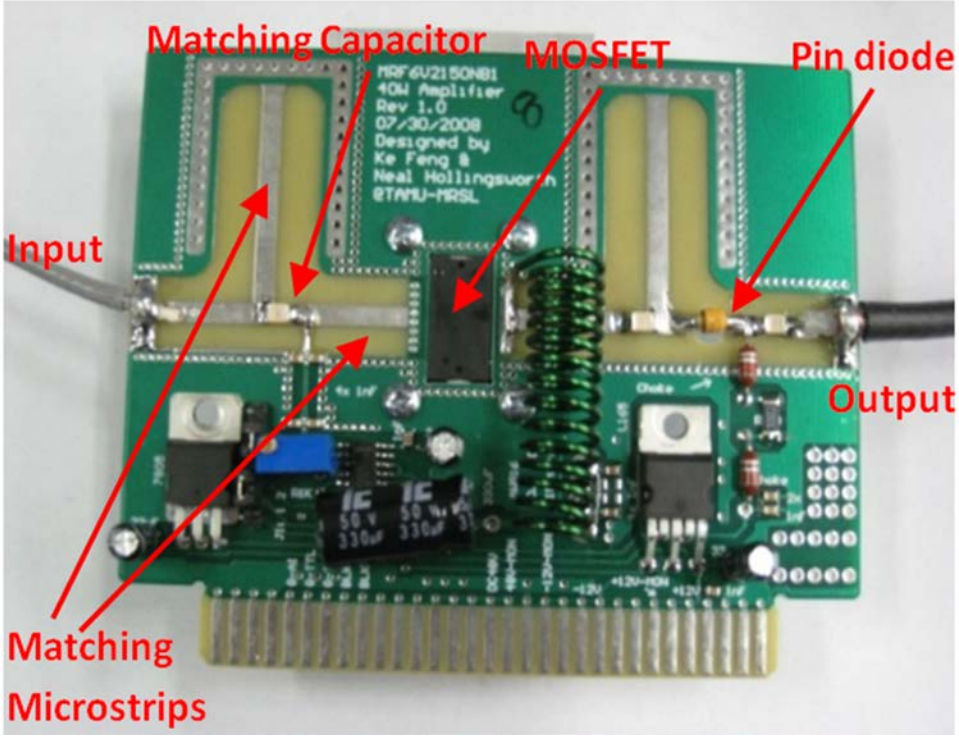

Figure 3.12 Photo of a Second Stage Amplifier. The LDMOS transistor based power amplifiers use a capacitor and microstrip for input and output matching networks. This avoids the need to precisely valued inductors that could couple to each other, removing the need to individually tune each amplifier in order to obtain an output level of 100W. The low power RF enters the board on the left and high power output is on the right, separating the RF signals on the board to avoid feedback. The card edge connections give DC, gate bias control, and blanking control. The PIN diode (seen on right) is used to minimize the noise during the receive window.

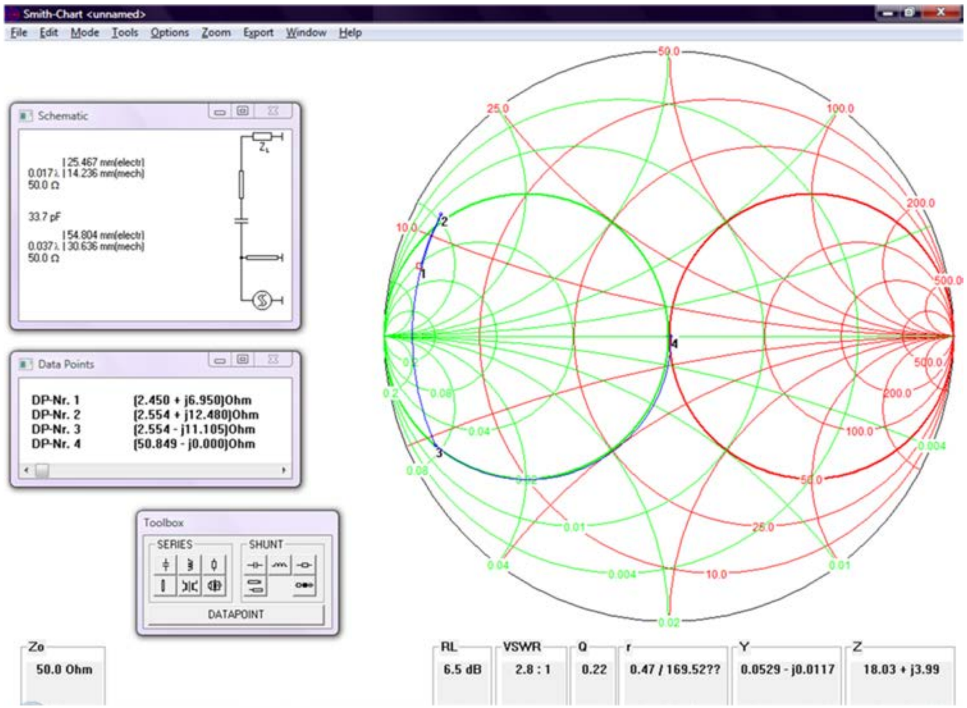

```
            |25.467 mm(electr)
0.017λ |14.236 mm(mech)
50.0 Ω

33.7 pF

            |54.804 mm(electr)
0.037λ |30.636 mm(mech)
50.0 Ω
```

```
DP-Nr. 1        (2.450 + j6.950)Ohm
DP-Nr. 2        (2.554 + j12.480)Ohm
DP-Nr. 3        (2.554 - j11.105)Ohm
DP-Nr. 4        (50.849 - j0.000)Ohm
```

Zo 50.0 Ohm

RL 6.5 dB

VSWR 2.8 : 1

Q 0.22

r 0.47 / 169.52??

Y 0.0529 - j0.0117

Z 18.03 + j3.99

Figure 3.13 A Smith Chart Software Used for Assisting with the Matching Network Design. The optimal load impedance, as given by the manufacturer is 2.45+j6.95Ω (Point 1). A 14.24mm section of 50Ω transmission line followed by a 33.7pF capacitor brings the impedance to 2.554-j11.1Ω (point 3). Finally, a 30.6mm shorted stub of 50Ω transmission line matches the input to 50Ω (point 4).

Again, noise blanking is very important in the amplifier. Here, two blanking schemes are used simultaneously in this amplifier.

A series PIN diode (MicroSemi UM9405) is used to reduce noise outside of the transmit window by forward biasing it during transmitting and reverse biasing it at all other times. This is less ideal than a tank circuit, but it does not require individual tuning for each amplifier boards and so that make it much easier for large arrays. One concern of the tank circuit is that it might shift over the time. The simple in series PIN diode eliminates this viability.

Further noise reduction is achieved by controlling the gate bias for the MOSFET with the blanking signal so that the device is turned on only when transmitting. The time it takes to stabilize is only about 2 to 3 RF cycles at 200MHz. This also reduces the total power consumption and heat dissipation of the MOSFET.

Each of the two methods discussed in the above text provides at least 20dB of blanking. When both of them are used, a gain of at most -16dB will be seen, considering the normal gain of 24dB. A negative gain has been an efficient measure for noise blanking.

III.8 System Interlocks and Second Stage Amplifier Gate Watchdog

The output stage of the RF amplifiers is designed to work in pulse mode only. If they are fully biased for an extended duration of time they will suffer from thermal overload and fail. Following the first such catastrophic failure of amplifiers a “watchdog” circuit was implemented, which uses a standard 8051 microcontroller that monitors the gating signal for the amplifiers. The maximum duty cycle and continuous on-time can be set using two DIP switches. Absolute maximums are set at 2 seconds of continuous on-time, and 30% duty cycle for a period of 5 seconds. Stricter limits can be set, which is desirable in cases such as hardware testing where the output might become disconnected resulting in more reflected power, or other problems may be encountered. The duty cycle is constantly calculated and displayed on two digits of seven-segment LED displays. If either of these two limits is exceeded, it will immediately disable the amplifiers by holding the blanking line low, and the LED would display the error code until the reset button is pressed.

The watchdog circuit is based on an Atmel AT89S52 microcontroller. The choice of the 8-bit microcontroller was mainly because of my personal familiarity with the Intel 8051 microcontroller architecture. However, the program was written in C. It should be easy to migrate to a faster microcontroller with more memory. New designs, if necessary, should be advised with newer microcontroller. A system schematic is shown in Figure 3.14. Because of the simplicity of the circuit, it was actually built on a breadboard. The watchdog circuit inserts only a single logical AND gate in the blanking signal path, which is shown in the middle right part of the circuit schematic. This ensures that there is a fixed, low propagation delay (about 20 nanoseconds) in the blanking signal so that there is no timing error between the transmitter and the rest of the MR system. Another advantage of this design is that the complicated phase lock between the watchdog circuit and MR system becomes unnecessary, which can greatly reduce the system complexity and increase the system stability.

Software was developed in traditional ANSI C to ensure possible migrations to other microcontrollers if needed in the future. The C source code was was compiled using Keil C for 8051. The input gate control is monitored at fixed time intervals, which is 1mS. This interval can be much shorter if a different microcontroller chip is used. The current value is then pushed into a memory buffer in a compressed way to save the memory requirement. The last stored value is pushed out at the same time. The compression was achieved by combining the same values into groups. The maximum buffer size is defined to be 5000 so it stores the input waveform of 5 seconds. This is because previous experiences indicate that thermal overloading failures happen in roughly such a time frame. Duty cycle is calculated for the 5 seconds interval, and constantly compared to the maximum value the user sets through the DIP switch. Definitions of each bit are shown in Table 3.1. Details of the settings are shown in Table 3.2 and 3.3. The maximum continuous on time is also measured in the same way. If any of the limits is exceeded, the output is immediately disabled. The error code is also displayed on the 7 segment display. The program gets into an endless loop, and the only way to get out would be pressing the reset button.

When initially powered up or immediately after the reset button is pressed, the 2-digit 7-segment display will show “c1”, followed by maximum allowed on time setting. Then “c2” and maximum allowed duty cycle settings. Afterward, the duty cycle is displayed in real time, in the unit of percentile, unless one of the user set limit is exceeded.

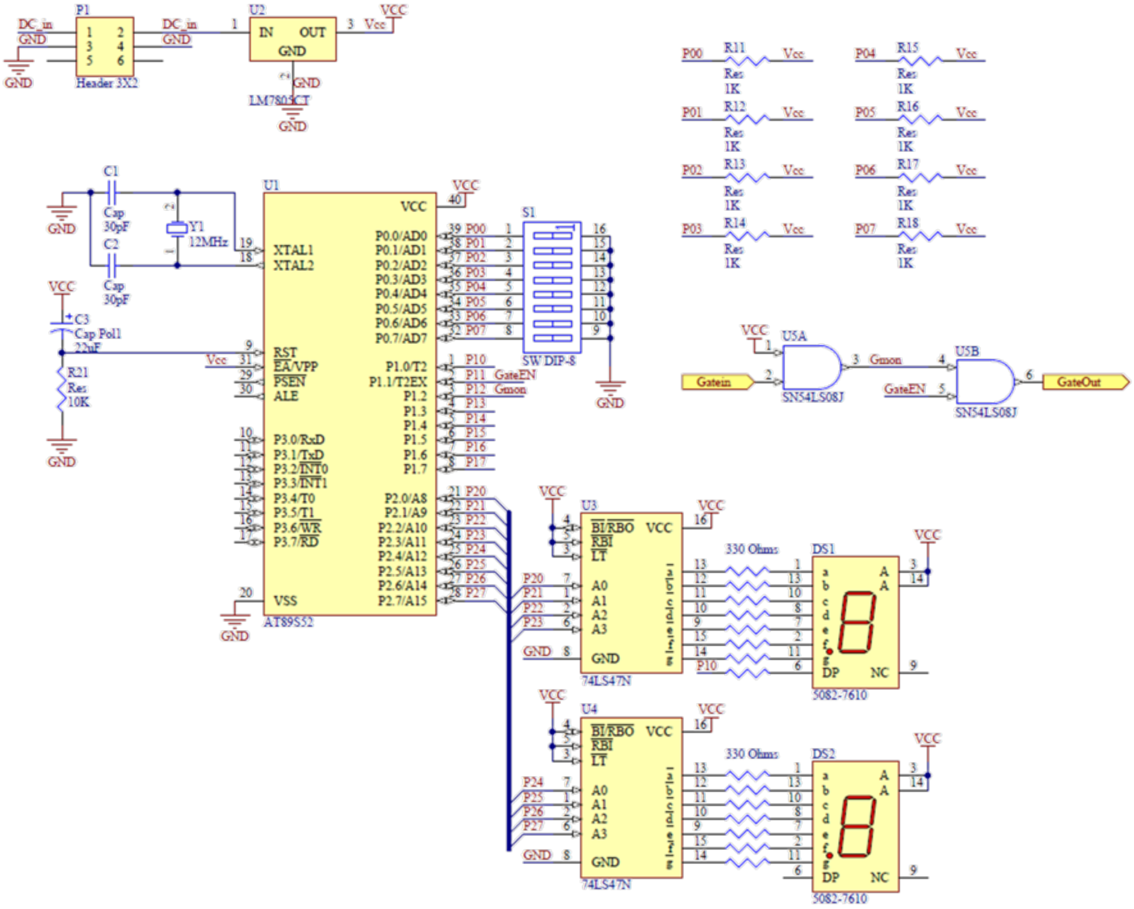

Figure 3.14 Schematic of the Second Stage Amplifier Gate Watchdog. An industry standard 8051 architecture microcontroller, Atmel AT98S52, is used to constantly monitoring the VGS control of the second stage amplifiers, which could cause catastrophic failures if not operated properly. For user interface, it uses a (Dual In-line Package) DIP switch to allow users to set the desired limit. A two-digit seven-segment LED display is used to display duty cycles in real time, or display error codes if any of the set limits is exceeded. Middle right side shows the interface to the input and output VGS control line.

Table 3.1 DIP Switch Settings for Second Stage Amplifier Gate Watchdog. Three bits are used to set the maximum allowed duty cycle and another three bits are sued to set the maximum continuous on time, while two extra bits are reserved for possible future upgrades. Details of the settings are shown in Table 3.2 and 3.3.

1	2	3	4	5	6	7	8
Duty cycle limit			Max on time limit			Reserved	

Table 3.2 DIP Switch Settings of Maximum Duty Cycle for Second Stage Amplifier Gate Watchdog.

3	2	1	Hex Value	Max allowed duty cycle
OFF	OFF	OFF	0	1%
OFF	OFF	ON	1	2%
OFF	ON	OFF	2	5%
OFF	ON	ON	3	10%
ON	OFF	OFF	4	15%
ON	OFF	ON	5	20%
ON	ON	OFF	6	25%
ON	ON	ON	7	30%

Table 3.3 DIP Switch Settings of Maximum Continuous On Time for Second Stage Amplifier Gate Watchdog.

6	5	4	Hex Value	Max allowed on time
OFF	OFF	OFF	0	10ms
OFF	OFF	ON	1	25ms
OFF	ON	OFF	2	50ms
OFF	ON	ON	3	100ms
ON	OFF	OFF	4	250ms
ON	OFF	ON	5	500ms
ON	ON	OFF	6	1000ms
ON	ON	ON	7	2000ms

During operation, the decimal point will flash, as an indicator that the watchdog is working properly, and the current duty cycle will show in the unit of percentile. If any one of the set limitations is exceeded, the output is disabled immediately and the seven-segment display will show the error corresponding code, and the decimal point will remain light up. Error message “c1” means that duty cycle limit is exceeded, while “c2” indicates that the maximum on time limit exceeded. The only way to resume the watchdog is the user pressing the reset button located next to the seven-segment display.

III.9 TR Switches

A set of 64 T/R switches and preamps connect the coil to the parallel transmitter and receiver. The T/R switches use MicroSemi's reference design circuit found from the UM9401 PIN diode data sheet. The circuit diagram is copied into Figure 3.15. This design can also be found in many other places and is commonly used for T/R switch designs.

The design has low parts count and complexity, which helps to keep cost and size down. Two PIN diodes are used in this circuit. When a DC current is applied, the DC current passes though both PIN diodes, allowing RF to go though both of them. RF from the Antenna port, as labeled in the figure which would be RF coil for MRI, RF goes to the transmitter port. D2 also conducts, but the antenna port sees an open circuit instead of a short circuit because of the quarter wavelength cable used. D2 also short the input to receiver, protecting the receiver from potentially high power from transmitter. When the DC supply is reverse biased, both PIN diode are open for RF, so the antenna port is connected to the receiver.

Each of the 64 T/R switches is enclosed in an individual box to reduce possible coupling and to improve heat dissipation. Actual photo of one of the T/R switches is shown in Figure 3.16.

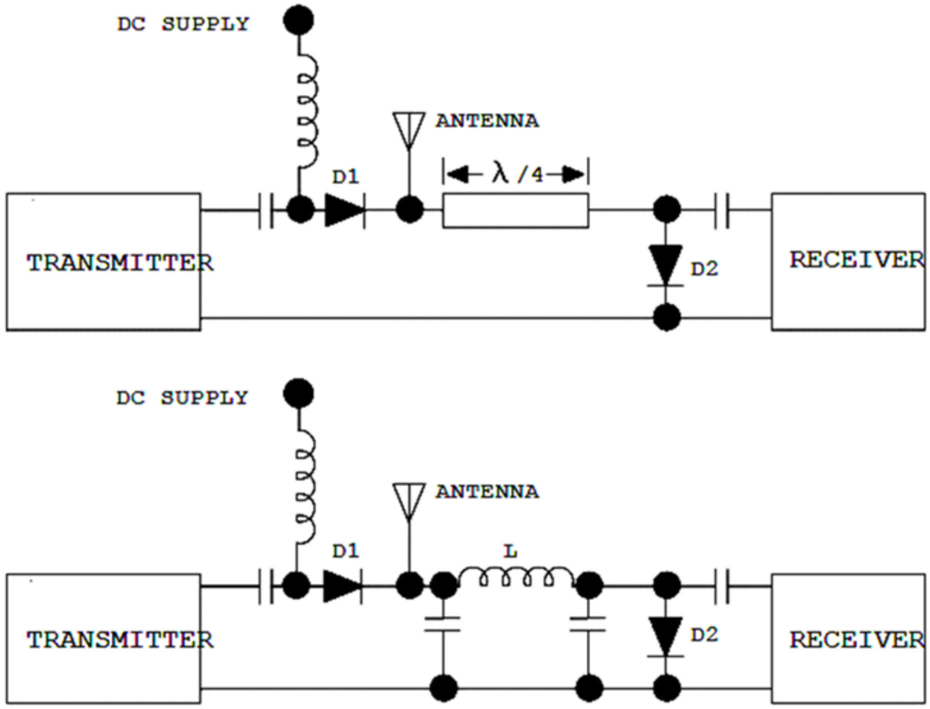

Figure 3.15 T/R Switch Reference Designs Found from the Datasheet for MicroSemi UM9415 PIN Diode. The design on the top part uses a quarter wavelength transmission line while the design on the bottom replaces the transmission line with lumped elements. The principles of operation are identical, based on the fact that a quarter wavelength transmission line transforms an open circuit into a short circuit and vice versa. The design on the top of the figure is easier to implement for testing purposes, while the one on the bottom is easier to implement for large arrays. Cost is also reduced by choosing this design. Here, $L = Z_0 / (2\pi f_0)$ and $C = 1 / (2\pi f_0 Z_0)$.

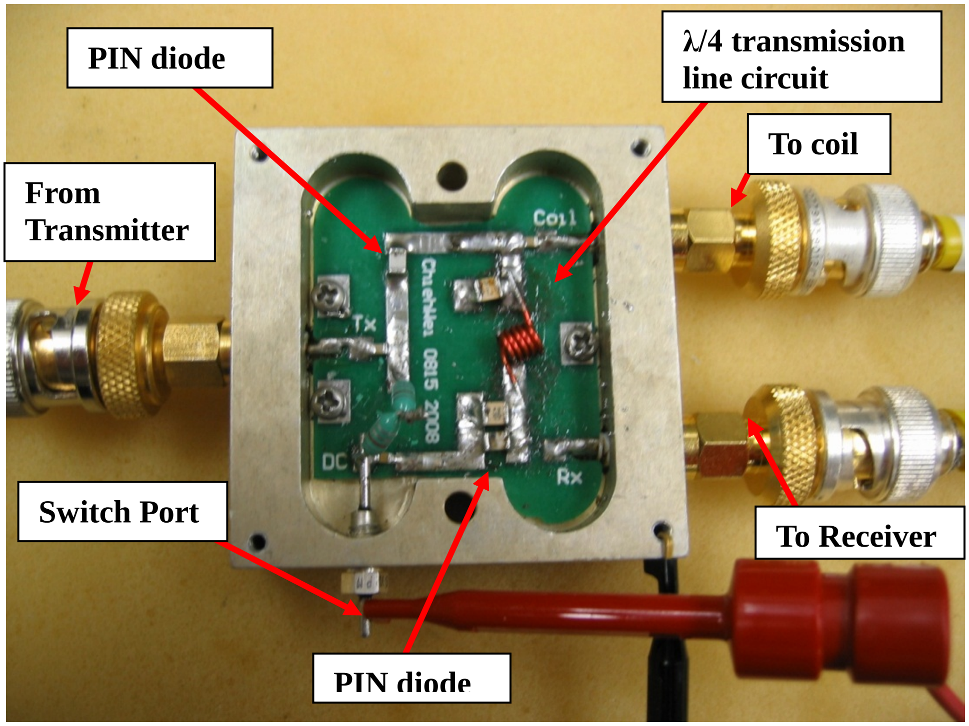

Figure 3.16 Photo of a T/R Switch. The top cover is removed to show the inside circuit shown in Figure 3.15. The design is based around two Microsemi UM-9401 PIN diodes. Each of the enclosure has only one TR switch included. Switching time was measured to be about 3μs. Insertion loss was measured to be about 0.2dB. 27dB isolation between transmit and receive ports were achieved using this circuit. Test hooks are shown in this picture for power supplies. These test hooks are replaced with soldered wires in the final operational states. The quarter transmission line was achieved using lumped elements, which could be replaced with an actual coaxial cable.

III.10 Preamplifiers

The preamplifiers uses Mini-Circuit’s Gali-74 monolithic 50Ω matched amplifier. The given reference design, which is shown in Figure 3.17, has been used with added back to back protection Schottky diode at the input. A Schottky diode has a low forward voltage drop and has a very fast switching time, commonly used for protections in MRI systems. This protection is very important in MRI applications because the transmitted power is easily 100dB higher than the received signal at the input.

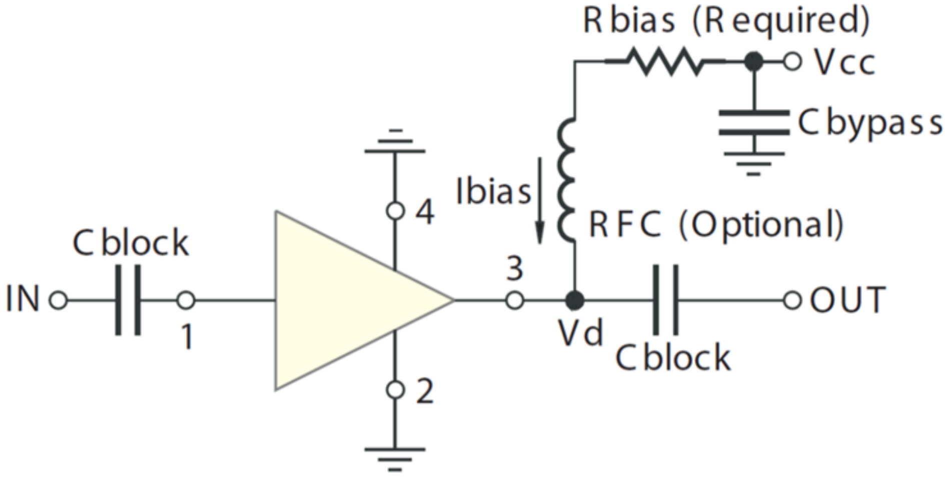

Figure 3.17 Reference Design of Mini-Circuits Gali-74+ Monolithic Matched Amplifier from Datasheet. This is the design that is actually used in the construction, except for added protection.

The amplifiers are each placed in an enclosure to simplify later debugging and testing issues, as well as avoiding possible couplings and overheating issues. Figure 3.18 bellows shows an actual photo of one of the 64 preamplifiers.

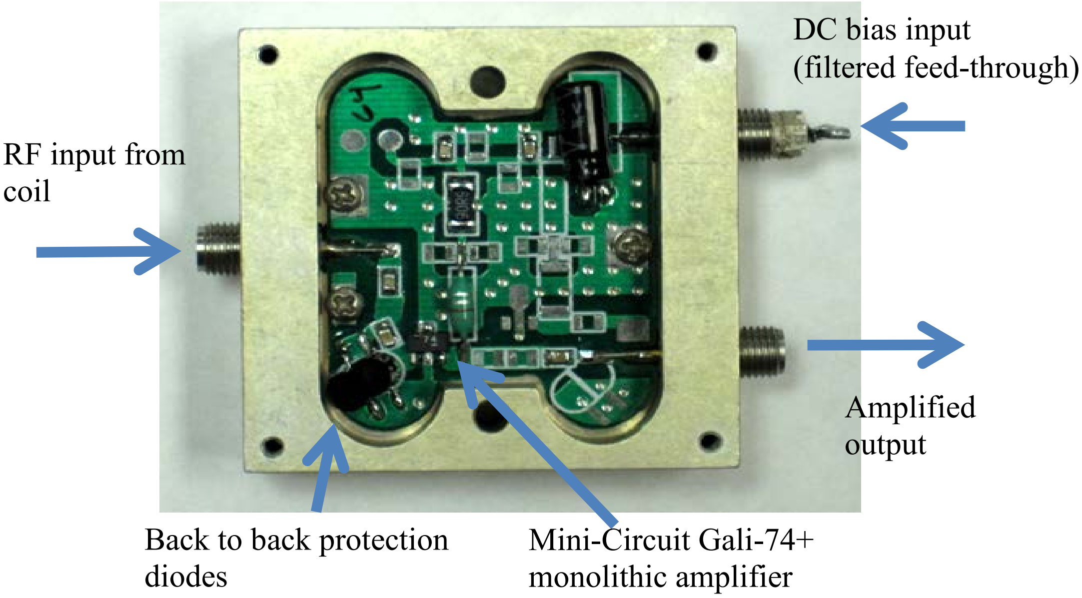

Figure 3.18 Photo of a Preamplifier. The cover is removed to show the inside circuit. Individually shielded boxes minimize possible cross talks. Mini-Circuits Gali-74+ monolithic gain block is used, which greatly simplified the designs. Low pass feed-though filter on RF shielding box is used to filter out possible noises from power supply lines. MBD301 back-to-back protection diodes are used to provide protection to the amplifier especially during transmit window.

III.11 Receiver

The receiver was previously designed and constructed. The 64-channel system receiver contains the main receiver module and an acquisition control computer, as shown in Figure 3.19. Note that the preamplifiers are now replaced with the ones described in Section II.10 of this dissertation because of some stability issues with the previous design. More details should be found in [24, 28].

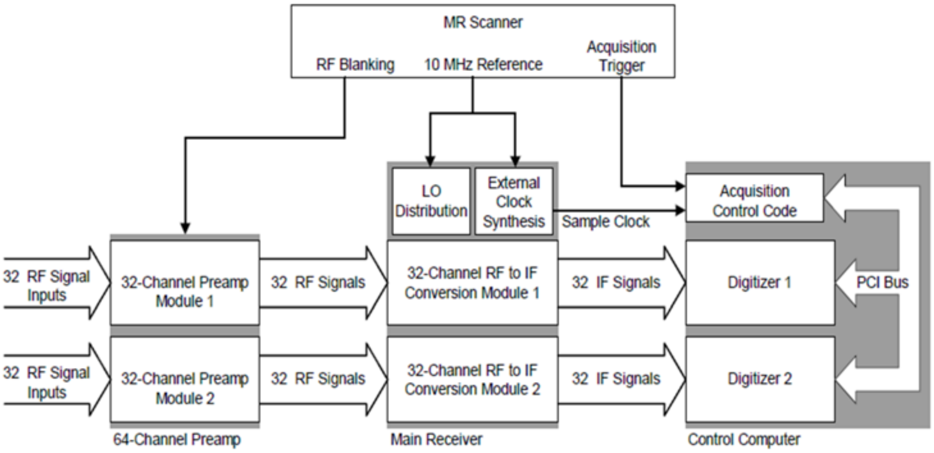

Figure 3.19 Block Diagram of the 64-Channel Receiver. Reproduced from David Brown’s PhD Thesis. The MR scanner provides the phase lock for the receivers. RF signals are mixed down to IF stage before going to 64 channel digitizer. Quadrature demodulation is performed by in the digital domain by DSP or the CPU. The preamplifier module have been replaced because of stability issues. The RF blanking signal is no longer needed. A passive circuit is used for protections.

III.12 Power Supplies and System Integration

Power supplies for the system are all commercially available DC supplies with hardware protection interlocks added. The interlocks prevent the system from being powered on in an order that may cause damages and also ensure that rest of the software and hardware are powered on correctly before proceeding. There are two primary interlocks, the first is a software interlock that uses one digital line of the USB-6501 to ensure that the vector modulator boards are powered prior to attempting to set the I and Q values and attenuation for the modulators. The second is a hardware interlock that ensures that the amplifiers can only be turned on after the modulators are turned on as well as preventing the 50V supplies that serve as the power amplifiers drain to source voltage from turning on until the rest of the system is powered up. The assembled system fits inside eight enclosures except the 50V power supplies and control box for the second stage amplifiers. The complete 64 channel transmitter system, with static control for the modulators, is housed in a standard 19 inch rack cabinet as shown in photos in Figure 3.20 and Figure 3.21. The computer is a standard desktop, which can be replaced with a rack mount computer. The space is reserved, as shown in Figure 3.20. System connections for power and signals are also illustrated in Figure 3.21.

The only changes made to the existing MR system in order to use it are routing the main RF line and a digital gating line to the parallel transmitter. Beyond this, only AC power connections are needed. A single 20A, three phase service is needed for the high power 50V DC supplies, and a standard 15A single phase connection is needed for the remainder of the equipment. This allows for installation of the system with very few changes to the site and relatively manageable infrastructure requirements. Finally, the T/R switches and preamps connect the 64 channel receiver that was previously constructed[12, 19] for use with SEA imaging. This makes a complete, parallel transmit/receive system.

Figure 3.20 Photo of Transmitter System – Front Side. The complete 64 channel transmit system, with static modulation control s, is contained in three half height 19 inch rack units. DC power supplies, modulators, first and second gain stages are all located in separate enclosures, as shown, to help mitigate noise, coupling, cross talk and instability due to feedback. Labels in the pictures are for: A - Computer running controller software. B - Modulator box including vector modulator boards and digital potentiometer boards. C - First stage amplifiers, in 2 boxes. D - Second stage amplifiers, in 4 boxes. E - Power supplies and amplifier watchdog. F: 50V power supplies for second stage amplifiers and controlling circuit.

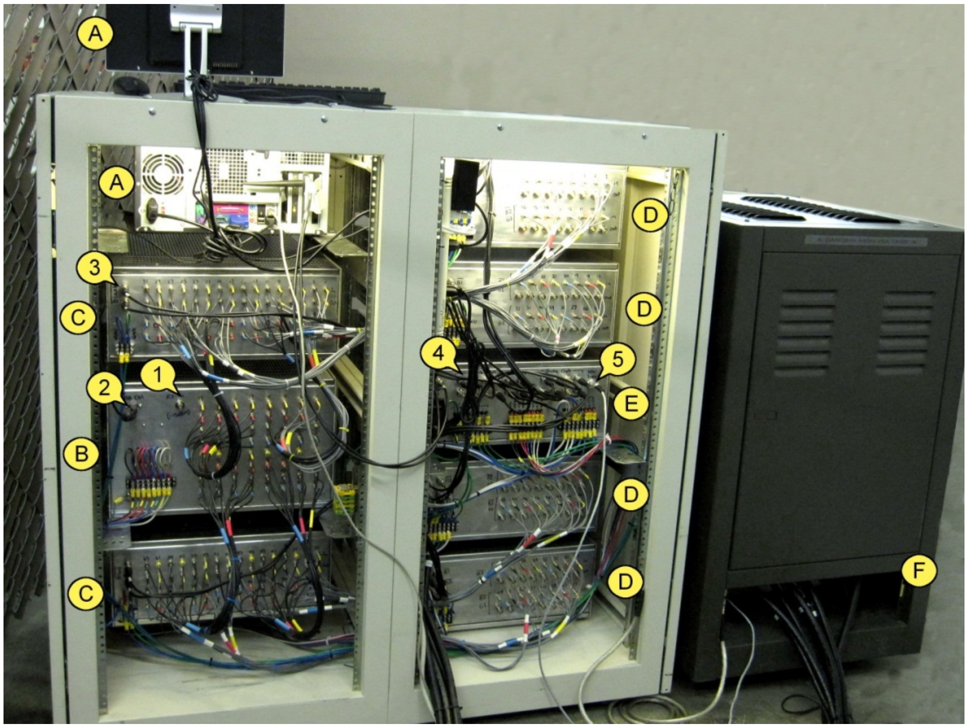

Figure 3.21 Photo of Transmitter System – Back Side. Alphabetical labels A through F correspond to the same labeling as previous figure. Number labels are 1 - System overall RF input. 2 - USB link between computer and modulator box, which includes the digital potentiometers. 3 - Noise blanking for amplifiers. 4 - Gate control through watchdog. 5 - Interlock to disable 50V power supplies when the rest of the system is determined to be not ready.

CHAPTER IV

TRANSMITTER SOFTWARE

With the hardware system ready, software is necessary as human interface, connecting the hardware and human and let the user specify the desired functionality of the hardware. The software was written for controlling the hardware in TR SEA configuration. A totally independent piece of software was also provided to give the system full capability for Transmit SENSE which will be briefly introduced. Testing software is described in Chapter VI.

IV.1 TR SEA Controller Software – Linear Correction Version

The TR SEA controller software was developed using Microsoft Visual Basic 6.0. The choice of programming language was because some previous work done for digital tuning was done using Visual Basic. It was determined it would be easier to use some of the source code already available. From a user's point of view, a single compiled EXE file is the only program to use for most application. The interface provides linear magnitude, phase and dB attenuation control to each channel, as well as calibration and normal windows software functionalities, such as save or open settings. Only the most basic functions are covered in this section, while the calibration will be covered in Chapter VI. A screenshot of the software Graphic User Interface (GUI) is shown in Figure 4.1.

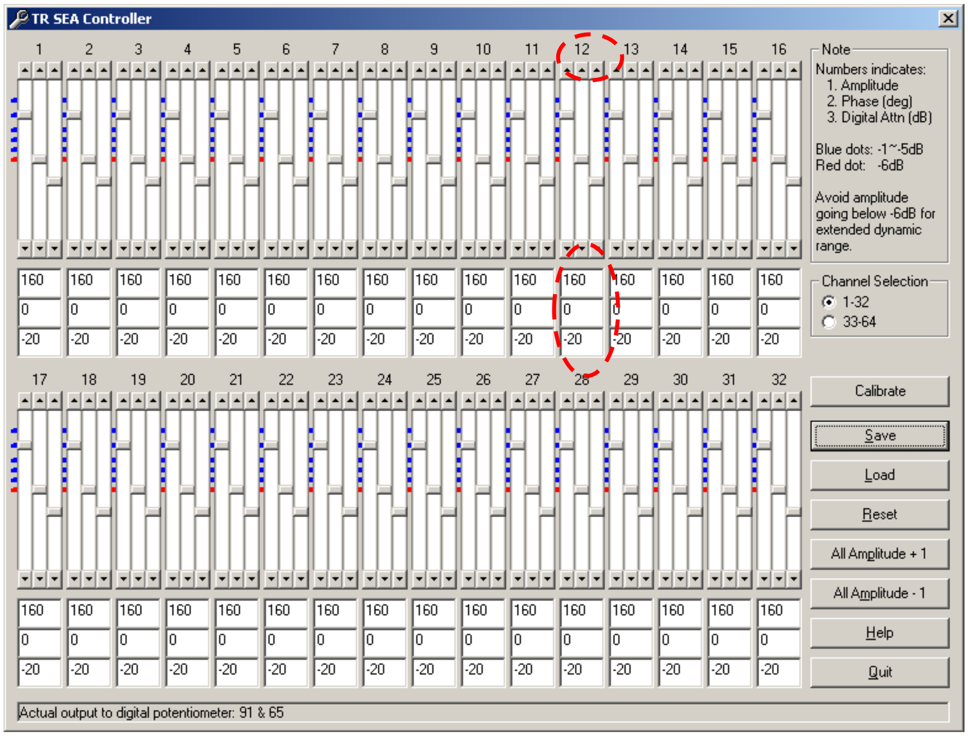

1	2	3	4	5	6	7	8	9	10	11	12	13	14	15	16
160	160	160	160	160	160	160	160	160	160	160	160	160	160	160	160
0	0	0	0	0	0	0	0	0	0	0	0	0	0	0	0
-20	-20	-20	-20	-20	-20	-20	-20	-20	-20	-20	-20	-20	-20	-20	-20

17	18	19	20	21	22	23	24	25	26	27	28	29	30	31	32
160	160	160	160	160	160	160	160	160	160	160	160	160	160	160	160
0	0	0	0	0	0	0	0	0	0	0	0	0	0	0	0
-20	-20	-20	-20	-20	-20	-20	-20	-20	-20	-20	-20	-20	-20	-20	-20

Note
Numbers indicates:
1. Amplitude
2. Phase (deg)
3. Digital Attn (dB)

Blue dots: -1~-5dB
Red dot: -6dB

Avoid amplitude going below -6dB for extended dynamic range.

Channel Selection
● 1-32
○ 33-64

Actual output to digital potentiometer: 91 & 65

Figure 4.1 TR SEA Controller software GUI – Linear Correction Version. In this window, numbers above the sliders are channel numbers. Three sliders and three numbers below are linked together for linear relative amplitude (from 0~200), phase in degrees (-180 ~ 180) and digital attenuation (0 ~ 31dB) of the corresponding channel. In the particular example above, numbers in the red circle means channel 12 has a relative magnitude of 160, phase of 0° and a digital attenuation of 20dB.

This software is even driven. When a user movies the slider or changes values on the slider, the event handler would send the corresponding streams of data to the USB-6501 digital I/O, which does the actual open loop communications to the digital controlled potentiometer board or the digital controlled attenuators depending on which value the user changed on the GUI. The data stream would first encode the address of the corresponding chip, either the digital controlled potentiometer or the digital controlled attenuator. The encoded address is sent to the address decoder on the corresponding board which does the chip selection on the board. Going through the hassle of encoding and decoding of address is because it minimizes the requirement for number of bits in the digital I/O. Afterward, either simulated serial data or parallel data is sent to the corresponding chip to set the wiper position or attenuation.

The settings on the GUI can be saved into an INI file simply by clicking the save button on the GUI, which brings up a standard window to query the location and filename to save. Clicking the load button opens up a window to choose an INI file. The INI file structure is standard so that it can be edited directly using any text editor.

A specific separate file, settings.ini, includes all settings, such as the NI hardware name and calibration data. The structure and usage is closely related to calibration, so it will be covered in Chapter VI.

A problem with this system is linearization. The solution is a new version of software, which is discussed in the next section to address this problem. Basically, the linearization uses 3 points for corrections, zero points, maximum I and maximum Q points. The lookup table expands to arbitrary number of points.

IV.2 TR SEA Controller Software – Lookup Table Version

Later, a new version of the GUI based control software was developed, using lookup tables for linearization purposes, which also features automatic attenuation control. A screen shot of the new software is shown in Figure 4.2. The software was developed using Microsoft VB 6.0, combined a Component Object Model (COM) binary interface developed using MATLAB 2010a.

The software looks at a calibration table, which specifies arbitrary number of points in specified I/Q inputs to the vector modulator, and measured magnitude and phases. The specified I/Q inputs can easily fall into nicely grids. However, here is a reverse lookup. The user specifies a desired output level, and the software looks up for corresponding I/Q levels. A 128x128 lookup table would be too large to implement. Fortunately, MATLAB has a built-in function, called *TriScatteredInterp*, which can be used here to perform interpolation on a scattered dataset that resides in 2D space. The interpolations utilize Delaunay triangulations of the I/Q derived from measured magnitude (dB) and phase (degrees). This produces a surface that is used for the lookup of I/Q levels that need to send to the hardware system. Using the new *deploytool* provided by MATLAB, the lookup function is compiled into a COM component, which is used in the VB program.

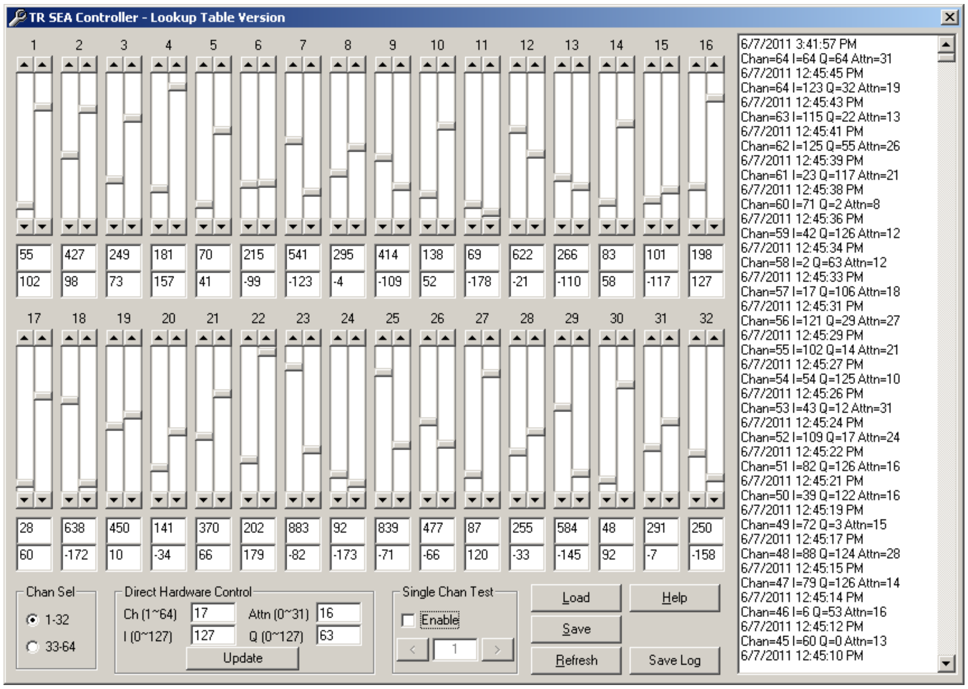

1	2	3	4	5	6	7	8	9	10	11	12	13	14	15	16
55	427	249	181	70	215	541	295	414	138	69	622	266	83	101	198
102	98	73	157	41	-99	-123	-4	-109	52	-178	-21	-110	58	-117	127

17	18	19	20	21	22	23	24	25	26	27	28	29	30	31	32
28	638	450	141	370	202	883	92	839	477	87	255	584	48	291	250
60	-172	10	-34	66	179	-82	-173	-71	-66	120	-33	-145	92	-7	-158

● 1-32
○ 33-64

Ch (1~64) 17
Attn (0~31) 16
I (0~127) 127
Q (0~127) 63

☐ Enable
1

```
6/7/2011 3:41:57 PM
Chan=64 I=64 Q=64 Attn=31
6/7/2011 12:45:45 PM
Chan=64 I=123 Q=32 Attn=19
6/7/2011 12:45:43 PM
Chan=63 I=115 Q=22 Attn=13
6/7/2011 12:45:41 PM
Chan=62 I=125 Q=55 Attn=26
6/7/2011 12:45:39 PM
Chan=61 I=23 Q=117 Attn=21
6/7/2011 12:45:38 PM
Chan=60 I=71 Q=2 Attn=8
6/7/2011 12:45:36 PM
Chan=59 I=42 Q=126 Attn=12
6/7/2011 12:45:34 PM
Chan=58 I=2 Q=63 Attn=12
6/7/2011 12:45:33 PM
Chan=57 I=17 Q=106 Attn=18
6/7/2011 12:45:31 PM
Chan=56 I=121 Q=29 Attn=27
6/7/2011 12:45:29 PM
Chan=55 I=102 Q=14 Attn=21
6/7/2011 12:45:27 PM
Chan=54 I=54 Q=125 Attn=10
6/7/2011 12:45:26 PM
Chan=53 I=43 Q=12 Attn=31
6/7/2011 12:45:24 PM
Chan=52 I=109 Q=17 Attn=24
6/7/2011 12:45:22 PM
Chan=51 I=82 Q=126 Attn=16
6/7/2011 12:45:21 PM
Chan=50 I=39 Q=122 Attn=16
6/7/2011 12:45:19 PM
Chan=49 I=72 Q=3 Attn=15
6/7/2011 12:45:17 PM
Chan=48 I=88 Q=124 Attn=28
6/7/2011 12:45:15 PM
Chan=47 I=79 Q=126 Attn=14
6/7/2011 12:45:14 PM
Chan=46 I=6 Q=53 Attn=16
6/7/2011 12:45:12 PM
Chan=45 I=60 Q=0 Attn=13
6/7/2011 12:45:10 PM
```

Figure 4.2 TR SEA Controller software GUI – Lookup Table Version. In this window, numbers above the sliders are channel numbers. Two sliders and two corresponding numbers shown in text boxes below the sliders are used to control the relative RF linear magnitude (from 0~1000) and phase in degrees (-180 ~ 180). Digital attenuation controls are applied automatically (0 ~ 31dB) to the corresponding channel.

Another fundamental difference is that the attenuation slider is removed. An automatic attenuation control is implemented, which tries to use the maximum attenuation and I/Q values that fall in the hardware limit of 0 to 127. A new log box is also provided for convenience to see what the hardware and software have performed, which could be useful for debugging purposes.

IV.3 Transmit SENSE Software

When configured in transmit SENSE mode, the system uses NI DAQ boards instead of the low speed digital controlled potentiometers. Also, the software will send out waveforms instead of fixed DC values. Because of the significant differences, another software package is needed instead of simple modifications. MATLAB is chosen here instead of Visual Basic because it provides easy interface to NI DAQ analog waveform generators. More importantly, many of the data preparations are normally done in MATLAB. A program written in the same computer language would provide an easier interface.

In transmit SENSE, each channel requires a completely different RF pulse. A dynamic control system is needed with high bandwidth analog signal available for each I and Q input of the modulators. Direct comparisons with MR images indicate that a bandwidth of 100 kHz which corresponds to a sample rate of 200 kHz would be enough, which is easily available from commercial DAQ systems. A 40-pin header connector on each vector modulator card directly exposes the I and Q inputs as well as the digital lines to control the step attenuators so that this system can be easily implemented. This interface was designed to mate with National Instruments Data Acquisition (DAQ) cards directly, in particular the NI PCI-6713. However, this connection is standard to many of the older NI DAQ cards, so switching to other cards, if necessary, would be simple. The PCI-6713 has eight analog output channels, as well as eight digital lines, which is sufficient to control up to four transmit channels at once. Each analog channel will operate at a maximum of 720kS/sec simultaneously, exceeding the minimum bandwidth requirements for the control system.

This MATLAB program has two major parts. First is to control the digital controlled attenuators and second part deals with analog waveform playback. The first part of the function uses DAQ card's digital output capability to set the digital attenuation for rough level controls. The second part of the function deals with DAQ card's analog output capability. It sets trigger source, buffer configuration and sampling rate before sending the waveforms to the system buffer. Once a digital trigger is received from the MR system, the waveform is immediately played out, modulating the user specified RF waveforms. Using digital trigger instead of software trigger minimizes the delays between the trigger and the actual waveform output. Most ideally, this should be done using a more expensive DAQ system which has phase lock with the MR scanner. However, this phase lock is not necessary because the RF phase is controlled mainly by the scanner. The added phase shift by the modulator is a slow varying signal so a tiny shift does not normally bring noticeable effect.

The primary difference between the static controller software and dynamic controller software is the waveform playback instead of setting the potentiometer values. The dynamic controller converts the amplitude and phase waveforms to I and Q waveforms suitable for the modulators, then sets the modulators step attenuators and waits for a digital trigger (normally the gating signal used for the amplifiers). When the trigger is received the I and Q waveforms for each channel are played back simultaneously. These waveforms modulate an RF hard pulse that is supplied by the MR system.

CHAPTER V

TRANSMIT B1 FIELD PATTERN SYNTHESIS

Simulations have been performed for the transmit pattern in this research. The purpose of the simulations are for transmit B1 field synthesis. It turns out to be a very useful method in dealing with the SEA coil array. Results show that an optimal phase shift between neighboring channels exists for optimal penetration depth and B_1 filed homogeneity, assuming the same power is used for excitation for each channel. The simulations are based on Biot-Savart law. Various phase offset are simulated in search of the optimal point. Planar and cylindrical formed planar pair coil arrays are both calculated and later imaged using real MR experiments for verifications and good agreements are shown. Results show that near the coil excitation field can be synthesized by using inter-coil phase shift while keeping the same amplitude. Slice of excitation can be synthesized near the array, and the distance from the surface array can be manipulated by varying the transmitted power.

V.1 Introduction

MRI transmit arrays has been used mainly to overcome the B1 homogeneity problem in high field MRI. When the array becomes even larger, RF transmit field can possibly be manipulated without complicated pulse sequences. This is similar to a phased array used in antenna systems, except that near field is used instead of far field.

While full wave simulation software packages are widely available today, either commercial or open source, they are often too expensive or difficult to use. More importantly, full wave simulations are often too time consuming and thus not suitable for large arrays. Quasi-static or static simulations can be used when full wave effects can be safely ignored. In a planar pair array, as used in Single Echo Acquisition (SEA) imaging, the magnetic field pattern is limited to the near field, decaying quickly in the far field, making it great for quasi-static or static simulations. The simulation in this study uses a MATLAB (MathWorks, MA) program developed in house based on magnetic field generated by a finite length of wire calculated from static Biot-Savart law. The source code used for this calculation can be requested directly from the authors.

In a transmit planar pair array, which was used for Transmit / Receive (TR) SEA [5], at distances very close to the array, the main contribution to the transmit field is from the coil just below it. Contributions from other channels can be safely ignored because they are much smaller. However, at a distance that is comparable to the coil to coil distance, contributions from nearby channels are on the same order as that from the one below it. In this case, the transmit sensitivity must be considered as the sum of that from all individual components of the array. Figure 5.1 (a) and (b) illustrate the transmit sensitivity of an array of three planar pair coils with fields calculated at different distance from coils. To have the maximum transmit sensitivity at a certain point without increasing the transmit power, i.e., to have maximum transmit efficiency, we want the transmit field from all coils to be in phase at that point. This can be achieved by phase shifting the transmit signals applied to adjacent coils. Figure 5.1 (b) and (c) illustrates the effects of such a phase shift. However, the required phase shift is location dependent. Figure 5.1 (c) and (d) illustrates the effects of the same phase offset at different location. To have the maximum transmit efficiency in a volume is more complicated and thus a numerical method is helpful.

V.2 Theory and Basis of Simulation

Biot-Savart law describes the magnetic field generated by a short segment of wire carrying electric current. To find the magnetic field generated by a segment of straight wire carrying current, integrating over the finite length is required. The integration result has been discussed in various texts such as [47] with simple analytical result. The magnitude is shown in Eqn. 5.1.

$$|B| = \frac{\mu_0 I}{4\pi d}(cos\,\varphi_1 + cos\,\varphi_2) \qquad \text{[Eqn. 5.1]}$$

Figure 5.2 shows a diagram of the magnetic field and the definitions of the parameters used in Eqn. 5.1. Here, φ_1 is the angle between two lines, the first being the line between the observation point and the start point of the straight wire, the second line being the straight wire. φ_2 is defined in a similar way, except that the start point is changed to the end point. The direction of the magnetic field from the straight wire can be determined using the right hand rule. This will be the underlying theoretical basis that is used for all the simulations in this paper.

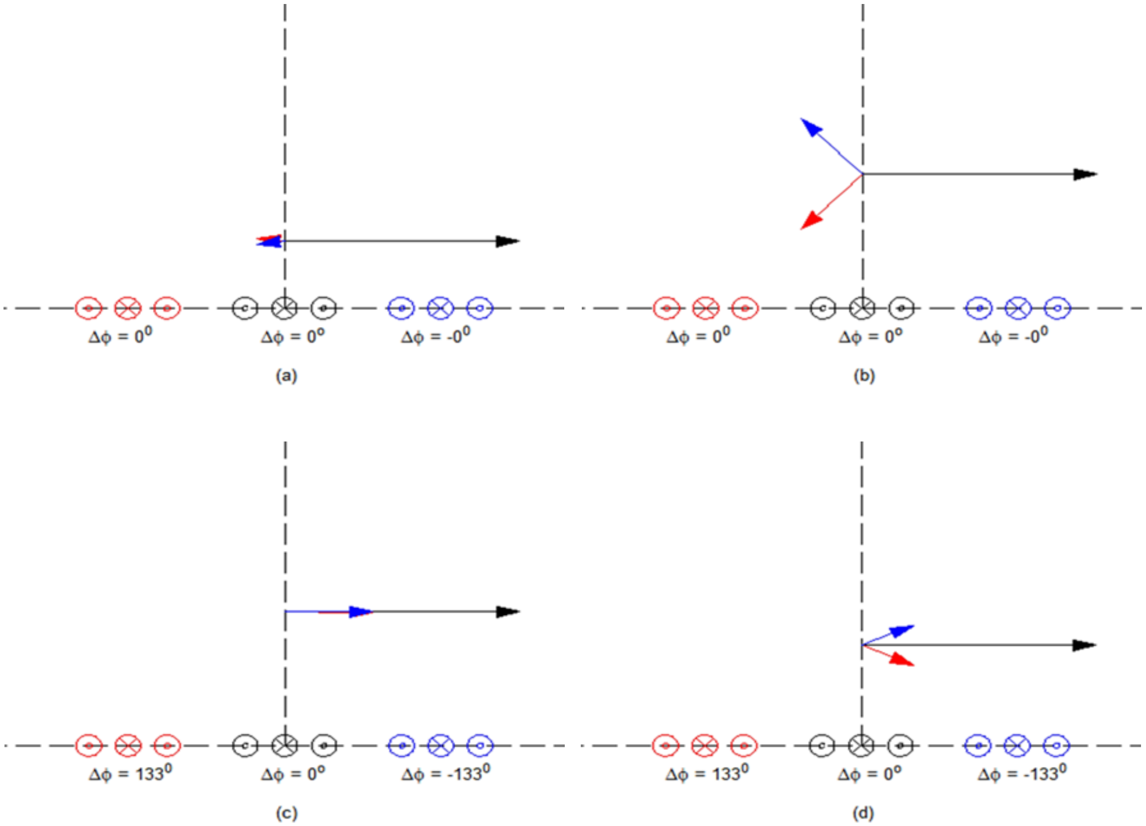

Figure 5.1 Excitation Field of Three Planar Pair Coils above the Center Element at Different Distance from the Array and Different Phase Ramp. Each coil has its own color, and corresponds to the arrow with the same color. At 0.5D (a), where D is the distance between centers of neighboring channels, the excitation is mainly contributed by the coil just below it. However, at 1.0D (b), excitations from other channels are no longer ignorable. By applying a linear phase ramp of -133 (c) and keeping the same location as (b), the red and blue vectors are rotated, and the vectors are aligned and the sum is maximized for this point. However, this optimal offset is dependent on the location. (d) shows the effects of the same phase ramp at a different location (0.75D from array), which is not optimized.

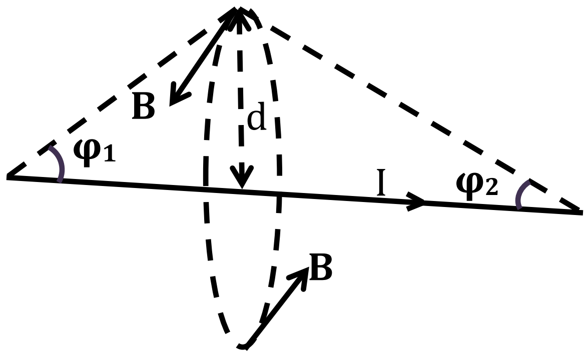

Figure 5.2 Magnetic Field around a Piece of Straight Wire with Finite Length. The magnetic field produced from a finite length straight wire, labeled as I in from the figure, can be calculated using current flowing through it and two angles, labeled as φ_1 and φ_2. Figure adapted from: http://faculty.wwu.edu/vawter/PhysicsNet/Topics/MagneticField/MFStraitWire.html

V.3 Simulations Preparation

The program was written using MATLAB in an object oriented approach. A *straightwires* class is first defined which works as the core of the whole computer program. An object derived from this class has a source space, which defines the two end points for each piece of wire in 3D Cartesian coordinates and the electrical current that flows through each piece of the wires. The object can be either a single wire or a group of wires. For DC or frequency excitations, the currents are real numbers, flowing from the starting points to the corresponding end point for each piece of wire. The currents are complex numbers when the source of excitation is RF instead of DC. The complex numbers carry information of both amplitude and phase of the current. To construct an object derived from the *straightwires* class, only one line is needed in MATLAB:

wires = stragightwires(sp, ep, i) [Eqn. 5.2]

where sp defines the starting points and ep for ending points. The two matrixes here must have the same size, N by 3, where N is number of segments for wires which carry current. The first column of the sp or ep matrix defines the x coordinates, the second and third are for the corresponding y and z coordinates. The i matrixes must be N by 1 in size.

With the sources of current defined, a problem space is required which defines a matrix of points for magnetic field calculation. A class method, bfield, is defined to calculate the magnetic field at the problem space generated by the currents defined in the source space. To calculate the magnetic field generated by wires at 3D coordinates of location, one line is needed

B = bfield(wires, location) [Eqn. 5.3]

where wires is previously defined using the straightwires class constructor and location is the is a 3D matrix with size of P by Q by 3. The first page of the 3D matrix is for x coordinates, the second and third pages are for the corresponding y and z coordinates. The result matrix returned by the bfield method, B, has the same dimension as the input variable location. First page of the matrix defines x components of the magnetic field, Bx. The second and third pages are for the y and z components, By and Bz.

The *straightwires* class works for general Biot-Savart magnetic field calculations. For MRI, it can be used for both main magnetic field and gradient field calculations directly. When full wave effects can be safely ignored, B_1 field of a coil or an array can be simulated using this program. Magnetic field in the transverse plane (xy plane) contributes to the B_1 field. The z component of the magnetic field does not contribute to B_1 and can be ignored safely. The two components of the B_1 field transmit B_1 field, normally labeled as ${B_1}^+$ for transmit and ${B_1}^-$ for receiving, can be calculated using

$$\mathrm{B_1}^+ = \frac{\mathrm{B_x}+\mathrm{j}\mathrm{B_y}}{\sqrt{2}} \qquad \text{[Eqn. 5.4]}$$

and

$$\mathrm{B_1}^- = \frac{\mathrm{B_x}-\mathrm{j}\mathrm{B_y}}{\sqrt{2}} \qquad \text{[Eqn. 5.5]}$$

Since the currents are RF expressed in complex scalars to carry both phase and amplitude, B_x and B_y calculated using Eqn. 5.1 are also complex scalars. ${B_1}^+$ and ${B_1}^-$ are both complex scalar field, containing amplitude and phase of the transmit or receive patterns. The transmit $\mathrm{B_1}$ field, $\mathrm{B_1}^+$ calculation is used in this chapter, but later the ${B_1}^-$ will also come into play for TR system, which is discussed in Section VII.5. For this chapter, however, only the transmit filed is of interest.

V.4 Simulations Setup

With the *straightwires* class fully defined above, the program is relatively simple. All needed is constructing the planar pair array coil geometry in the simulations. A planar pair array uses only straight wires without any curved structures. This makes the geometry much easier to construct because if curves exist, they need to be broken into segments of straight wires. Geometries are defined to be the same as the arrays actually used for SEA imaging. Two designs are simulated. Each one has equal size and spacing across all 64 coil elements. To construct the coil geometry in the program, starting and ending points for each element of each coil is defined. Currents are also defined for each segment of each coil in a complex way to include phases.

Figure 5.3 and Table 5.1 shows the geometry and dimensions used in the simulations, where W is for coil width, L for coil width and D for neighboring coil to coil distance, all numbers show are in the unit of mils (1/1000 inch), which is standard in printed circuit board.

Later, actual MR images were acquired using planar pair arrays using the exact dimensions as the simulations, which were shown in Figure 5.3 and Table 5.1. The images and the simulation are then directly comparable.

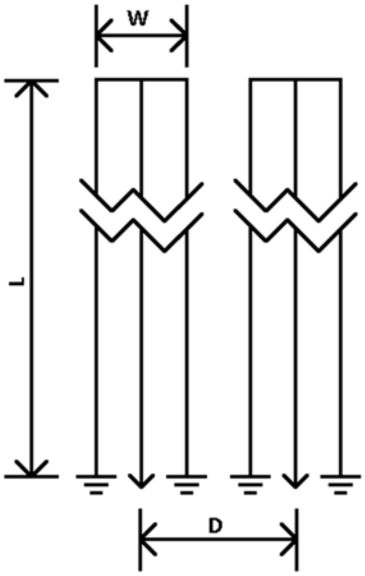

Figure 5.3 SEA Coil Geometry Used in Actual Coils and Simulations. For simplicity, only two channels are shown here. The actual arrays used have 64 channels. Each element of the array is long and narrow, so it is truncated in the long direction in the drawing.

Table 5.1 SEA Coil Dimensions Used in Simulations.

Case	**W (mil)**	**L (mil)**	**D (mil)**
Planar	60	2980	80
Flexible	130	2870	160

Two cases will be discussed, planar formed and cylindrical formed. The array is placed in such a way that the array elements are aligned with the main magnetic field (z direction) in both cases. In the planar case, the array is placed in the xz plain with a phantom placed directly above it, like commonly done in SEA imaging. In the cylindrical case, the array is wrapped around a cylindrical phantom. For both cases, the currents on the 3 vertical elements are exp(jφ), -2·exp(jφ) and exp(jφ), where φ is the phase of RF excitation at the feeding point of the coil. There is a factor of -2 in the middle element because it carries double the current as compared with the two returning paths, and the direction of the current is opposite to the other two elements because we define the start z and end z to be identical for all the three elements. This calculation gives the "normalized" B_1 field because 2 amps of current are assumed to be flowing in each coil.

For problem space, the simulations will calculate the ${B_1}^+$ field in a slice in the middle of the array. For planar case, the Field Of Interest (FOI) is just above the array. For cylindrical case, the FOI is inside the array.

Figure 5.4 illustrates the array and the area for calculation in the planar case. The field map was calculated using 0° phase ramp. The pseudo colored rectangle area is the FOI, or problem space as referred to earlier. Cylindrical case setup is not illustrated here, but it looks very similar.

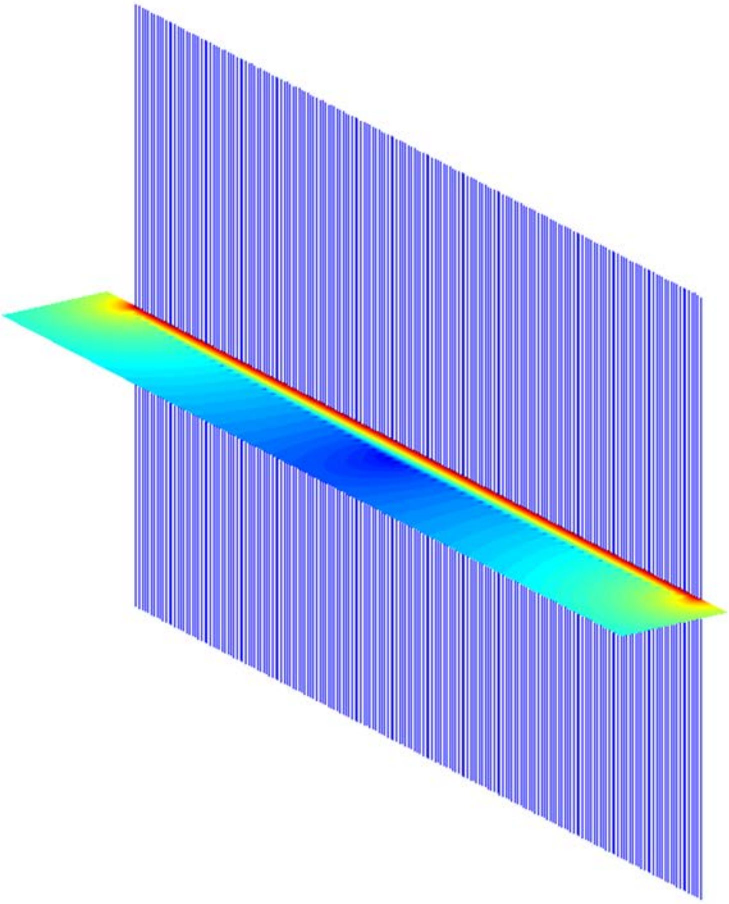

Figure 5.4 Simulation Setup for Planar Case together with B_1 Field Map in Log Scale. The blue vertical lines are the coils. The colored area is the ${B_1}^+$ field calculated, shown in log scale.

Instead of B_1 field, it is often desirable to show simulated MR images assuming uniform receiving coil pattern. This would be useful for easy comparison to actual results to verify the simulation result, as performed in this study. Simulated MR images can be derived from ${B_1}^+$ field using:

$$Image = k_1|\sin\alpha| = k_1\left|\sin\frac{\pi\cdot {B_1}^{+}}{{B_1}^{+}{}_{\pi}}\right| = k_1\left|\sin\left[k_2\cdot\sqrt{P}\cdot {B_1}^{+}\right]\right|$$

where α is the flip angle, ${B_1}^{+}{}_{\pi}$ is the ${B_1}^{+}$ field strength which makes 180° flip to the spins. Since ${B_1}^{+}$ field is proportional to the current flows on the coils, it is proportional to the square root of power, P given by the transmitter. In this simulation, we just combine all the constants to be k_2 for convenience. The studies are for relative power levels, given in dB to get rid of the k_2 constant.

V.5 Planar Case Simulation Results and Experimental Verifications

FOI was defined to be 142mm by 16.3mm, with a resolution of 0.2 mm in each direction in the simulation. Colored area in Figure 5.4 is the actual ${B_1}^{+}$ filed shown in log scale with zero phase shift across nearest neighbors.

The array has a total width that is actually a little bit wider than the array, so that the “edge effect” can be seen. Across nearest-neighbor coil element phase shift of 0° to 355°, with step of 5° are simulated. Simulated imaging results for 0°, 180°, 320° and 40° are shown in Figure 5.5. The result might seem counter-intuitive that the optimal is neither 0° nor 180° that one might envision initially but around 40° for the coil with the geometry specified in Table 5.1. This value is related with the coil geometry.

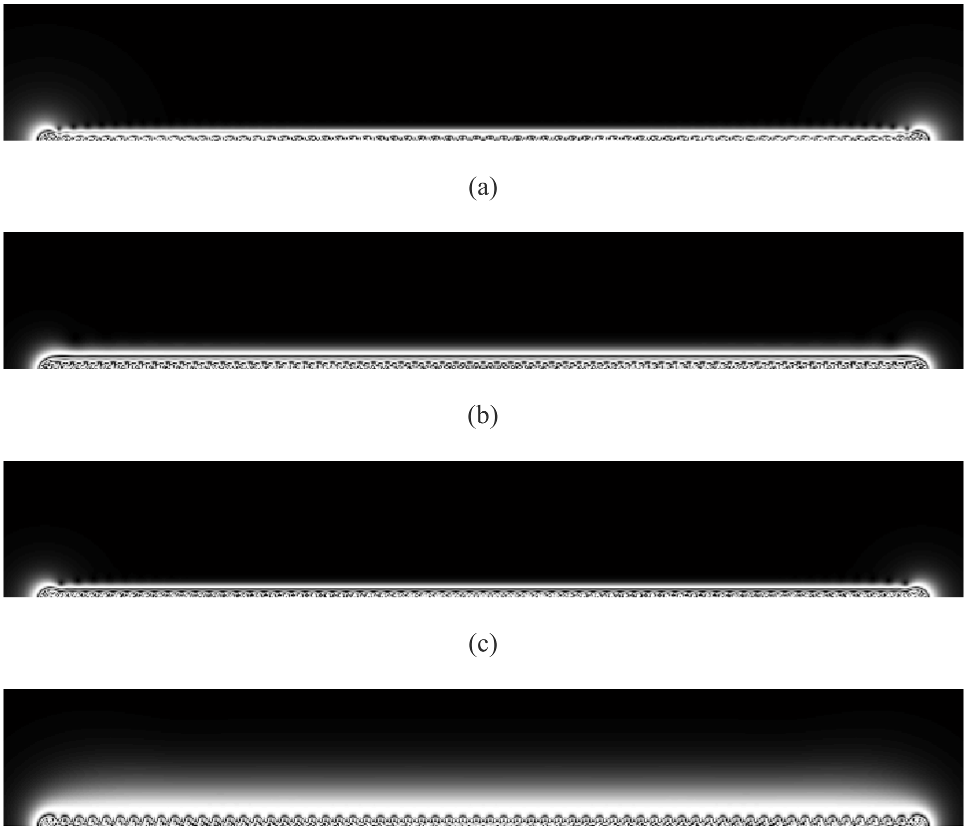

(a)

(b)

(c)

(d)

Figure 5.5 Simulated Images for Planar Formed SEA Array, with Different Phase Offset across Nearest Neighbors. By manipulating the phase shift across nearest neighbors, the transmit image can be optimized for penetration depth or uniformity in certain regions. The phase offset was set to be (a) 0°, (b) 180°, (c) 320° and (d) 40°.

For verification, the simulation results are then compared directly to the actual MR imaging results, using an array with the same dimensions as used in the simulation. A photo of the planar transmit planar pair coil array with a uniform phantom is shown in Figure 5.6. A flat container is filled with 1 gram per liter $CuSO_4$ doped agarose gel as the phantom used in this experiment. The whole setup is placed inside a parallel plate volume coil (not shown in the picture) for receiving. This setup is very similar to SEA imaging the only difference being that transmit and receive coils are reversed and we call it “Reverse SEA”.

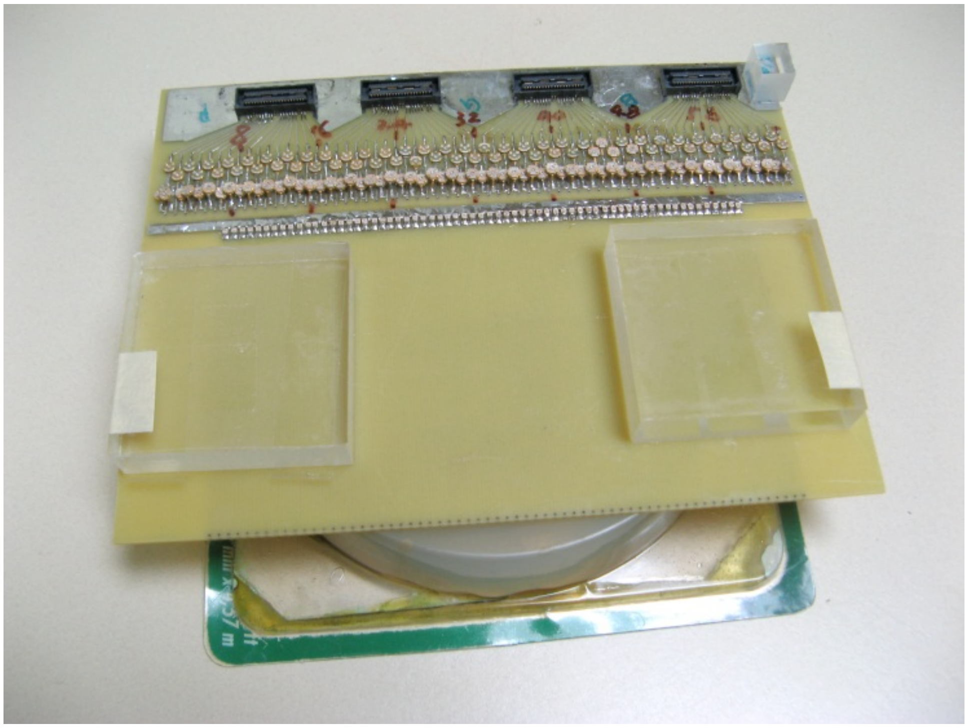

Figure 5.6 Planar SEA Coil Array and Uniform Phantom. The traces of the coil elements are on the bottom side of the FR4 board and thus can’t be seen in the picture. The whole setup is placed inside a parallel plate volume coil, which is not shown either.

A standard spin-echo sequence is used for the verifications. The “90 degrees” pulses are transmitted using this surface array, while the 180 degrees pulses are transmitted using the volume coil. Please note that the actual transmitted “90 degrees” pulses have different flip angles across the phantom and thus the quotation make here. The 180 degrees pulses produce actual 180 degrees spin flips across the phantom assuming the volume coil is uniform enough. Imaging results using this setup are shown in Figure 5.7, confirming the simulation results.

V.6 Cylindrical Case Simulation Results and Experimental Verifications

Simulations for the cylindrical case are very similar to planar case. A flexible SEA coil array is wrapped around a cylinder. The simulations are only interested in the filed inside the coil. Result from outside has been simply masked out. The flexible SEA array used in this simulation is just about double comparing to the planar SEA array. As a result, similar results are developed. Simulated imaging results for 0°, 180°, 40° and 320° nearest neighbor phase shift are shown in Figure 5.8. Still 40° gives the optimal penetration depth.

Similarly, the cylindrical case is verified using MR images. The experiment setup is shown in Figure 5.9. A birdcage coil is used to replace the parallel plated used in the planar case experiment. The SEA coil is changed to a flexible one to wrap around the cylindrical shaped phantom. All other parts remain the same as the planar case experiments.

Figure 5.7 Acquired Images of Excitation Field for Planar Formed SEA Array with Different Phase Offset across Nearest Neighbors. Figure is in next page. The phase offset was set to be (a) 0°, (b) 180°, (c) 320° and (d) 40°. Images were acquired using standard spin echo pulse sequence with TR 500mS, TE 30mS. The thicknesses of the excitation, measured by 50% of the magnitude from peak intensity, are approximately 1.5mm (c) and 8.5mm (d). While in simulations, the numbers are 1.0mm and 7.5mm. The difference is contributed mainly from imperfections of the control of the phase and amplitude in the transmitter. Note that although it was acquired fully encoded, the transmit pattern is achieved in a single shot.

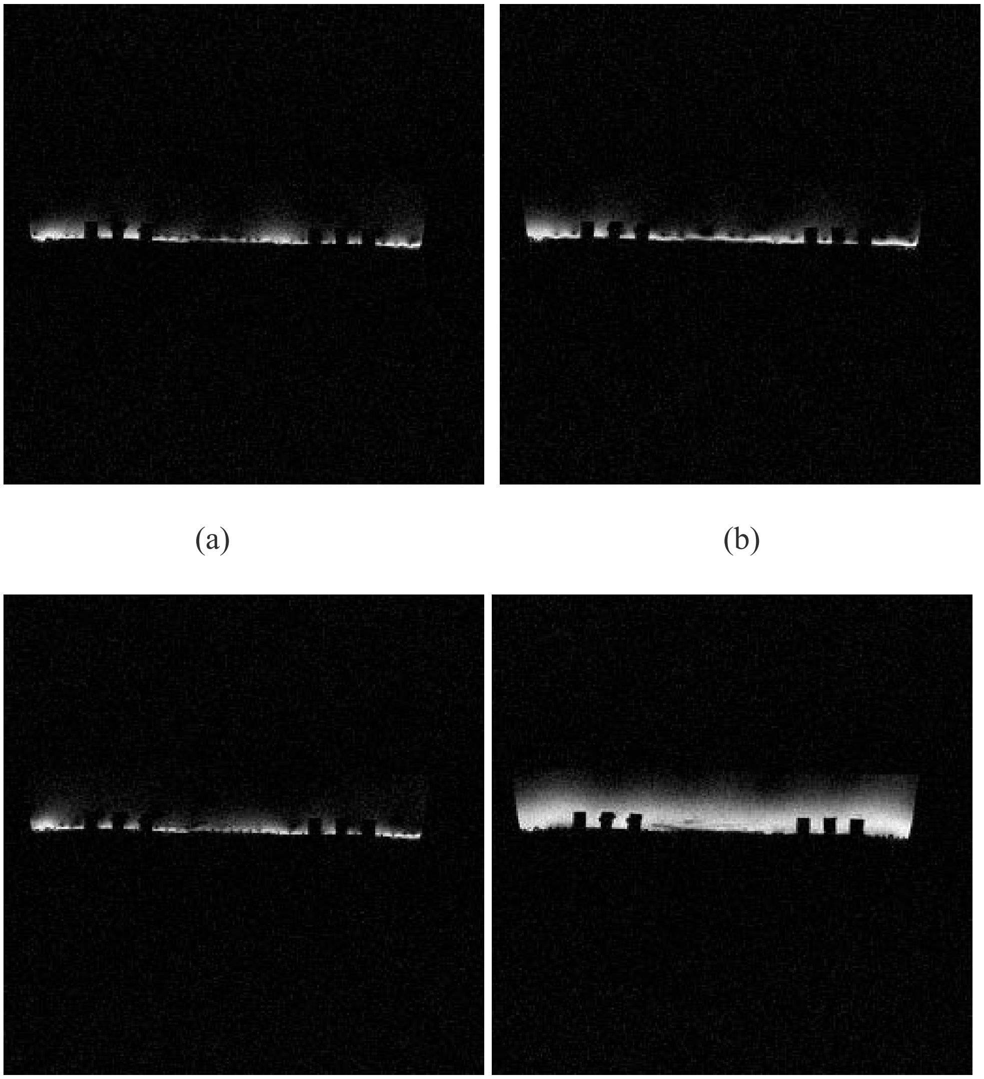

(a)

(b)

(c)

(d)

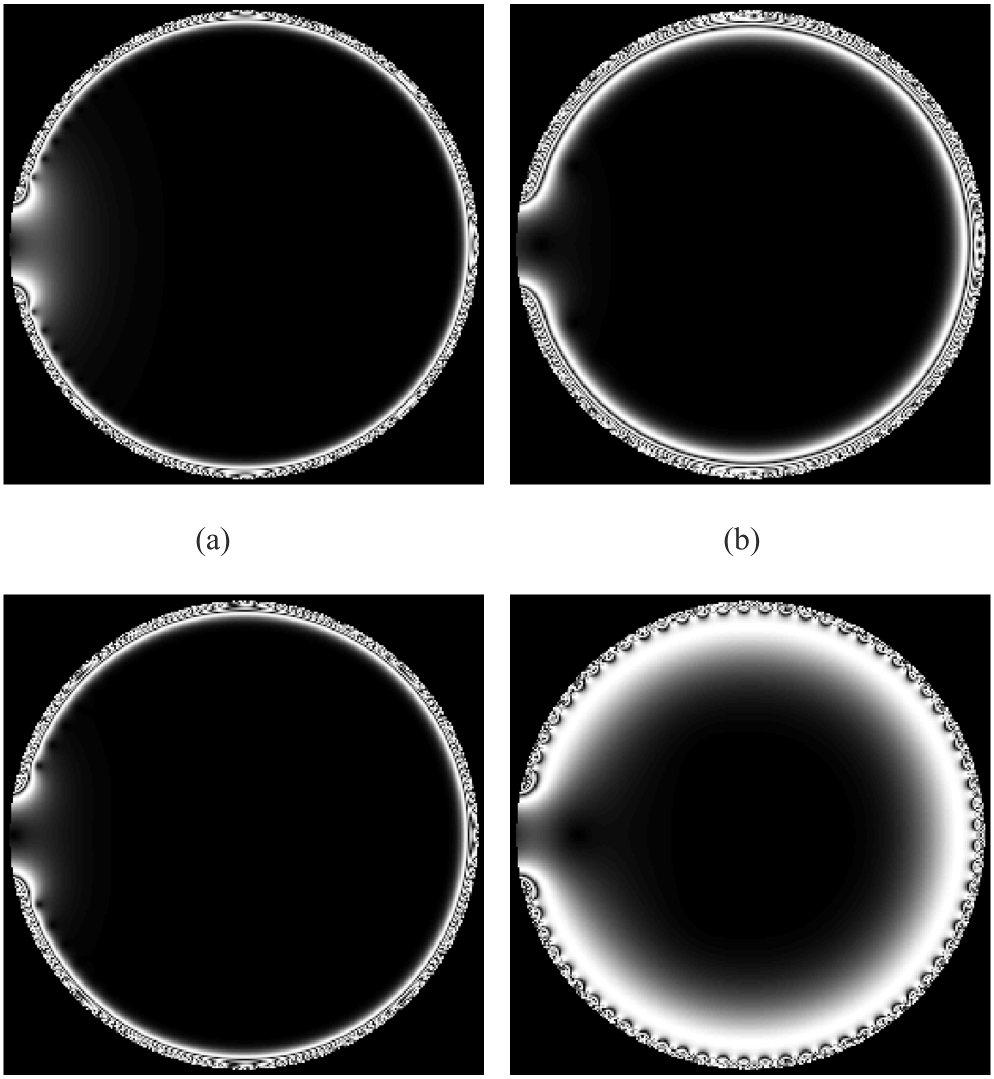

(a) (b)

(c) (d)

Figure 5.8 Simulated Images for Cylindrical SEA Array, with Different Phase Offset across Nearest Neighbors. The phase offset was set to be (a) 0°, (b) 180°, (c) 320° and (d) 40°.

Imaging results are shown in Figure 5.10, indicating optimal phase offset for penetration depth to be around 40°, just as simulation suggested.

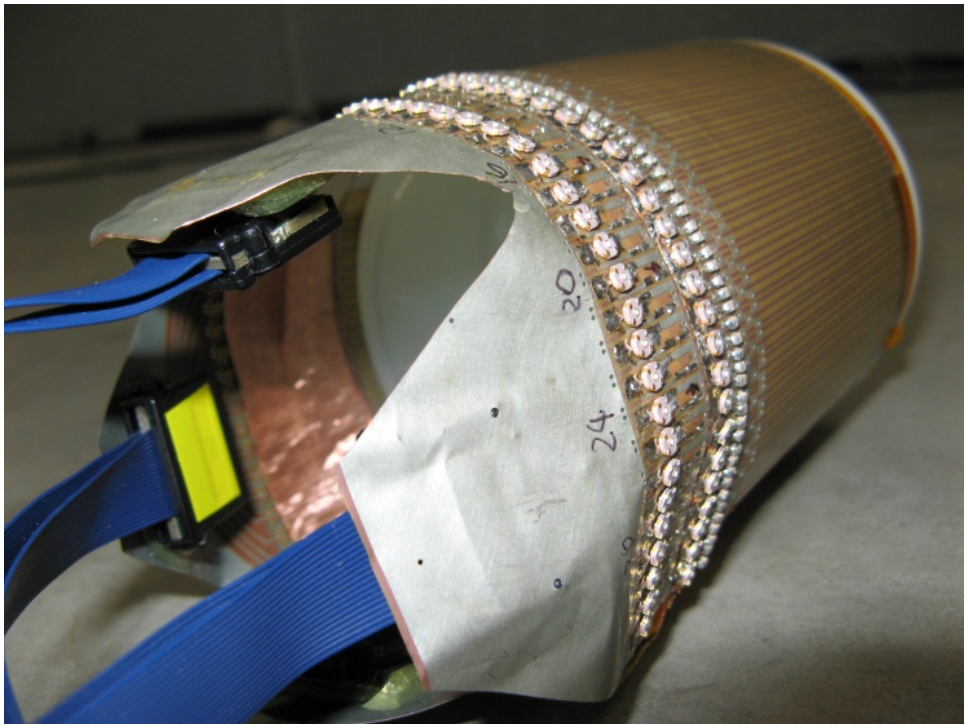

Figure 5.9 Flexible SEA Array Wrapped around a Cylindrical Uniform Phantom. Please note that there is a gap so the phantom is not covered completely. The coverage is only about 350°. This setup is used alone for TR SEA imaging. For images of transmit only, or reverse SEA, the setup is placed inside a birdcage coil for receiving. The ground plate is constantly a problem for reverse SEA imaging using this setup because of eddy currents on the large ground plane. The solution is to place it half way into the birdcage coil, so that the birdcage coil can be properly tuned and matched.

Figure 5.10 Acquired Images for Cylindrical SEA Array with Different Phase Offset across Nearest Neighbors. Figure is shown in the next page. The phase offset was set to be (a) 0°, (b) 180°, (c) 320° and (d) 40°. Images were acquired using standard spin echo pulse sequence with TR 500mS, TE 30mS and FOV 140mm × 140mm. Because the 64-channel flexible array is actually two 32-channel flexible board, imperfections of the connection point makes the right side nulls in (d). The thicknesses of the excitation, defined again by 50% drop from peak intensity in images, are 1.5mm and 12mm for simulations, and 1.5mm and 13mm for images. The transmit pattern is again achieved using a single shot.

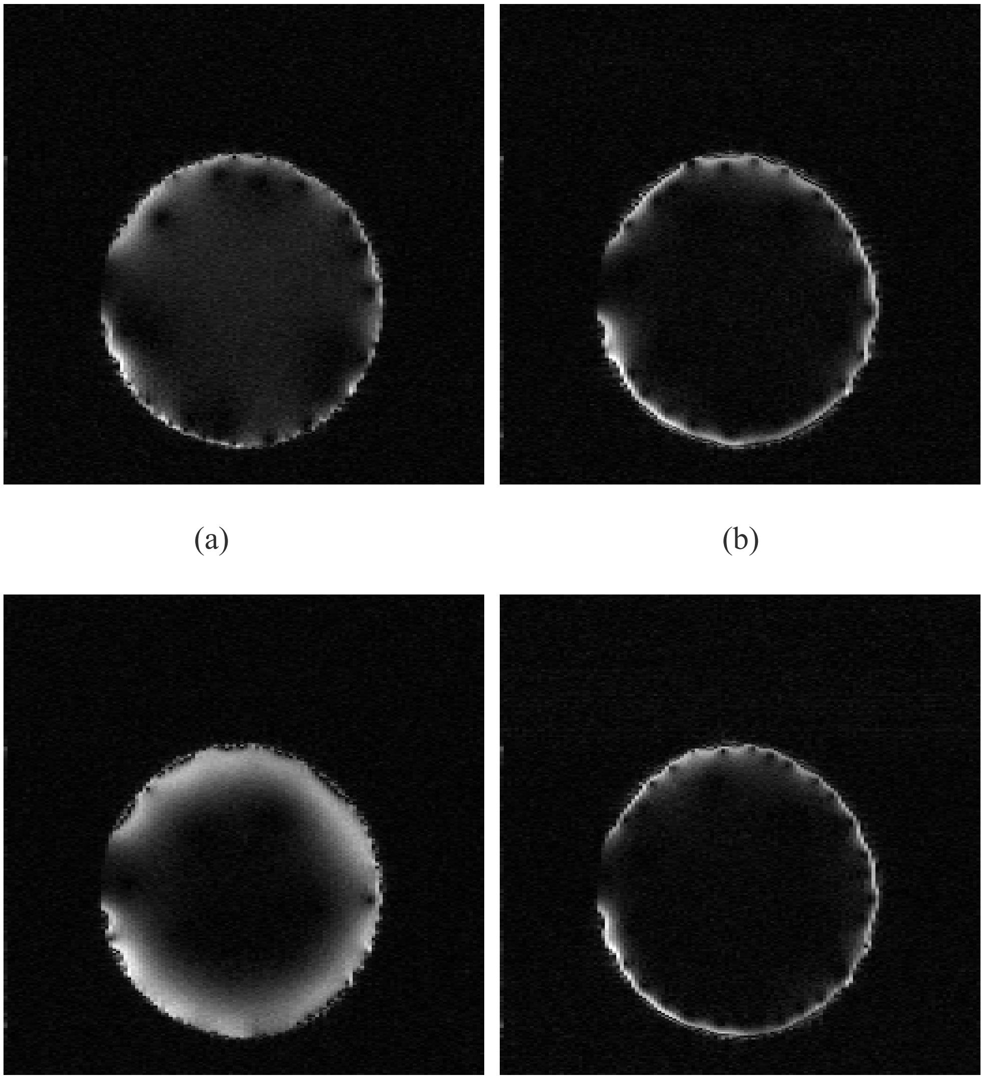

(a) (b)

(c) (d)

V.7 Transmit Filed Synthesis for Single Point

The synthesis of null and maximum for a single point is demonstrated here using three channels of the planar array. Although relatively trivial, this demonstrates the principles of target B_1^+ with large arrays discussed in the next section. Synthesized nulls are actually the sum of three none-zero vectors, requiring precise control of the transmit field. For this reason, the images acquired using simulated B_1^+ patterns to generate nulls were not accurate enough because of practical issues, such as couplings and non-uniform current distributions on the arrays, which were not considered. Actual images were needed to generate the target excitation patterns.

This experimental setup is the same as discussed in the Section V.5. In this experiment, three channels were turned on one channel at a time for images using small tip angles. The images, shown in Figure 5.11, were used as the B_1^+ patterns directly using small tip angle approximation. It is then possible to select phases for the three elements, while keeping the power level constant, to create nulls or maxima in specified locations. This is illustrated in Figure 5.12, where a and b show the effectiveness of three elements to form a null (a) and a peak (b) at the chosen location above the array (indicated by the tip of the arrow). Figure 5.12 (c) and (d) show the calculated patterns, given the same applied amplitude and phase corrections determined from the B1 maps in Figure 5.11. The absolute peak occurs at different point because the optimization was performed for the target point only. Because of the rapid sensitivity fall-off nature of the planar pair array, the vector sum of the three arrays can easily become larger than the target point which is more far away from the array.

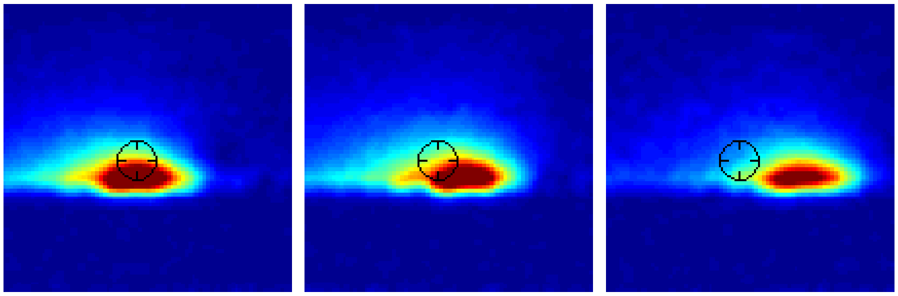

Top (Magnitude images, coils 1, 2 and 3)

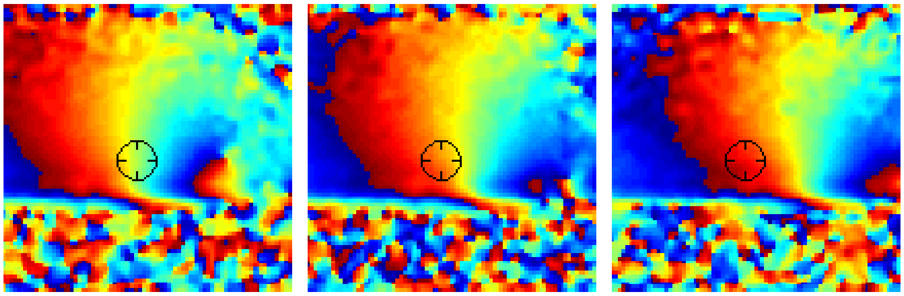

Bottom (phase images, coils 1, 2 and 3)

Figure 5.11 Transmit Field of Three Channels in a Planar Pair Array. Transmit images obtained from each coil, using small tip angles are used to approximate these transmit B1 maps. Tip angle at the point of interest is small, but it is not true at closer to the array. Images were acquired using gradient echo. A Gaussian low pass filter was applied because the field patterns are expected to contain only low spatial frequency information, at least at the point of interest. The target point, shown as crosshairs in the pictures, is where the maximum and minimum is going to be synthesized.

Figure 5.12 Transmit Field Synthesis at a Single Point. Figure is shown in the next page. Using the B1 map shown in Figure 5.11, it is possible to generate a minimized (a and c) or maximized (b and d) intensity by varying the phases of the three channels. The point chosen here is approximately 3mm above the center of coil 1. The first row shows actual acquired images and the second row shows simulated images from the B1 maps. To create a maximum excitation above coil 1, it just happens that there are cancellations between coil 2 and coil 3 (right of image) since the calculation does not care about the values other than the point used for the calculation. That null between coil 2 and coil 3 looks different between the simulation and the actual imaging result because images were used to approximate B1 map. At this region, the tip angles become large and this small tip angle approximation is no longer valid.

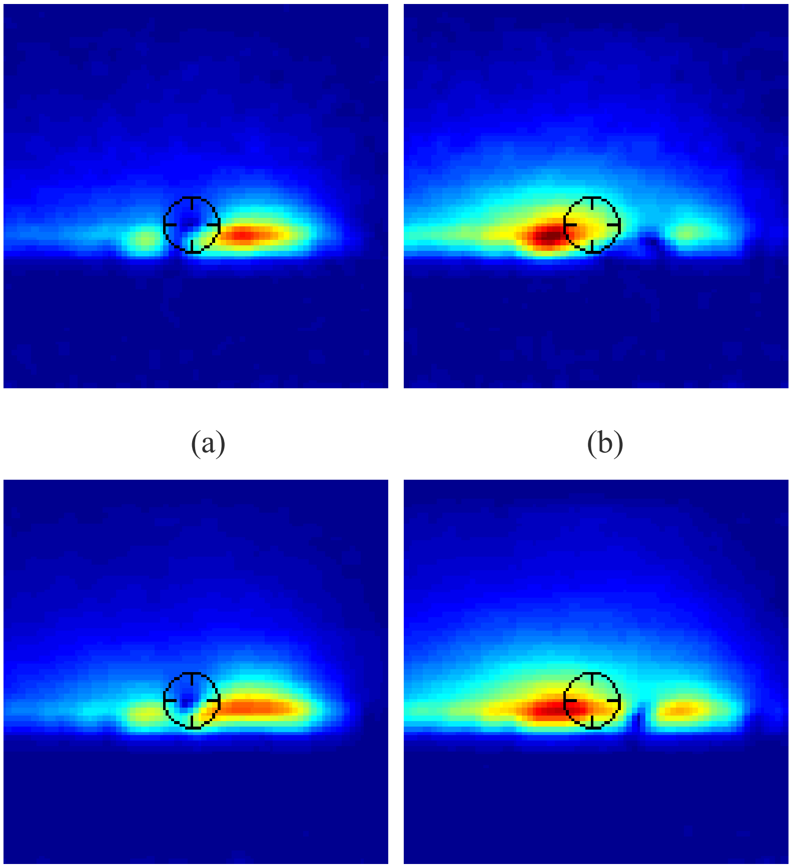

(a) (b)

(c) (d)

V.8 Spin Tagging Using Target Field Method

Beyond the described single point field synthesis, more interesting is the control of the B_1^+ pattern of the array at many points. Here, we attempted to perform spin tagging using the array instead of complicated pulse sequences such as a DANTE sequence. Several approaches were tried. As expected, simply turning off alternating elements did not result in effective tagging. The next approach was to attempt to synthesize nulls using the magnitude and phase control of the modulators.

The experimental setup is again the same as that of the three channel setup. 64 individual images with the resolution of 512x512were first acquired as the B1 map. Along a line 2mm away from the array, a target is specified, which is a square function repeating every forth coil. The width of the nulls was specified to be the same as the coil center to center distance. 512 target points were defined in this way, which produce 15 nulls. Mathematically speaking, there are a total of 64 complex unknown variables specifying the magnitude and phase of excitation for each channel. These variables are denoted by V which is a 1 by 64 matrix. The $B_1{}^+$ patterns at the target locations for all channels form a 64 by 512 matrix, S. At the 512 target points a target $B_1{}^+$ pattern is specified, which is a 1x512 matrix, T. The equation to solve becomes V S = T, which is a simple overdetermined system of linear equations with a closed-form solution. However, the solution of V multiplied by S does not give a good match to the specified target, T. By looking at the problem more closely, it is interesting to note that the problem is over specified. The target contains not only magnitude, which was specified as a square function, but also phase, which was accidently specified as constant zeros across all target points. Reality is that magnitude of the target is of more interest than the phase of the target. With this in mind, the matrix equation, V S = T, was over specified. The problem we try to solve is really |V S| = |T|. By releasing the stringent requirement for the phase of the target, it is expected to have a solution that has less square error in the target. Because of the use of the absolute signs used here, the least squares problems is no longer a simple ordinary (linear) least squares problem, but a non-linear least squares without closed-form solution. It must be solved iteratively. MATLAB is used to find the least square solution. A function was defined, which calculates the sum of squares of errors to the target B_1^+ using given magnitude and phases. The function is minimized by adjusting the magnitude and phase of each channel automatically using MATLAB's built-in *fminserach* function to find the least square solution. The target, together with the linear solution and non-linear solution discussed above are plotted in Figure 5.13. The least square solution is used and the axial and coronal images are shown in Figure 5.14.

In general, the method of using acquired field maps to generate target patterns works well in the axial slice. The left side of the image shows an anomaly, which is caused by two failed channels which caused mistakes in measuring the field maps. The right image, Figure 5.15 (b), shows the coronal image directly over the array. The tags are less well defined in this view. This is believed to be due to variations in the patterns along the long axis of the elements. This has been seen previously in SEA array coils. The scalar magnitude and phase corrections used to create the tags do not take this into account.

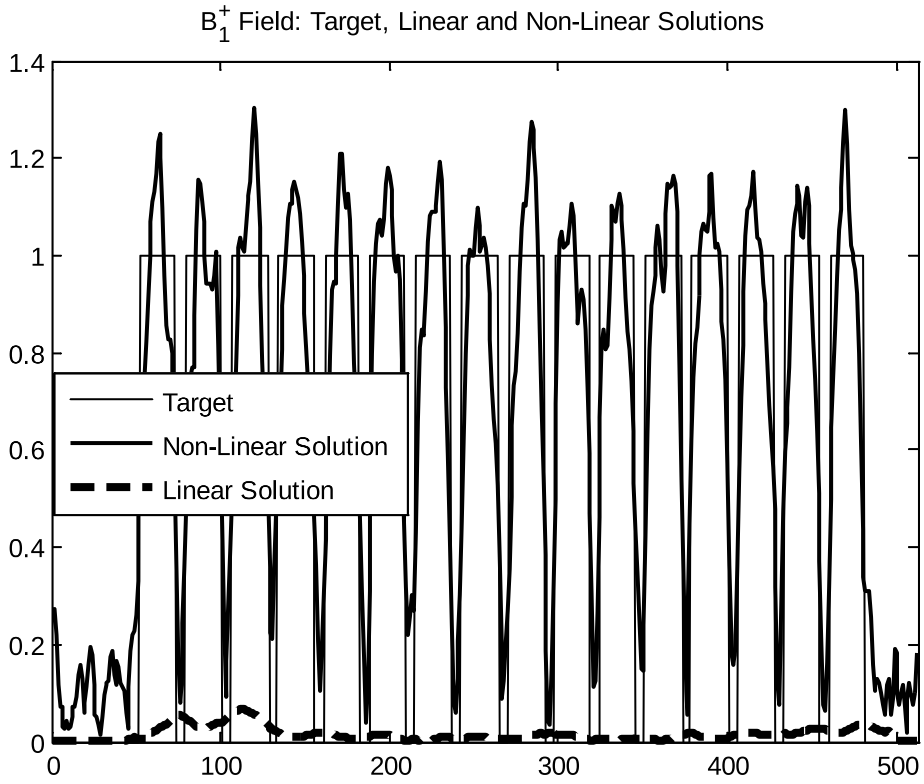

Figure 5.13 Target Transmit B1 Field Synthesis Using Linear Matrix Solution and Non-Linear Optimization Based Iterative Solution. The linear matrix solution (dashed line) is very badly behaved. However, by freeing the phases, the optimization based iterative method gives reasonable result. The corresponding magnitude and phase settings for each channel are shown in Figure 5.14.

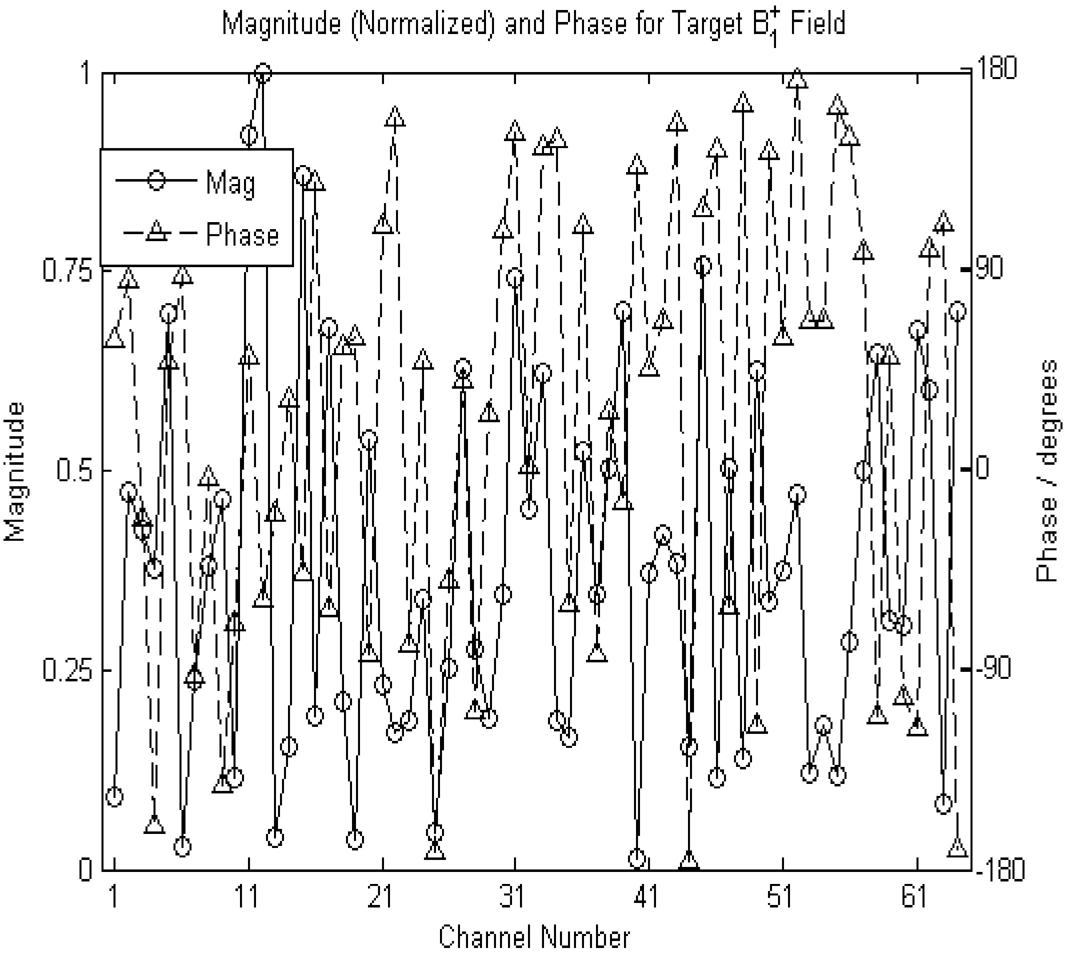

Figure 5.14 Magnitude and Phase Settings to Create the Target B1+ Field Using Optimization Method. The target is 15 nulls, with center to center distance equal to 4 times of the center to center distance of two adjacent coils. Though appearing almost random, this setting was used to successfully create the transmit pattern shown in Figure 5.15.

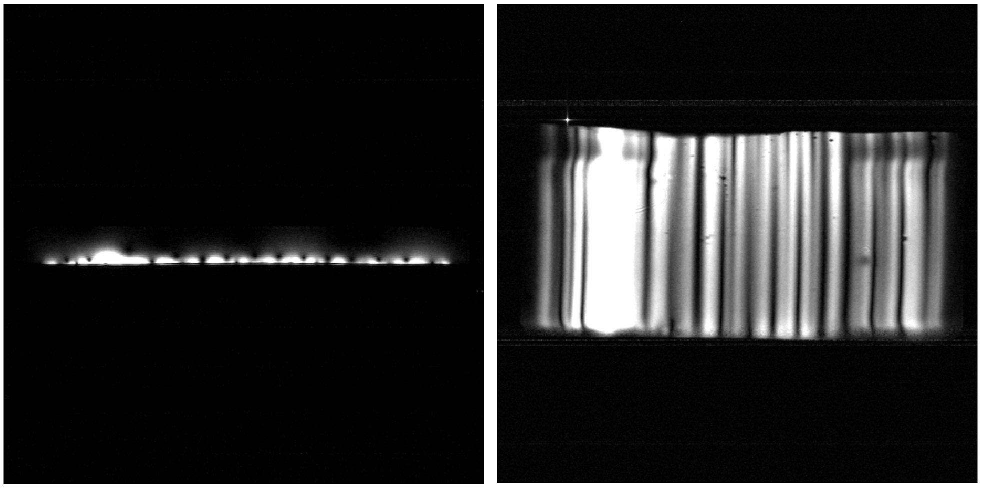

Figure 5.15 Target Transmit B1 Field Synthesis. After obtaining a B1 map from each channel, it is possible to synthesize desired target transmit patterns at given regions. This experiment is almost identical to the three channel experiment above, except 64 channels are used, and the target is a row instead of a single point. First, an axial image which is perpendicular to the long axis of the array is used to obtain the transmit B1 maps. A target is given, which is a square function with 15 evenly spaced nulls, each of which has a width equal to one coil to coil distance. The target has 512 points and three are only 64 channels so it becomes an over determined equation to solve. A least sum of squares solution is found, which gives the magnitude and phase of the 64 channel array. Using this solution, an axial image is acquired which is shown in (a). A coronal image is then acquired, which is shown in (b). In the coronal image, the patterns look different from different vertical locations because of current distributions on the coil are different from coil to coil. The bright region in the left is because of two failed channels of the transmit system.

V.9 Alternative Spin Tagging Method

An alternative approach for spin tagging synthesis using the array is achieved together with a volume coil. The RF source from the MR scanner is split two way, one to feed the 64 channel system and one to feed the system amplifier through an adjustable attenuator. The system amplifier is connected to the system TR switch and then to the volume coil. This way, the uniform field from the volume coil is combined with the planar pair array which is placed inside the volume coil. The setup is illustrated in Figure 5.16.

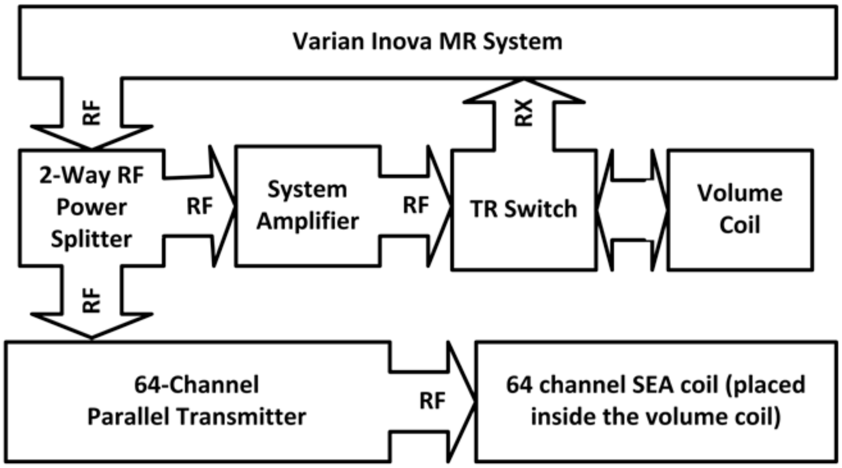

Figure 5.16 Experimental Setup of Spin Tagging Using Planar Pair Array and Volume Coil for Transmit. The 64 channel planar pair array is placed inside a volume coil to transmit simultaneously with the volume coil. The actual transmit field is the vector sum of the transmit fields from volume coil and planar pair array.

A constant magnitude with a phase is used on the planar array. This setup is essentially a 65 channel system. As it is possible to match the amplitudes at different heights and create an essentially arbitrary phase ramp (though no greater than 180 degrees per coil width), these fields can create nulls (tags) at variable spatial frequency. Figure 5.17 illustrates the principles.

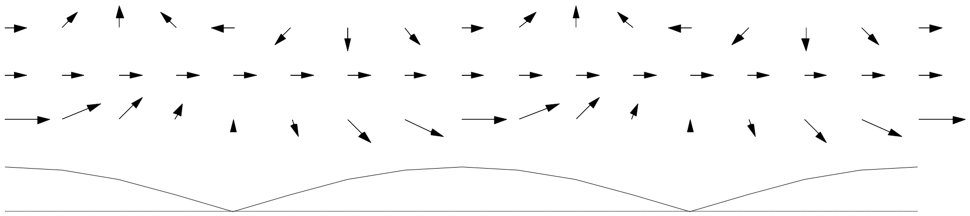

Figure 5.17 Principles of Spin-Tagging Generation Using Planar Pair Array and Volume Coil for Transmit. The first row of arrows show the transmit pattern generated by the planar pair array, which are constant in magnitude but with a phase ramp. The second row of arrows show the transmit pattern generated by the uniform volume coil, which are constant in both magnitude and phase. The sums of the two fields are shown in the third row. Magnitude of the arrows in the third row is plotted below, with dotted line as reference for zero level. The two nulls are the spin tagging that we are trying to create.

Figure 5.18 (a) and (b) show a set of tags created with a low spatial frequency using phase ramp of 300°, calibrated for a relatively high slice. The axial and coronal images are shown, demonstrating very well-defined tags. Figure 5.18 (c) and (d) show the nulls calibrated for higher spatial frequency using phase ramp of 180° and a closer location to the array, again showing very well-defined tags at a spacing of every two coils. Importantly, this approach should allow spin tags to be created very rapidly at greater depths than the method investigated above, because it does not rely on cancellation of signals from the different array elements and is thus less prone to errors.

V.10 Simulation Conclusion and Discussion

Using simple phase shifts and flexible array, surface excitation is achieved. This excitation pattern can be predicted using simple Biot-Savart law. While this work uses SEA array, we expect that transmit patterns can be predicted using this program, when coil size is much smaller than the wavelength. Beyond predicting the transmit patterns, it is possible to use this combinations for applications like RF encoding.

It is interesting to note that there is an optimal phase offset, which brings the most uniform field pattern and penetration depth. And the result might seem counter intuitive. It is normally neither 0° nor 180° across-neighbor phase shift brings the optimal penetration depot, as one might perceive quickly, but rather one that is determined by the geometry of the array. In the case of planar SEA array with the geometry defined in Figure 5.3 and Table 5.1, the optimal phase offset is around 320°.

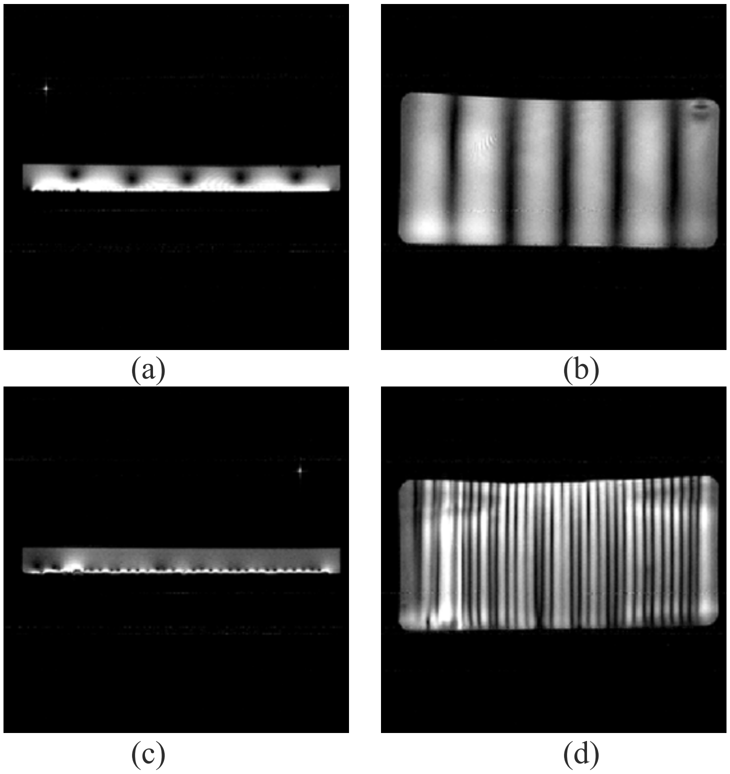

Figure 5.18 Experiment Results of Spin Tagging Using Planar Pair Array and Volume Coil. Using the configuration shown in Fig 9, the actual transmit pattern is the vector sum of that from the volume coil, which is a constant, and that of the array, which is a constant in magnitude but a ramp in phase. The vector sum becomes a cosine modulated spatial function. This can be used as a way to create tags alternative to the complicated target B1 method used earlier. (a) and (c) show the axial images, while (b) and (d) show the corresponding coronal images that are acquired using the setup shown in Figure 5.16. (a) and (b) use phase ramp of 330°, creating a null for every 12 channels. (c) and (d) use phase ramp of 180°, creating a null for every 2 channels.

With the coil constructed in the software, the simulation takes about 1 hour 40 minutes for 72 frames of results for a 64-channel SEA coil array, in the resolution of 200 by 700 problem space on a laptop with Intel Corel 2 Duo 1.4GHz processor with 4GB of memory. While the speed can be improved dramatically if the true 3D code is converted to consider only currents in xz plane, we keep the code as universal as possible for future uses. Graphic card accelerations can be used easily with MATLAB version 2010a or later but the hardware is not available on the computer used for the simulation.

It is not quantitatively measured or plotted, but the penetration depth and filed uniformity have been shown to be a function of the phase offset across neighboring channels. This function does not have a sharp peak, as observed from the simulation and imaging results. As the result, we only looked at the results and determined the “optimal” phase offset. This optimal point can be more precisely determined, but we consider it not necessary in our case.

CHAPTER VI

SYSTEM VERIFICATION, TESTING AND CALIBRATION

A lot of effort in this work was put to testing, calibration and verification. As the channel count goes up, testing and debugging can become really tedious tasks. An automated testing system is becoming a necessity, if not a must. This section describes an automated testing system built using National Instruments DAQ card and the MATLAB interfaces. This program also assists with system calibration. Some testing results are also provided.

VI.1 Time and Frequency Domain System Response in DC Modulation

The most basic demonstration is done using an oscilloscope. It is probably the most straightforward test and demonstration. Many of the demonstrations here are done qualitatively, but they can be done quantitatively if desired. However, we choose to make many of the quantitative measurements using a VNA instead of oscilloscope because they are easier and often more precise for RF. Those testing and measurements will be covered in the next sections. The only problem with VNA is that it is usually slow compared to oscilloscope, not suitable for many of tests involving short pulses.

The purpose is to test a single channel for amplitude, phase and attenuation control to verify that single channel control works. The Varian Inova system generates sinc pulses, 10MHz reference signal and a TTL trigger source. The RF is split into two branches, one to oscilloscope directly, and the other into vector modulator box followed by the amplifiers, TR switch, a single channel of coil and pick up loop to oscilloscope. Just before getting to oscilloscope, there is a mixer on each branch to mix the 200.23MHz signal to 1.05MHz and a low pass filter to filter the higher frequency mixing product. The mixing circuit is necessary because of the bandwidth limitations of the oscilloscope.

Amplitude, phase and attenuation are adjusted on screen using the GUI. We examined on the oscilloscope screen, and recorded for analysis in MATLAB. A screenshot showing both the oscilloscope software and the GUI of the controller are shown. By adjusting the power and phase value on the software GUI, one is expected to see the result on the scope. In other words, we are showing here the whole system's response to user input. Figure 6.1 shows the result with different amplitude settings on the software GUI.

Figure 6.1, intuitive though, is of qualitative merit rather than quantitative. To quantify the result for accurate measurement of the modulation errors or distortions, the signal is imported into MATLAB to demodulate numerically to analyze the accuracy of the system's response to specified input, which is shown in Figure 6.2.

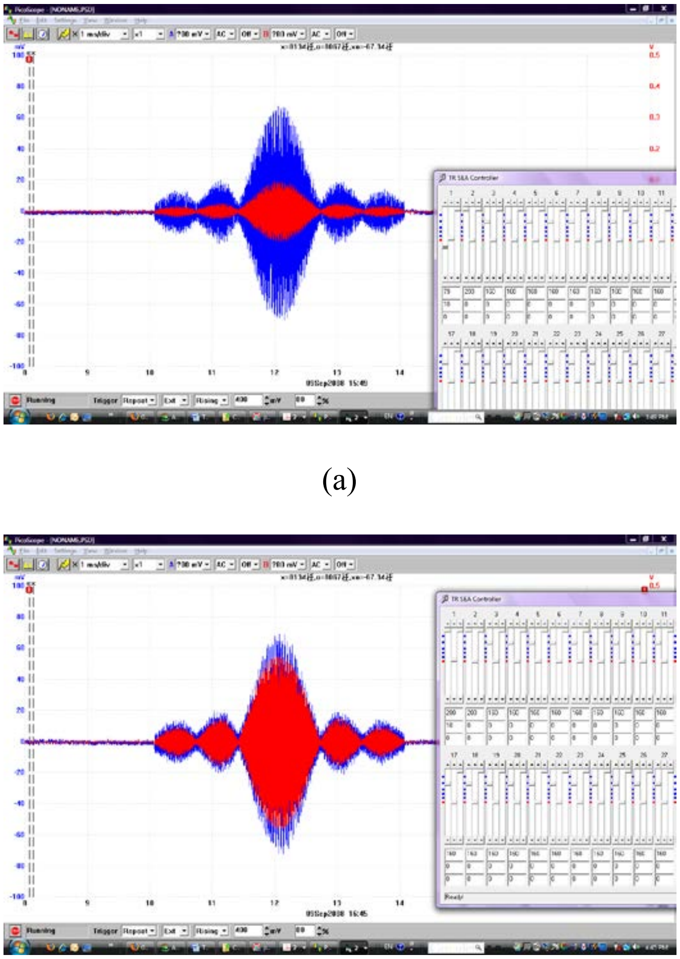

(a)

(b)

Figure 6.1 System Response from a Single Channel in Static Control Configuration. In both figures above, blue traces are from system pulse, or input of vector modulator. Red traces are output from modulator. The GUI is on the right side of the screen. As can be seen, the amplitude settings are different from the two cases, so the output levels are changed accordingly as expected.

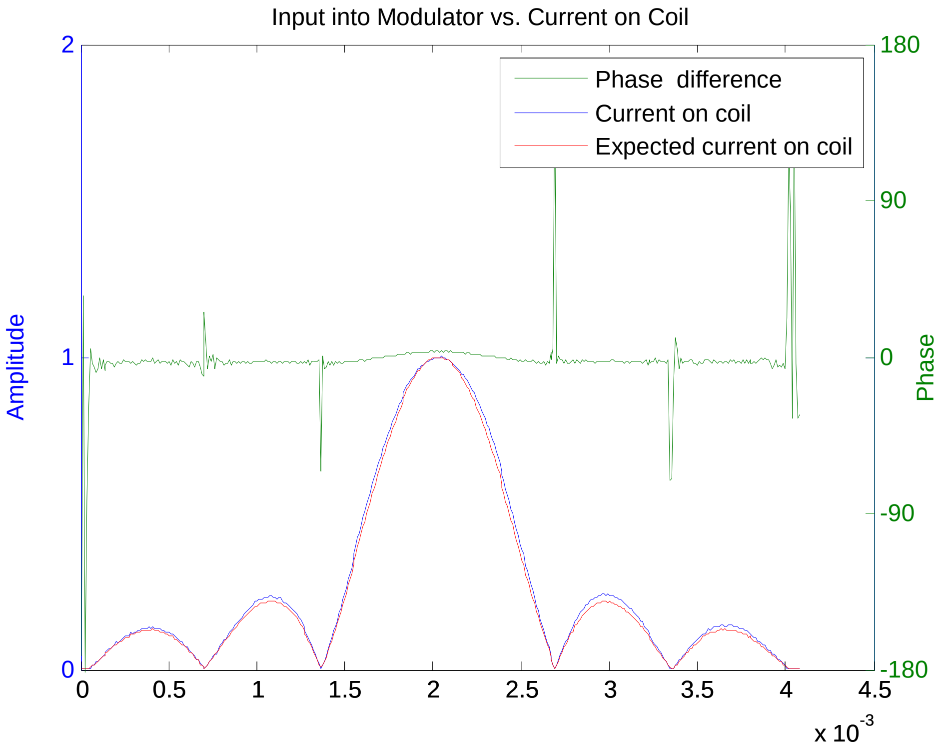

Figure 6.2 System Time Domain Response of a Single Channel Using Static Modulation Scheme – Software Demodulated. The small bumps on the phase curve when amplitude is changed near zero are normal, as the phase of zero amplitude is of no physical meaning. Phase error here is not significant. The rest of the area gives amplitude error and phase errors of less than 1%

Since the data is sometimes more interesting in frequency domain, such as in the case of slice selection when it indicates the accuracy of slice selection, it is shown in Figure 6.3 for the frequency composition. The same dataset is used.

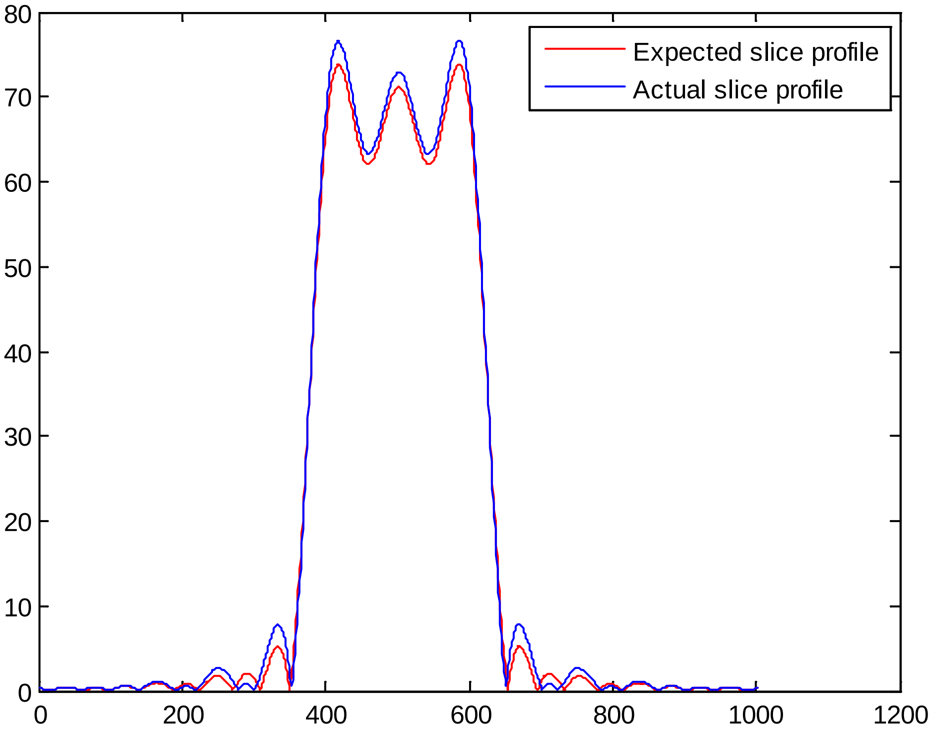

Figure 6.3 System Frequency Domain Response of a Single Channel Using Static Modulation Scheme. The temporal data from Figure 6.2 is analyzed using FFT to investigate the system's frequency response and ability to do slice selection. A mean square error of less than 2% is measured using this plot.

VI.2 System Response to GUI Input Sweep

The software GUI provides three sliders with corresponding text boxes which are associated with the three parameters for each channel. This test is used to verify two of the three parameters, amplitude and phase. The attenuators response is a more straightforward one and it shows to be working the same way as indicated in the datasheet. Different values of amplitude and phase settings are set in the GUI. The actual output is measured using a VNA, and the results are plotted in Figure 6.4.

VI.3 Vector Modulator LO Leakage Hardware Calibration

The first step is a relatively rough calibration of the vector modulator for minimum LO leakage. Section III.4 of this dissertation already describes the hardware design which is used for minimal LO leakage. This section will cover the detailed procedure for this calibration.

The purpose here is to minimize the output power level, when the magnitude settings are set to zero. With this in mind, the rest is straight forward. All needed is connect the system to a network analyzer set to S21 measurements, and set the magnetite on the GUI to zero for the channel under test. The port 1 of network analyzer should be connected to the input of the vector modulator, and channel 2 to the output. By adjusting the variable potentiometers, S21 value is minimized, usually to under -40dB with on board preamplifiers and 0dB settings for the digital controlled attenuators. While this hardware calibration scheme works well in a short period of time, signs of fluctuations in the S21 parameters are shown in a long term. This is normally not a problem, but might be for LO leakage sensitive pulse sequences, such as transmit EPI.

Figure 6.4 Bench Test Results – Actual Amplitude and Phase Output vs. GUI Input Settings. Figure is shown in next page. Data from the bench measurements shows the amplitude variation when phase is swept, and phase variation when amplitude is swept. Ideally, all data points would fall on a single plane in both plots. The data shows an amplitude variation of less than one dB and phase error of less than 5°.

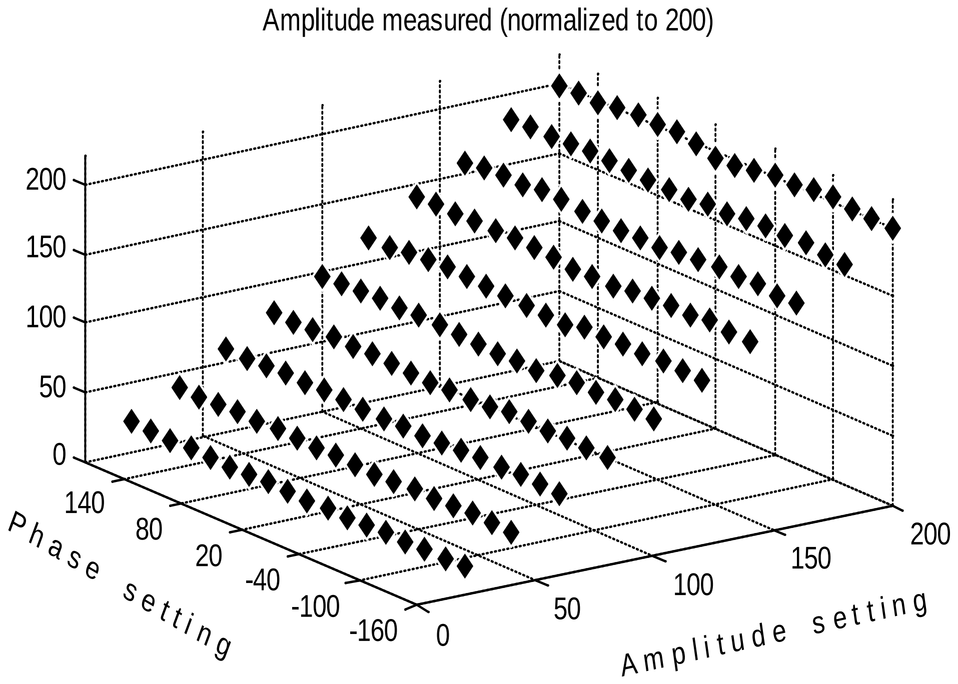
Amplitude measured (normalized to 200)

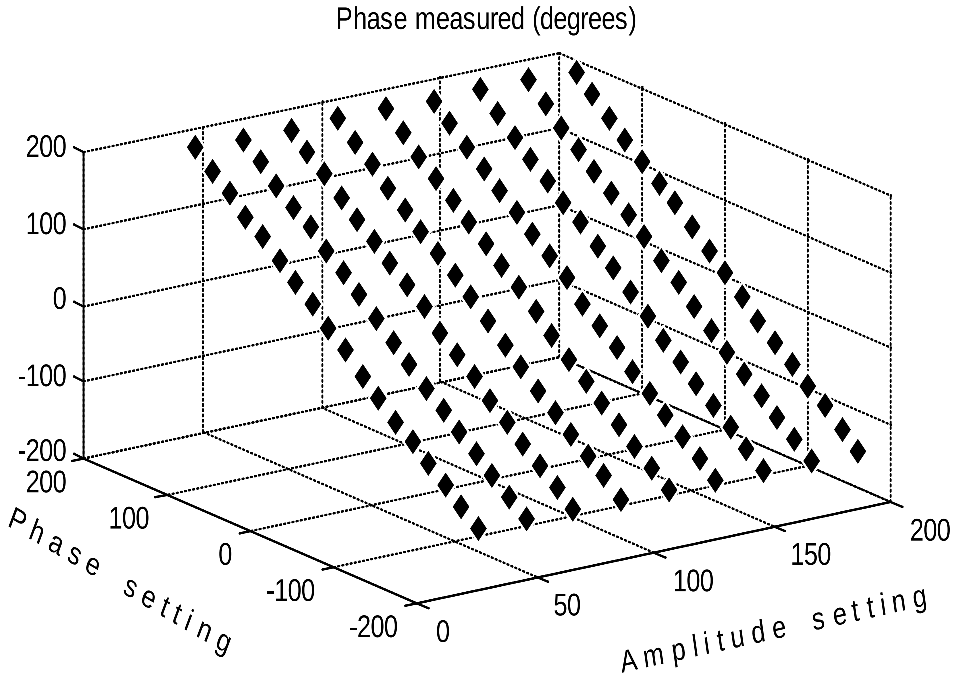
Phase measured (degrees)

VI.4 Software Calibration for TR SEA

Software calibration is provided to compensate not only LO leakage, but also I/Q balance and extra phase shift. Because of imperfections inside the vector modulator IC we use, I/Q are not well balanced. For example, given I =2.5V and Q=3V vs. I=3V and Q=2.5V yield not only a difference of 90° phase shift, but also amplitude variations. This requires an I/Q balance calibration. Because of different cable lengths, each channel has a different phase shift. Users usually care about the actual phase at the coil, which should correspond to the reading on the screen. Thus an offset is needed for each channel.

Furthermore, while hardware calibration to eliminate LO leakage is sufficient for most cases some pulse sequences may be very sensitive to LO leakage. An example is transmit EPI. As the gradient moves through k-space trajectory, most of the part would be very low power level, except for the DC part. LO leakage, though low in power level, can be on the same order as the higher frequency part of the transmitted pattern and accumulate through the pulse sequence. This might bring noticeable result in the final images. Because the software calibration requires reconnecting the vector modulators to network analyzer, a calibration using MR images can be done.

All of the three calibrations for TR SEA setup can be done pretty easily because the software GUI provides a guideline. Simply click the "Calibrate" button and an interface will show up, as shown in Figure 6.5. The frame labeled as “zero point adjustment” is designed for LO leakage. By clicking the four buttons, one can search the minimum point for LO leakage. Note that it is labeled as “real” and “imag” instead of I and Q, but they are really the same. The frame labeled as “normalization” provides I/Q balance functions. By clicking the “real” buttons, imaginary part is set to zero, and vice versa for the “imag” buttons. One should look at the network analyzer, until clicking the real buttons gives the same as the “imag” buttons. Detailed steps for the calibration are in following text.

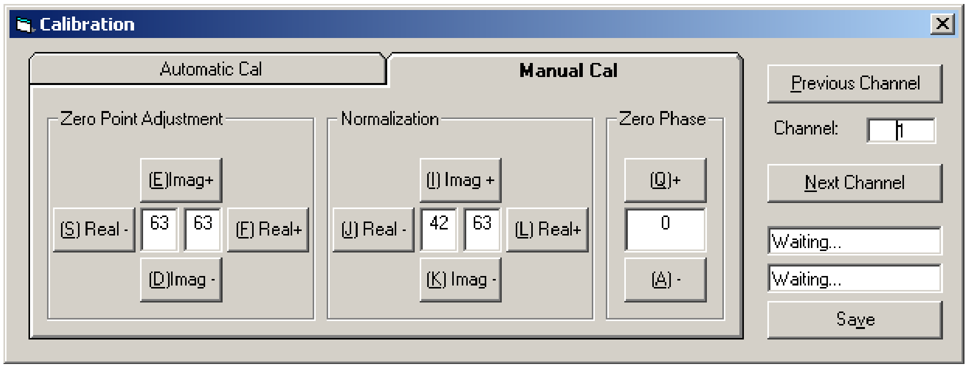

Channel: 1

Waiting...

Waiting...

Figure 6.5 Calibration Interface Built in TR SEA Controller Software. This interface is brought by clicking on the “Calibrate” button on the main interface. User use a network analyzer configured in S21 measurement together with this interface for calibrations.

In this “Manual Cal” tab, right side provides selection for the channel for calibration. Left side has the Zero Point Adjustment, Normalization and Zero Phase frames. The usual procedure as follows:

1. Calibrate network analyzer for S21 measurement. Connect port 1 to input of system, and port 2 to the output the system, in the channel for calibration. A appropriate attenuator is needed at the output to protect the network analyzer if amplifier is used.
2. Click the Previous Channel, or Next Channel button to the channel under test, or simply type it in the text box labeled as Channel.
3. Do zero point adjustment by clicking one of the four buttons in the Zero Point Adjustment frame until the network analyzer reads the smallest value.
4. Do Normalization. Click the Real+ or the Real- button in the Normalization frame to set the real part normalization. Read the absolute S21 value on the network analyzer. Remember the value, and click the Imag+ or the Imag- button for imaginary part normalization. One should get a value the same as when clicked on the real part normalization. Please note that to get the fully dynamic range, it is recommended to do the normalization with the maximum values you can get. For example, when real part equals to 20, and imaginary part equals to 24, would be worse than when the real part equals to 40, and imaginary part equals to 48. These will be multipliers to the actual output to the digital controlled potentiometers.
5. Optional: Do zero phase compensation. This step is normally not required because the testing here is for the low power part only. A system phase response requires the whole system, including RF amplifiers to be tested and calibrated. The system phase calibration will be covered using an automated

system described in Section VI.6 of this dissertation. This part is only necessary when the lower signal part is used without the high power part. That is normally in some special cases, like using the vector modulators for mode synthesizations. In this case, click the + and the - button in the Zero Phase frame until the phase on the network analyzer reads zero. This ensures that when 0 degrees is specifies on the GUI, the output of the system is in phase with the input of the system.

6. Click the Save button.
7. Repeat step 2 through 6 for another channel until all channels are calibrated.
8. Close the software and restart for the new calibration settings to take effect, as prompted.

All the calibration data, as well as some additional information are stored in the settings.ini file. It has the standard INI file structure with comments for manual editing. If some manual adjustment is necessary, one is advised to open the file. It contains settings of the NI DAQ device name and recommended steps for modification as comments. A small section of it is copied below in order to show its structure.

```
[Device]
# This section contains device name setting.
# Run National Instruments Measurement and Automation Explorer (NI MAX)
# To get device name for the USB Block. In MAX, click "My System" -->
```

```
# "Devices and Interfaces" --> "NI-DAQmx Devices", and look for "NI
#     USB-6501". The name listed for that device is the device name. Typically,
#      you should set Name=Dev1 if it is the only DAQ device.
Name=Dev2

[Defaults]
# This section contains default settings when the software is loaded.
Amplitude=160
Phase=0
Attenuation=-20

# Below are settings used for calibration. Settings in [RealZero] and
#     [ImagZero] are used to get zero point, so that when amplitude is set to zero,
#     you get as low transmitted power as possible. [RealFactor] and
#     [ImagFactor] are used to calibrate out the non-linear factor in HPMX-2005
#     vector modulator. A good guess of the values would be imagzero: 65,
#     realzero: 65,  realfactor: 47, imagfactor: 62
# Note: you must retain the following conditions:
#     realzero+realfactor <= 127, imagzero+imagfactor <= 127
#
 [RealZero]
Ch1=63
```

```
Ch2=62
Ch3=65
Ch4=61
Ch5=66
Ch6=58
…
```

The rest of the code is truncated, but it should be relatively easy to interpret. As seen in the code above, meanings of each section are already included as comments to make such interpretations easier.

VI.5 Additional Calibrations

In transmit SENSE mode, another program in MATLAB, vmzero, is written. It provides similar function, but without a GUI interface. A text based interface is provided. It is used to interface the DAQ card's analog output channels instead of the digital controlled potentiometers.

During actual imaging, further calibration can be performed using images. Setting all values to be zeros in the input, there should not be any transmitted field. If any transmitted pattern is seen, LO leakage is there. In this case, one need to carefully adjust the zero points to minimize the LO leakage. Later this offset will be used as an offset for the I and Q channels.

VI.6 Testing Setup for Whole System

The system is tested for each channel. For continence purposes, an automated system is given. The system is also used for additional calibrations to bring an offset of attenuation to each channel to balance all the channels, and an offset of phase settings for each channel to make the reading on the GUI accurate. The program is written in MATLAB, but it is provided for the calibrations of TR SEA system. The settings.ini file will be updated by this program automatically.

The main testing function is S21 measurement, which is done using a Vector Network Analyzer (VNA). The test setup is shown in Figure 6.6. A computer provides the controls to an NI DAQ multifunction card and an Agilent 4395A VNA through IEEE-488 General Purpose Interface Bus (GPIB) interface. More precisely speaking, the interface is Hewlett-Packard Interface Bus (HPIB), a primitive version of GPIB. However, the parts that are used here are exactly the same. Trigger of VNA, blanking of amplifiers and control of TR switches (which is omitted in the drawing) are provided through an NI DAQ device. All the controls are provided by MATLAB with DAQ toolbox.

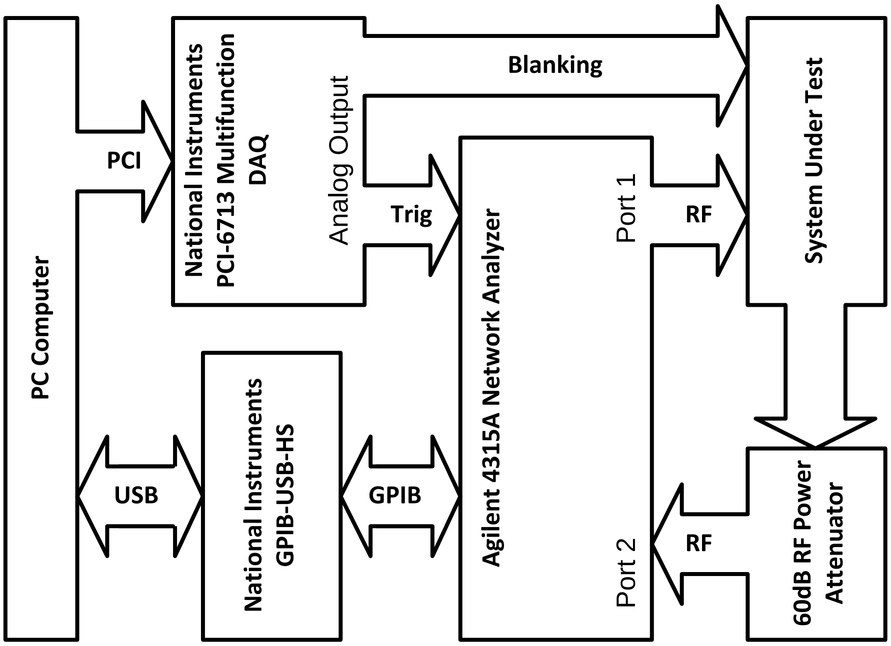

Figure 6.6 Block Diagram of an Automated Testing System. A PC computer is used to guide users through calibrations and control NI DAQ and VNA through GPIB for testing and measurement.

As a preparation for the automated testing system, a MATLAB function, pulse_gen, is written to generate pulses for testing purposes. It generates a 5V square pulse with specified duration using an analog channel of an NI DAQ card. The code was tested using PCI-6713 card, but should work with other DAQ cards. Although it uses a digital channel, it actually generates a pulse that is more like a digital signal. The reason to use an analog channel is mainly because it is easier to program in MATLAB with precise time control. The pulse generated by the pulse_gen function is used for multiple functions, which are triggering network analyzer, de-blanking the amplifiers and turning on gate control of the second stage amplifiers, which can be all identical signal.

Another MATLAB function, tr_sea_cal is the one actually used for the automated testing as well as system calibration. It provides basic guides for user to make connections, programs the VNA for calibration and the desired testing and shows the result of the testing on the screen. A S21 parameter power sweep is used, because it shows the amplifier's compression as well as the system's response to user input. Figure 6.7 shows a test in progress. The blue line shows the gain vs. input power, and green line shows the phase vs. input power. The blue line cuts down at -2dBm input because the blanking signal is provided in such a way that it actually cuts off earlier than the whole sweep. This is just a simple way to show the functionality of the noise blanking circuit in the amplifiers without additional testing procedures.

A typical gain curve of a channel is given in Figure 6.8. This was acquired automatically using the tr_sea_cal script described above.

The 1dB compression point, which is roughly 100W, comes mainly from the second stage amplifier. This was verified by removing the second stage amplifier and look at the output of the first stage amplifier.

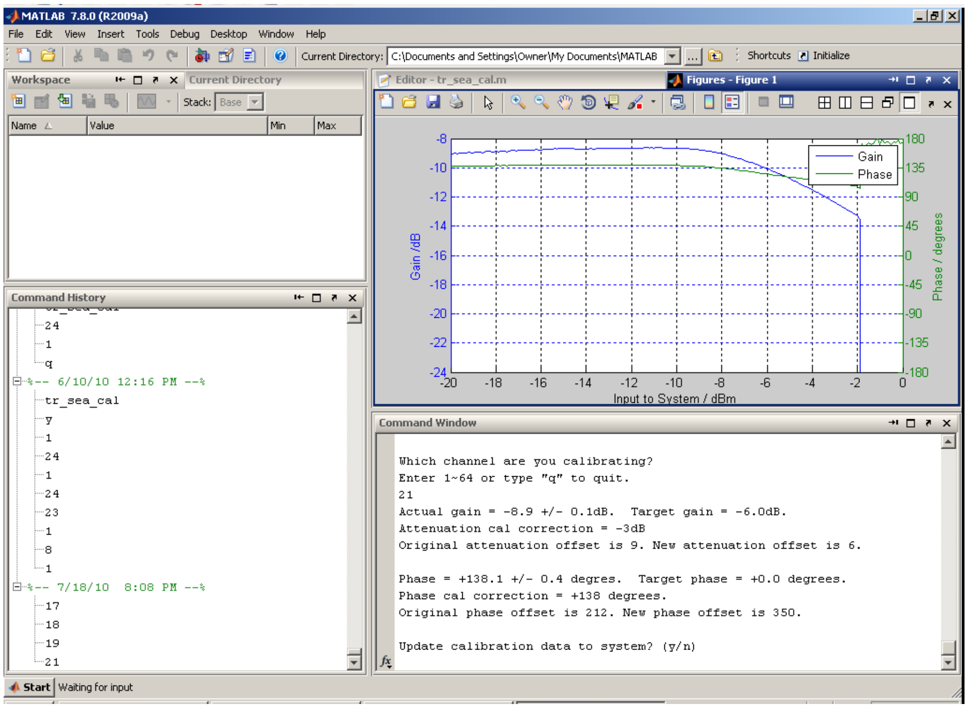

```
  24
  1
  q
%-- 6/10/10 12:16 PM --%
  tr_sea_cal
  y
  1
  24
  1
  24
  23
  1
  8
  1
%-- 7/18/10  8:08 PM --%
  17
  18
  19
  21
```

```
Which channel are you calibrating?
Enter 1~64 or type "q" to quit.
21
Actual gain = -8.9 +/- 0.1dB.  Target gain = -6.0dB.
Attenuation cal correction = -3dB
Original attenuation offset is 9. New attenuation offset is 6.

Phase = +138.1 +/- 0.4 degres.  Target phase = +0.0 degrees.
Phase cal correction = +138 degrees.
Original phase offset is 212. New phase offset is 350.

Update calibration data to system? (y/n)
```

Figure 6.7 System Testing and Calibration Software. The software guides uses through the testing setup as shown in Figure 6.6. It does a power sweep of the system, which is useful for gain readings. In the plot, the green line is for phase and the blue line is for gain in dB. Please note that since the calibration is done without the 60dB attenuators and some extra cables in line which are added later for the plot, the actual gain is higher than what is plotted. One can easily add that part in the software easily if the absolute power readings are essential.

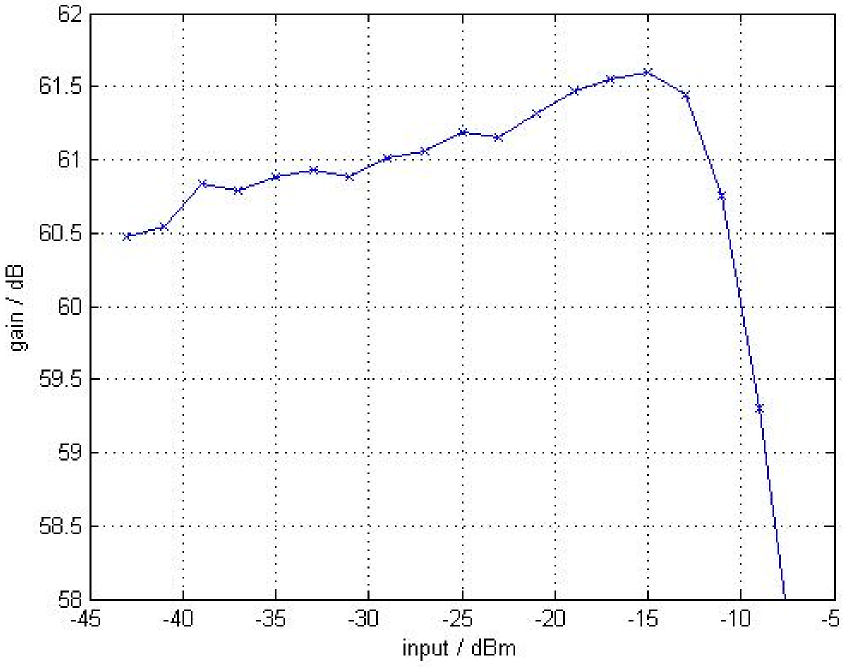

Figure 6.8 Typical Gain Curve of a Single Channel Acquired Using the Automated Testing System. At -13Bm input, the gain is roughly 61.5dB. That corresponds to 70W. The 1dB compression point happens at -10.5dBm input power, with about 60.5dB gain. That corresponds to 100W. This is measured at the end of the whole RF chain, i.e., at the coil. Otherwise the system can provide more power. The non-linearity can be compensated for transmit SENSE if desired.

With the transmitter power curve measured, the recommended input of the system would be -15 ~ -12dBm input, for best dynamic range of the system. The user should be aware that compression will happen when full power is used. An attenuation of at least 3~5 will be usually necessary.

VI.7 Calibration Verification Using Images

After the system is calibrated and verified using the procedures described in this chapter, single channel imaging for each channel was made. Both phase and amplitude images were taken. The images were made using a single channel of the transmitter at a time using a birdcage coil. Normal gradient echo sequence was used. Amplitude and phase images before and after calibration are shown in Figure 6.9.

VI.8 Multi-Slice Experiment with Temporal Phase Ramp

Transmit SENSE requires full modulation. A test of the system's full modulation capability was tested with a multi-slice (in the axial direction) experiment using temporal phase ramps. In this experiment, base band sinc waveforms were produced with an NI high-speed analog output card to modulate hard pulses generated by GE Omega system. A high-speed phase ramp was used to produce frequency offsets for different slices. The results were compared with those generated directly by GE Omega system. Figure 6.10 shows that our system is capable of full modulation, such as used in Transmit SENSE.

Figure 6.9 Single Channel Imaging Results Before and After Calibration. The figure is shown in the next page. Gradient echo magnitude and phase images were taken before calibration (a) and (b) and following calibration (c) and (d). Each image was obtained from a single channel connected to a small birdcage coil were taken before (a and c) and after (b and d) system calibration. When imaging using a specific channel all other channels were set to zero. The calibration provided good uniformity in both amplitude and phase across channels, as quantified in the text. Note that the figure is masked to remove the background.

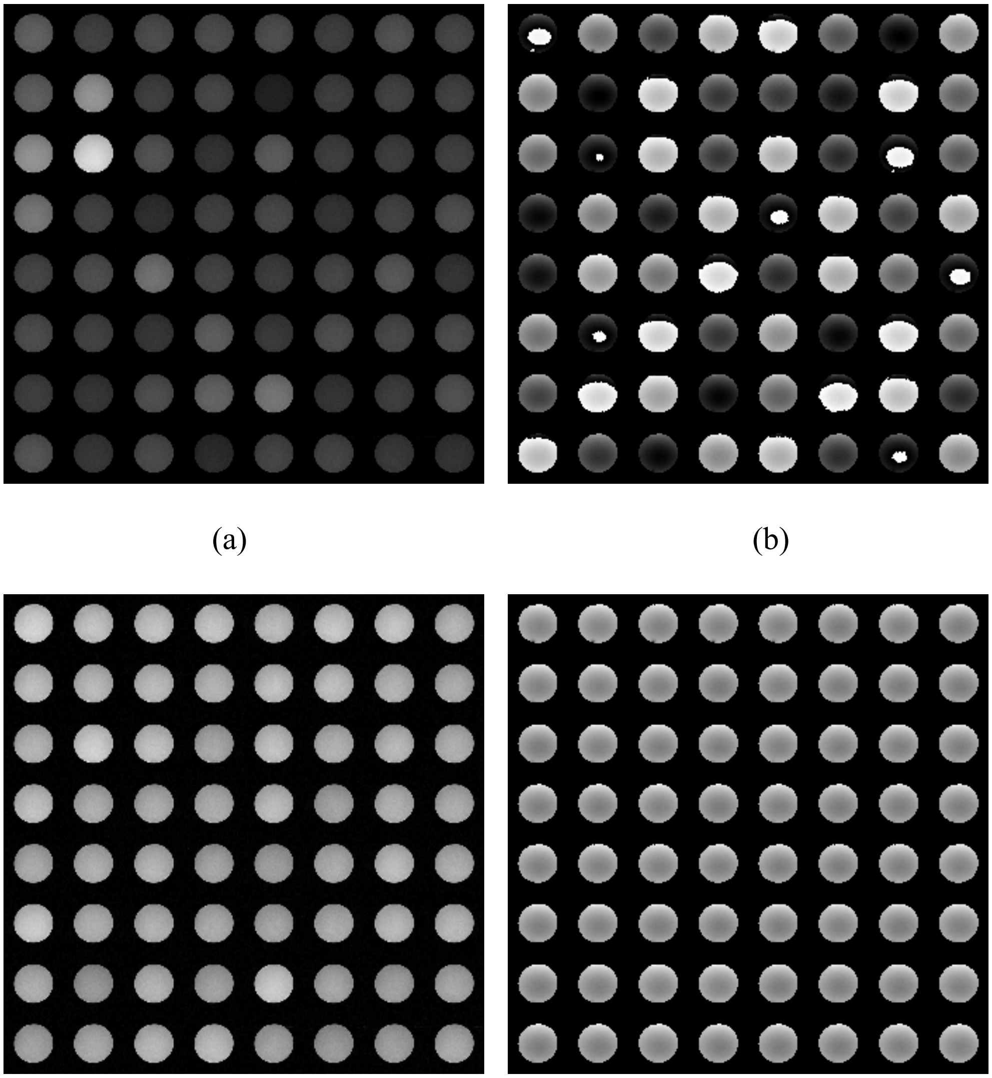

(a) (b)

(c) (d)

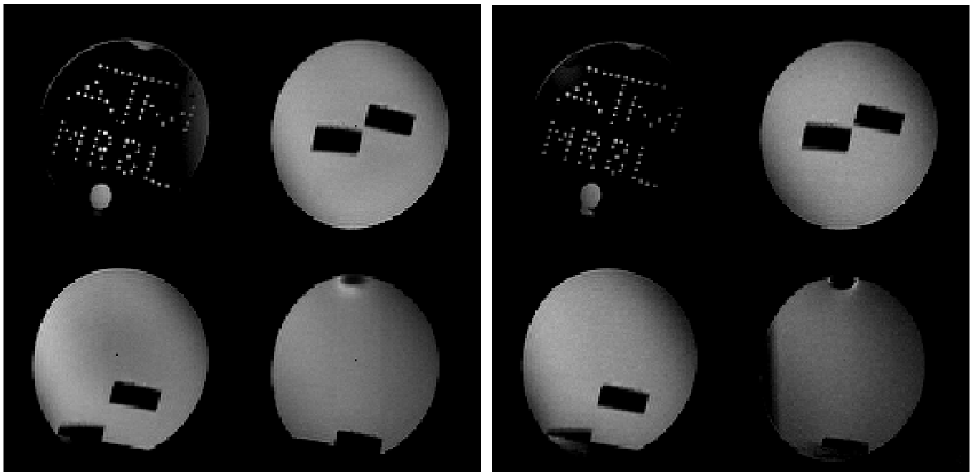

Figure 6.10 High Speed Modulation Multi-Slice Images Using Phase Ramps. The modulator board is fully capable of high speed RF waveform modulation. Simply by replacing the digital tuning board with high speed analog output board (NI PCI-6713). A sinc function together with different phase ramp was used to generate frequency offset in the slice selection direction. Result from our GE omega system modulator (left) is used for comparison purpose.

VI.9 Single Channel 2D Pulse for Dynamic Modulation

Dynamic control is demonstrated by generating a checkerboard excitation using a 2D transmit EPI pulse sequence. Images were taken using a single channel of the parallel system and a birdcage volume coil. The gradient goes through k-space line by line and the in-phase part of the RF signal is shown in Figure 6.11.

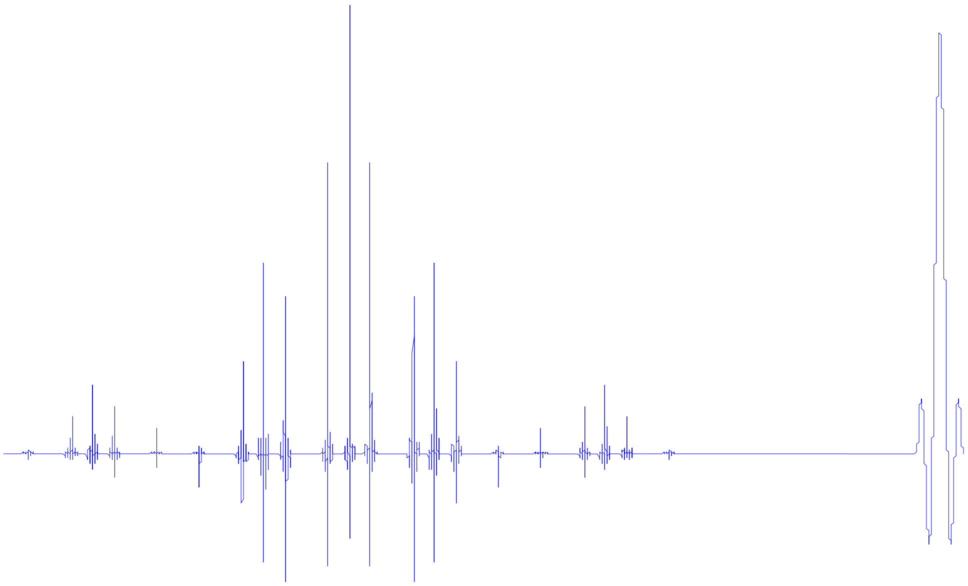

Figure 6.11 2D Pulse Used for Dynamic Modulation. As k-space is scanned line by line, the checker board pattern is transmitted and impressed onto the phantom. A slice selective 180 degree pulse is then used to flip the spins for a spin-echo image. Each peak on the left is approximately a sinc pulse. Stacked line by line, this is the Fourier transform of a checkerboard pattern

Images were taken by using the same pulse sequence with Varian Inova system for control and later one channel of the system. Results are shown in Figure 6.12. The two systems show good agreement with distortion resulting from shimming problems, and thus not indicating a flaw in the transmitter system. The results show that a single channel of the vector modulator and amplifier system is functionally equivalent to a commercial modulator, but the vector modulators are much easier to use when scaling up the number channels because they are smaller and lower cost.

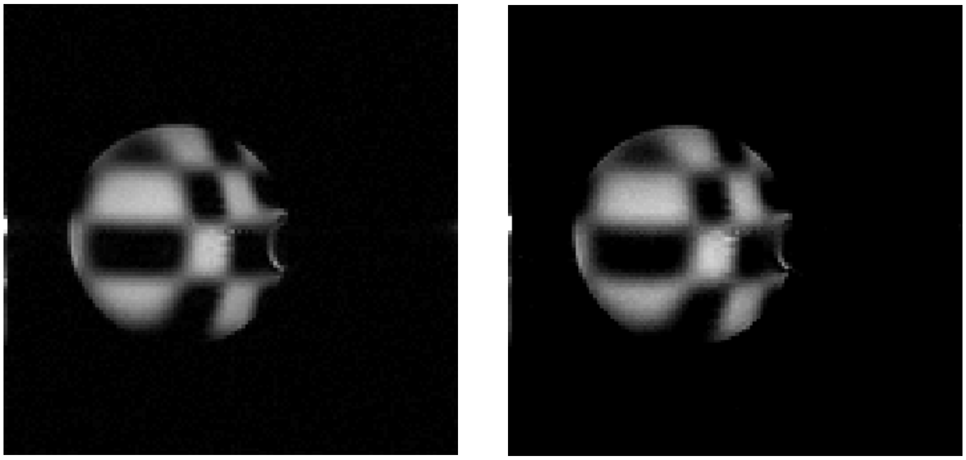

Figure 6.12 Comparison of 2D Pulse Imaging Results with Commercial Scanner and One Channel of the Parallel Transmitter. Agreement between the checkerboard excitation produced by a commercial modulator (left) and our vector modulator based system (right) is very good. Curvature and distortion is due to shimming, and is thus present in both images.

CHAPTER VII

PARALLEL TRANSMIT MR IMAGING TESTS AND RESULTS

Various MR imaging experiments are performed to show the capabilities of the TR SEA system. Many of them have been previously impossible without this this 64-channel parallel transmit system. Experimental setups and results are shown in this chapter.

VII.1 Eight-Channel In-Phase vs. Out-of-Phase Experiment

As a most simple experiment performed immediately after part of the system was constructed and tested, an eight-channel imaging test was performed before going to 64. This experiment uses a planar SEA array placed inside a parallel plate volume coil. The SEA array is used to transmit, while the volume coil is used for receiving. This is the same setup as described in Chapter V as reverse SEA. As predicted in the simulations, when neighboring channels have a phase shift of 180°, the transmitted field would be more uniform than when the phase shift is 0°. We are going to keep all the parameters to be identical, only changing the phase settings on the TR SEA Controller software GUI. These images were acquired using Varian Inova system. Sgems sequences were used for images in the coronal plane. The images as well as profiles of the images are shown in Figure 7.1.

Figure 7.1 Eight-Channel Parallel Transmit Experiment with Different Phase Shift Across Nearest Neighbors. The figure is shown in the next page. The first row is 180 degree phase across nearest neighbors and the second row is for 0 degree phase shift across nearest neighbors. The first column is for actual images and the second column is for the profile, i.e., horizontal sum of the images. Clearly noticeable is that with the phase shift, images get more uniform. Blurred area on the right side of the images was cause by the transmission lines not properly grounded, but it does not affect the image area. (c) looks wider than (a) because the excitation is less efficient and energy coupled into the neighbors have more effects. If shown in the same scale, (c) will appear much darker than (a).

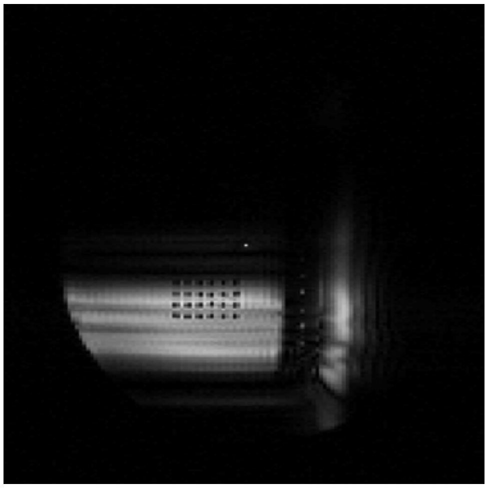

(a)

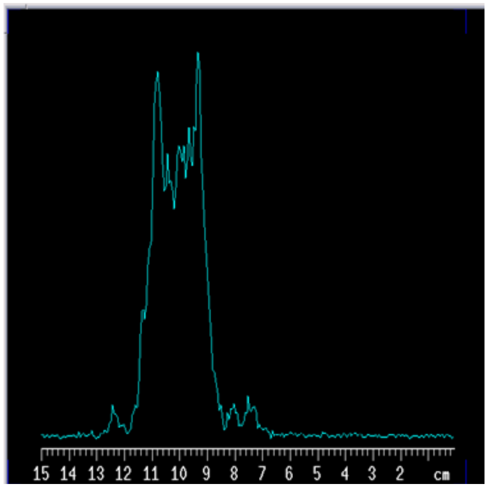

(b)

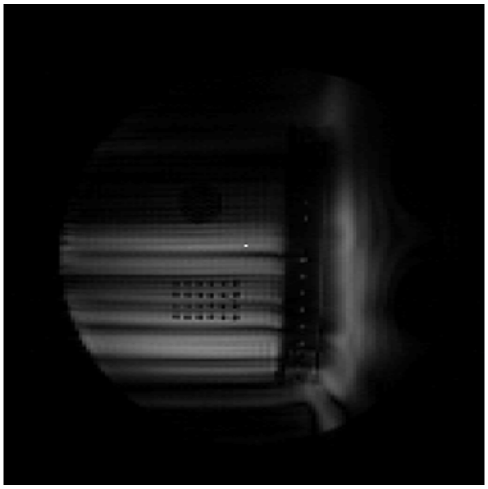

(c)

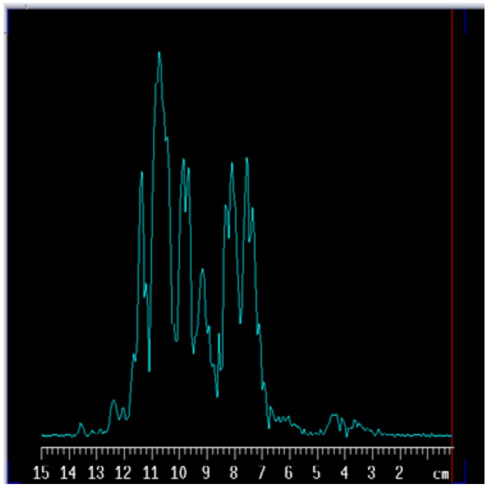

(d)

VII.2 Moving Slice with Power or Transmit Time Ramp

Using a uniform phantom and by varying the transmit power or time, the excitation band can be moved up or down. In this experiment, a standard Varian Ssems sequence is used. SEA array is for transmitting 90 degrees pulses and parallel plate volume coil is for transmitting 180 degrees pulses and receiving. Transmit power is ramped to observe the transmit pattern. Figure 7.2 shows the imaging results.

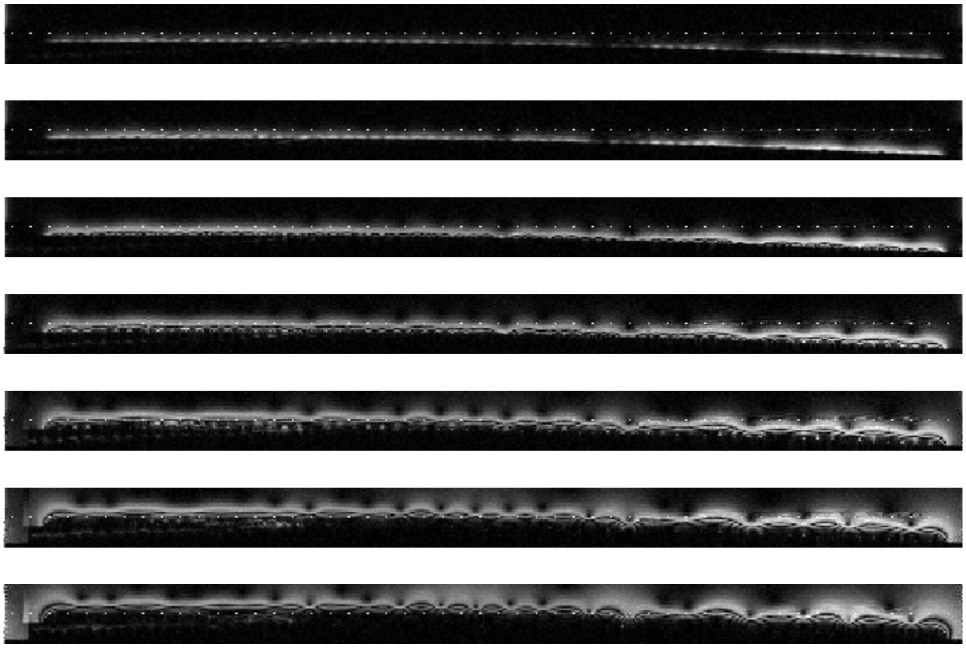

Figure 7.2 Moving Slice of Excitation Using Different Transmit Power. From top to bottom, the transmit power is increased by 6dB for each. The bottom one being 2mS hard pulse for 100W per channel. Dotted line is for reference and not artifact in the image.

VII.3 Slice Selection without Gradient

With the slice selection effects discussed in the previous section, one interesting application of the parallel transmitter is using the transmitter to do slice selection near the coil array. As predicted by the simulations, by varying the transmit power, it is possible that the slice selection is manipulated in a limited range.

In the first experiment, the planar array is used. A phantom was made using 1g/L $CuSO_4$ filled agarose gel. Plastic sheets with negative text, each with about 0.7mm thickness are stacked from the bottom of the phantom. The bottom of the phantom is placed above the SEA array with about 1mm of gam. Letters of “seamri” are included from the bottom of the array. A SEA array was used for transmitting 90° pulses and a parallel plate coil is used for both 180° pulses and receiving. Note that although we call it 90° here, actual flip angles vary with locations because of the fall off nature of the planar pair coils.

A standard Ssems pulse sequence is used. The slice selection gradient is turned off by forcing gss = 0 in the pulse sequence. Alternatively, the slice thickness can be set to the maximum allowed value, which is 1km, effectively removing slice selection gradient. Images were taken using 4ms gauss pulses. Neighbor phase offset was set to 180°. Power was set to be 100W and 25W. The images are shown in Figure 7.3.

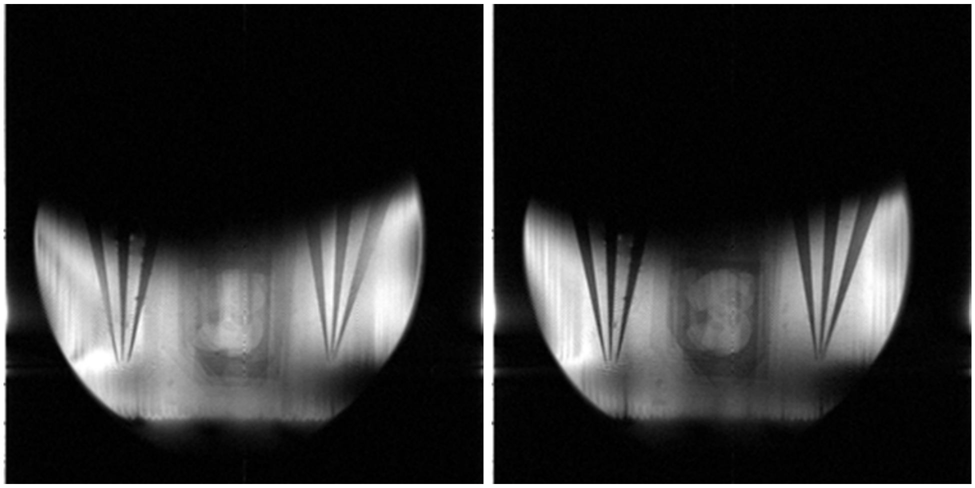

Figure 7.3 Slice Selection without Gradient. The figure on the left and right were acquired using 100W and 25W respectively. The figure on the left shows a letter “r”, while right one shows “s”, indicating a slice selection offset of about 2.8mm.

The same experiment is done for cylindrical case as well. A double-layered phantom was designed and constructed, thanks to Wen-Yang Chiang. A sketch is shown in Figure 7.4. The first layer and second layer are both spirals but in different directions. The phantom has a diameter of 89mm, with length of 72mm. Coil to first layer of phantom distance is 1.8mm. Thickness of first layer (near layer) of the spiral is 1.3mm while for the second layer (far layer) of the spiral is 3.9mm. The images acquired for both layers are shown in Figure 7.5.

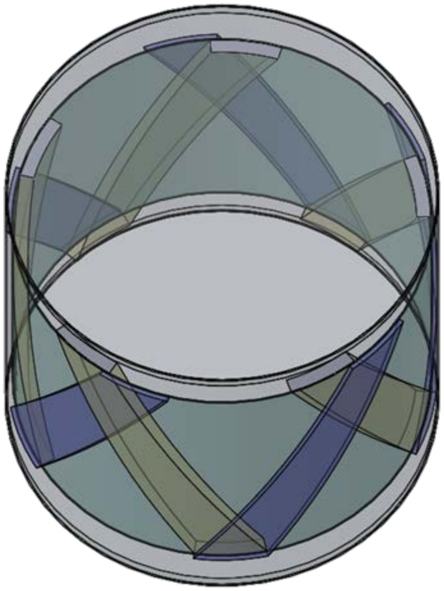

Figure 7.4 Double Layered Phantom. This phantom was constructed using 3.5 in diameter Smart^{TM} water bottle and double sided tapes for the spirals.

VII.4 TR SEA Imaging of Static Phantom on a Cylinder

As a first TR SEA imaging, a static phantom is used. Please note that the procedure here is primitive. A more improved and detailed description can be found in the next section of this dissertation. In this experiment, a flexible SEA coil array is wrapped around the surface to be imaged, as shown in Figure 7.6.

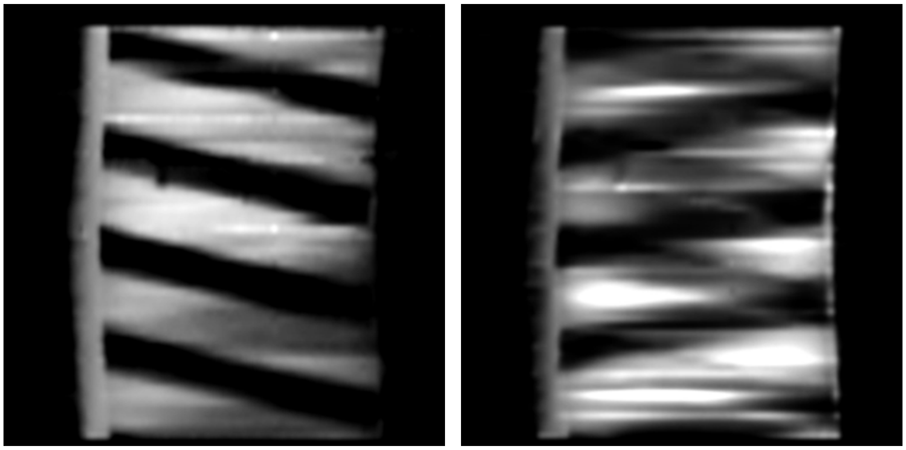

Figure 7.5 Cylindrical Surface TR SEA with Different Depth. With increased transmit power, saturation band is created at near surface, effectively imaging a deeper surface. Resolution=64x128. FOV=10x26 cm. TE: 2.66ms. Pulse: 0.5ms hard. Spectral width: 100kHz. Acquisition time: 1.28ms. Power increase: 22dB. Phase ramp: 150°(near), 60°(far).

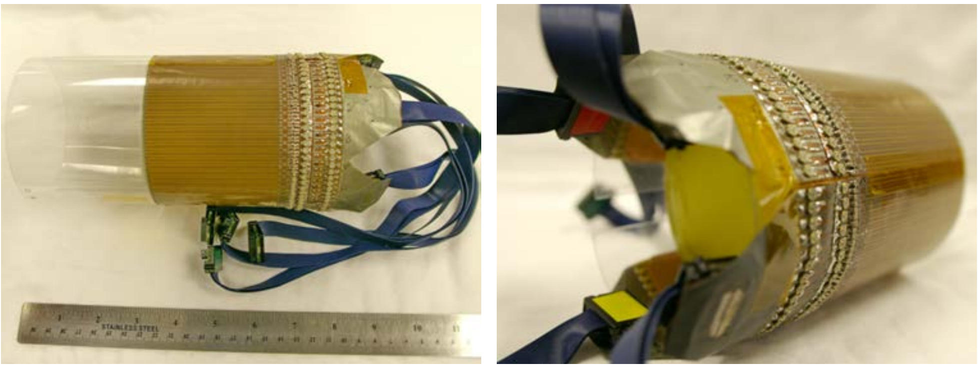

Figure 7.6 Flexible SEA Coil Array Wrapped around a Cylindrical Shaped Uniform Phantom.

To verify the transmit pattern, a birdcage volume coil is used for an initial image in axial slice. The setup is the same as reverse SEA discussed in Chapter V. Note that this transmit pattern does not require gradient involved, it is just with a single shot. The transmitted patter is shown in Figure 7.7.

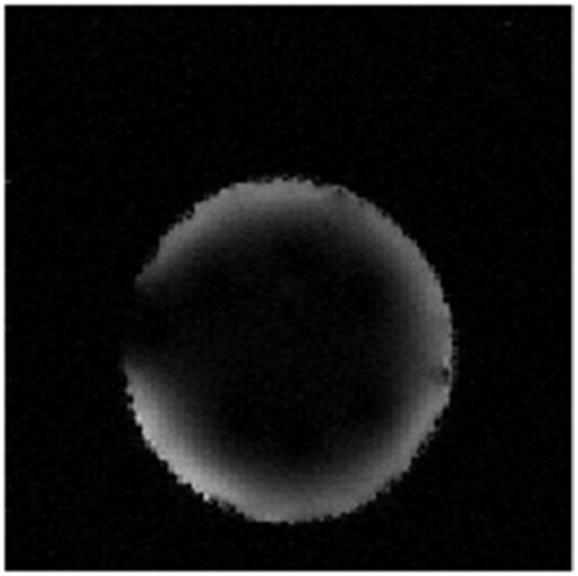

Figure 7.7 Axial Image Showing the Transmitted Pattern Using Reverse SEA Setup.

After the transmitter part is verified, TR SEA mode is used. A single shot for the curved slice excitation followed by a single echo using the 64-channel receiver yield an MR image on that curved surface. The image was acquired using a Varian Sgems sequence. Phase encoding is no longer necessary because it is replaced by the localization of the coils. In fact, there is no easy way to do it if it is desired in the curved slice. Removal of phase encoding was done by telling the Varian Inova MR scanner to acquire profiles instead of pictures. Slice selection during transmit is supposed to be a cylindrical shape in the phantom, but we simply do not want it because the coil pattern for transmit and receive is already there. The simple way to remove slice selection was to set the slice thickness to 1000 meters, which is the maximum allowed by the scanner. This way, it effectively removes the slice selection gradient. A screen shot of the gradient monitoring oscilloscope is shown in Figure 7.8.

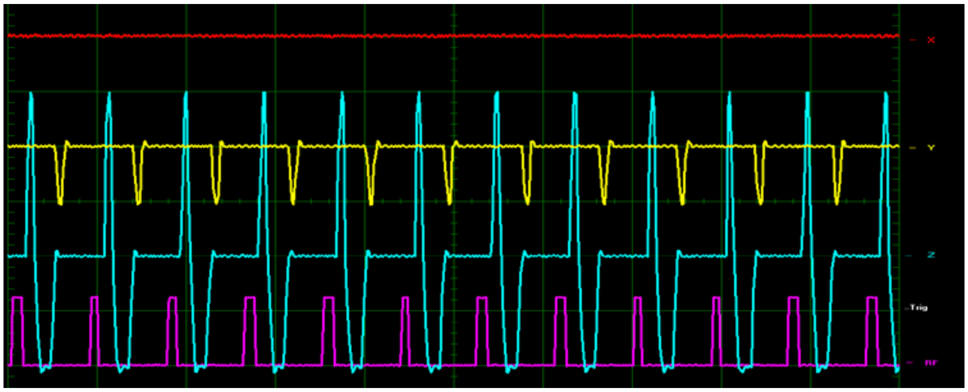

Figure 7.8 Unmodified Ssems Pulse Sequence for TR SEA Image. By simply setting the scanner to coronal slice, 1E6 mm (1km) slice thickness and set to acquire profile in Sgems sequence, the gradient would work the way we desire. Note the y gradient which is yellow colored in the picture. Ideally it should be all zeros, but they are not here. This is the crusher gradient, which is not necessary in our case. It will be removed later in the next experiment to allow shorter TR. Here TR = 8.8mS. Later TR = 5mS became possible.

Using the above setup and pulse sequence, an image is acquired, which is shown in Figure 7.9.

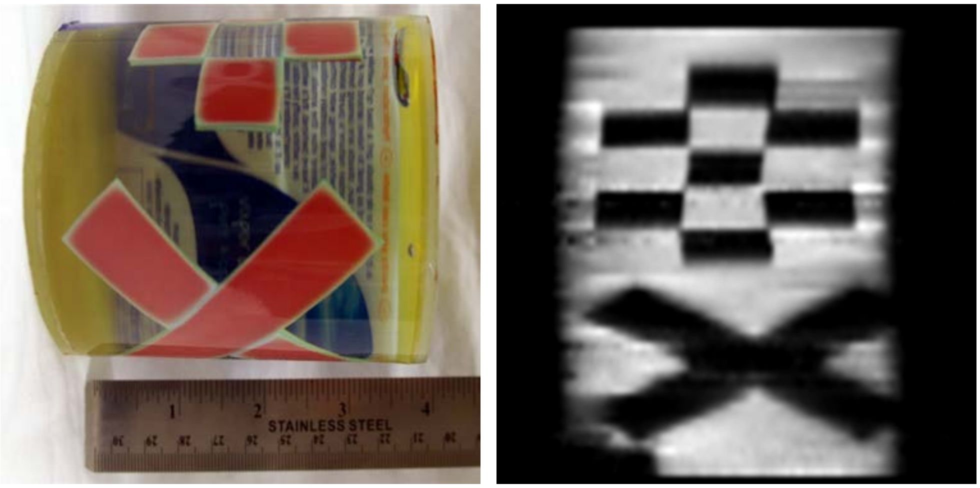

Figure 7.9 TR SEA Image of Surface of a Cylindrical Phantom, Single Shot Curved Slice Excitation and Single Echo Receiving. The phantom has a rectangle and three squares are attached to the inside of a cylindrical water container at random locations. Bottom left dark was caused by a bubble in the phantom.

VII.5 TR Signal Optimization

The *straightwires* class works for general Biot-Savart magnetic field calculations discussed in Chapter V is used to predict the optimal SNR for TR SEA.

Using theory of reciprocity, Hoult derived and clearly explained the received signal strength [36]:

$$\xi = 2\omega M_0 \sin(\gamma\tau|B_1^+|)\frac{-i\, B_1^+}{|B_1^+|}\widehat{B_1^-}$$

In our T/R simulations, we shall combine four constants, γ, τ, $-i$ and the constant to multiply to $\widehat{B_1^+}$ to get B_1^+, into one constant, V, which is proportional to the square root of the excitation power. We will simply remove $2\omega M_0$ and $-i$ term to get relative signal strength. Please note that the relatively signal strength calculated this way would still be complex, containing phase. This is very important because when we do TR SEA or any other imaging method where voxel size is comparable to coil size, the total signal received is the complex scalar sum of all small parts where the signal can be considered as in phase. Our signal would be

$$\text{Relative Signal Strength} = \sin\left(V\left|\widehat{B_1^+}\right|\right)\frac{\widehat{B_1^+}}{\left|\widehat{B_1^+}\right|}\widehat{B_1^-}$$

In a TR array, the $\widehat{B_1^+}$ field shall be calculated using the array because the excitation of the spins can be contributed from all coils, while $\widehat{B_1^-}$ field shall be calculated using a single channel. Using this theory, the received signal strength is calculated for the total volume of the phantom, which is a given distance from the array, using both phase and magnitude sweeps. Using the cylindrical setup shown in Chapter V, images were acquired using the same sweep. The results of simulations and images were shown in Figure 7.10. By varying the transmit power and phase offset, the images signal to noise ratio can be improved significantly. The slight disagreement might come from the fact that in the simulations, many factors were not considered, such as couplings and current distributions in the coil elements.

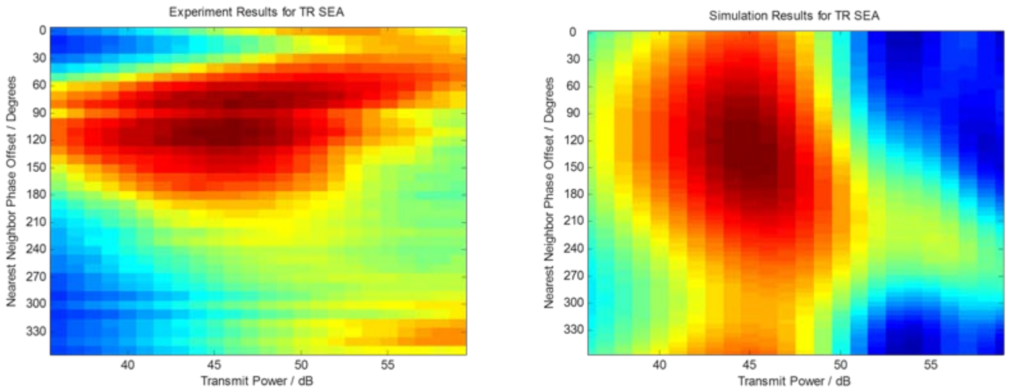

Figure 7.10 Transmit / Receive Signal Strength as a Function of Power and Phase Ramp Sweep. The coil to phantom distance was set to be 0.8mm for both simulations and experiments. The signal is considered to be contributed from all regions of the phantom.

VII.6 Cylindrical Rotational Phantom TR SEA Imaging

An interesting application is using the TR SEA to image rapid moving objects on a curved surface. This kind of imaging has been impossible with R/O SEA array because of the requirement for different phase compensation gradient by each coil element. The speed requirement made other imaging method fail for such images.

In this experiment, the gradient echo sequence, Sgems on Varian Inova, is modified into Sgems_no_ss for higher speed imaging. Figure 7.11 shows screenshots on the gradient monitoring oscilloscope before and after the modification.

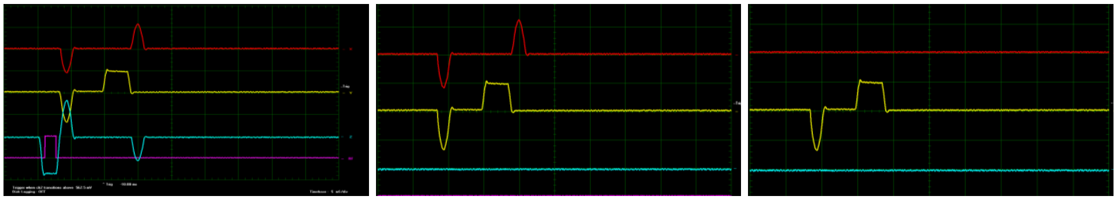

Figure 7.11 Gradient Echo Pulse Sequence Using Normal Parameters, Infinite Thickness and After Modification for TR SEA Imaging. Red trace is for phase encoding, yellow for frequency encoding, and cyan for slice selection (the y and z label in the screenshot is reversed). As mentioned in the previous experiment, the slice selection and crusher gradient are not necessary and will be removed for shorter TR. Pink colored RF for the first screen shot is on during the time z gradient is on for slice selection. For the other figures, it is on just before the gradient pulses. RF signal is not correctly shown because of a wrong connection as the time of the screenshot.

A cylindrical rotational phantom was made using “smart water” 1.5L bottles. 4 pieces of 1g/L $CuSO_4$ filled agarose gels are placed inside triangle shaped containers, and attached to the inside of the phantom. Figure 7.12 below shows the phantom, inside a flexible SEA coil array.

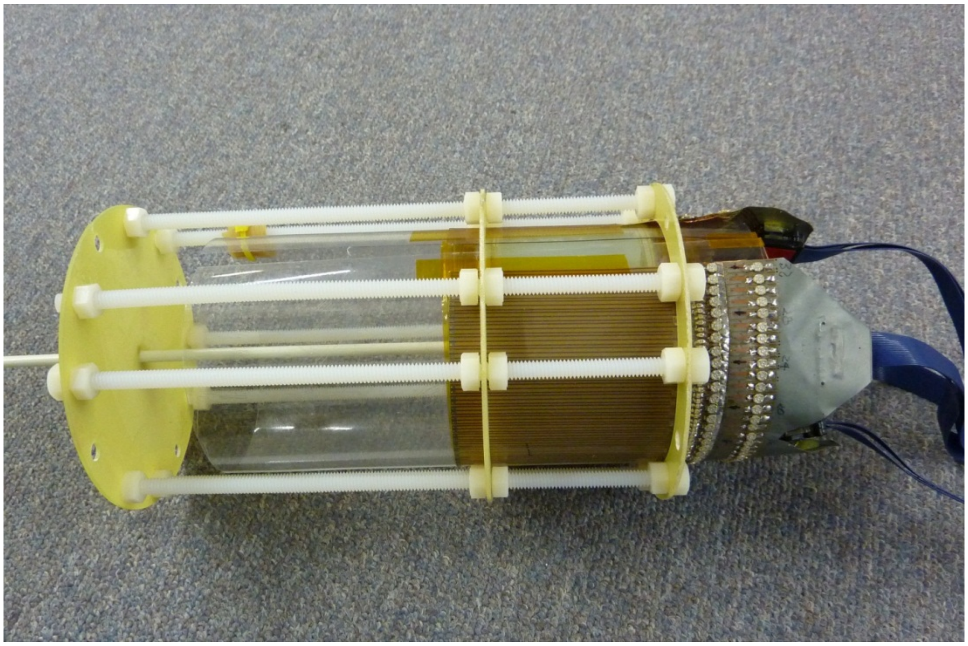

Figure 7.12 Rotational Cylindrical Phantom Inside a Flexible TR SEA Coil Array. The white rod in the center is used to drive the phantom for rotation.

The phantom needs a driver to make it rotate. A stepper motor, part number 5718X-01P, made by Lin Engineering is used to rotate the phantom. It is able to provide a maximum torque of 0.71Nm, eliminating the necessity of extra gears for extra torque. Since the cylindrical phantom has a diameter of 3.5 inches, 16N rotational force is applied at the edge of the cylinder. That is equivalent to 3.6 pounds. A stepper motor controller / driver with part number R325, which is also made by Lin Engineering, is also used. It takes a single digital input to go one step. A digital square wave would make the stepper motor go by 1.8 degrees. In other words, a 200Hz square wave would generate a 1 revolution / second rotational speed. To use this setup, a function generator is normally used. Power supply should be set to 15V, with 2.8A current limit. The actual current depends on the load, which is normally only about 0.5 to 1A. A photo of the motor and the driver circuit is shown in Figure 7.13 below.

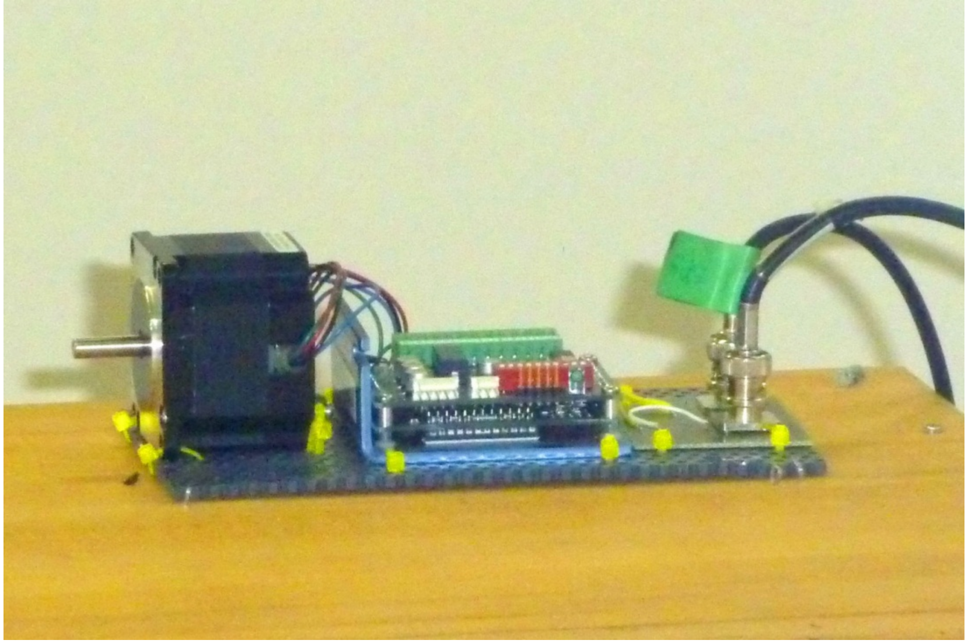

Figure 7.13 Stepper Motor and Driver Assembly for Rotational Phantom. A single digital pulse gives a single step in the stepper motor. Note that everything is stapled on a thick wood piece for added safety because this setup is only about 2m from the magnet, and the motor is, undoubtedly, very magnetic.

The experiment uses standard gradient echo sequence. Slice can be in coronal or sagittal, but for the VNMR system, coronal direction is used. Slice thickness is set to 1km, which effectively turns off the slice selection. Reason to prefer coronal instead of sagittal is because coronal image uses z as frequency encoding direction. If sagittal is used, swap phase and read is necessary.

Images were taken using 100 kHz spectral width, 128 frequency coding direction resolution. Ideally, larger receiver bandwidth can be used, but was limited to receiver side software issues. Transmit pulses are 1mS square shaped. As predicted in the simulations, 40 degrees across-neighbor phase shift gives the best penetration depth and so it is used.

The transmit power can be determined using an approach similar to fining the Ernst angle for fast gradient echo images. Because the transmit pattern is non-uniform, Ernst angle exists at all points, but with different values. If the transmit pattern is uniform, at Ernst angle, a maximum receiving signal will be received. Here, we are trying to get the maximum signal level. This is quite similar to Ernst angle but there are differences. On the receiver computer, the LabView Monitor that came with the ICS645 SDK, shown in Figure 7.14, is used in search of the “Ernst angle”. The signal strength is shown the FFT window on the bottom right side. The transmit power, tpwr1 on the Inova console, is stepped through until this signal strength value is maximized. The signal strength vs. tpwr1 is shown in Figure 7.15. Following this procedure, we are able to set the optimal input power. In this specific case, tpwr1 = 21, or about 0.5W per channel is the optimal input power.

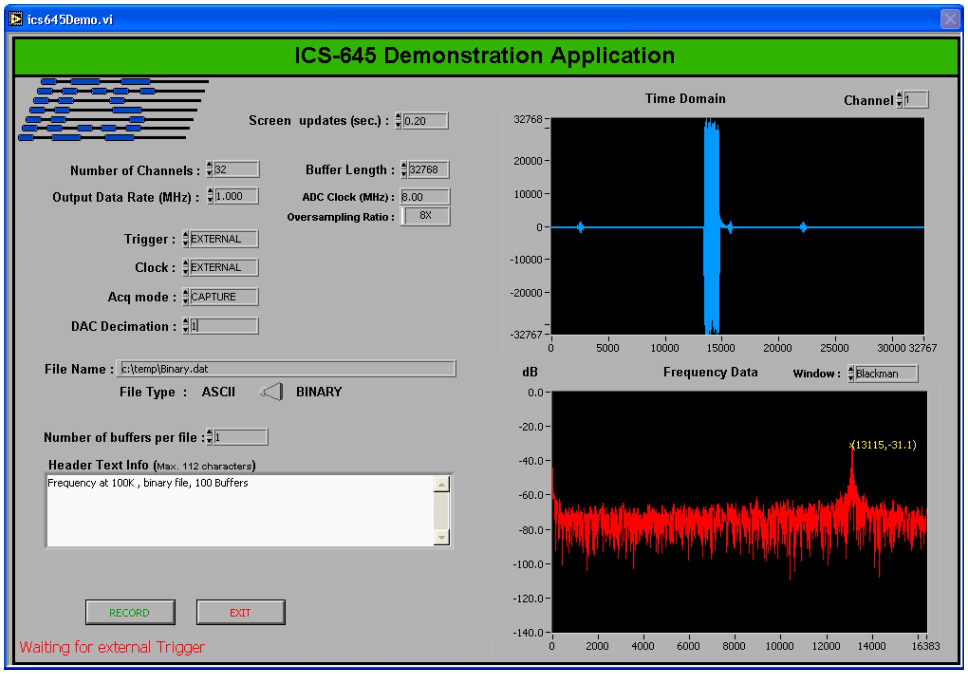

Screen updates (sec.) : 0.20

Number of Channels : 32

Buffer Length : 32768

Output Data Rate (MHz) : 1.000

ADC Clock (MHz) : 8.00

Oversampling Ratio : 8X

Trigger : EXTERNAL

Clock : EXTERNAL

Acq mode : CAPTURE

DAC Decimation : 1

File Name : c:\temp\Binary.dat

File Type : ASCII BINARY

Number of buffers per file : 1

Header Text Info (Max. 112 characters)

Frequency at 100K , binary file, 100 Buffers

Channel 1

Window : Blackman

Waiting for external Trigger

Figure 7.14 LabView Monitor Came with the ICS645 SDK Used to Find “Ernst Angle”. Using the settings on the left side, the signal in time domain (top right side) and frequency domain (bottom right side) are both shown. The maximum signal value in the frequency domain is indicated on the plot, which is used to generate the plot to get “Ernst angle” later to determine the transmit power later.

The Sgems pulse sequence from Varian is good for normal imaging, and can be used for TR SEA imaging. However, it needs to be carefully modified to accelerate TR SEA imaging. The y gradient here is unnecessary, and can be safely removed for shorter allowed TR.

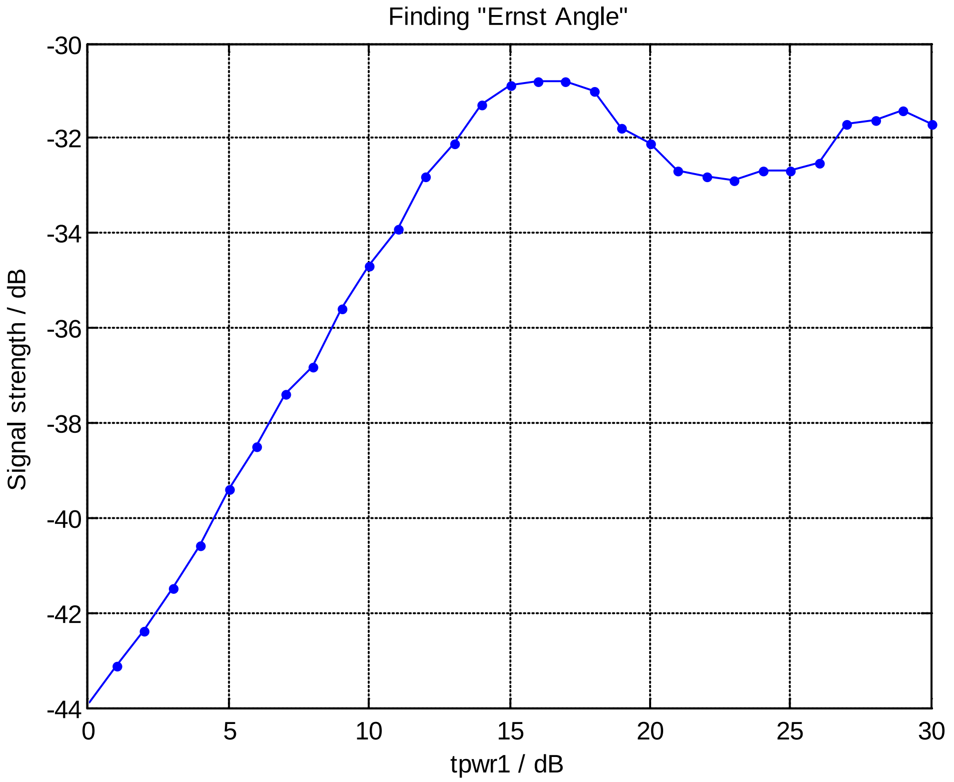

Figure 7.15 Signal Strength vs. Transmitted Power for TR SEA. As power goes up initially, the received signal strength goes up, as expect. However, it reaches the maximum point and begins to fluctuate. Because it is a more complicated spin system, the signal strength behavior is different than that of a simple gradient echo image using a normal MRI setup. The variation after reaching the “Ernst angle” is not that much, only about 2dB.

Using the above described experimental setup, images were acquired at 200 frames per second to form a movie of the rotation. A few frames of the movie is shown in Figure 7.16.

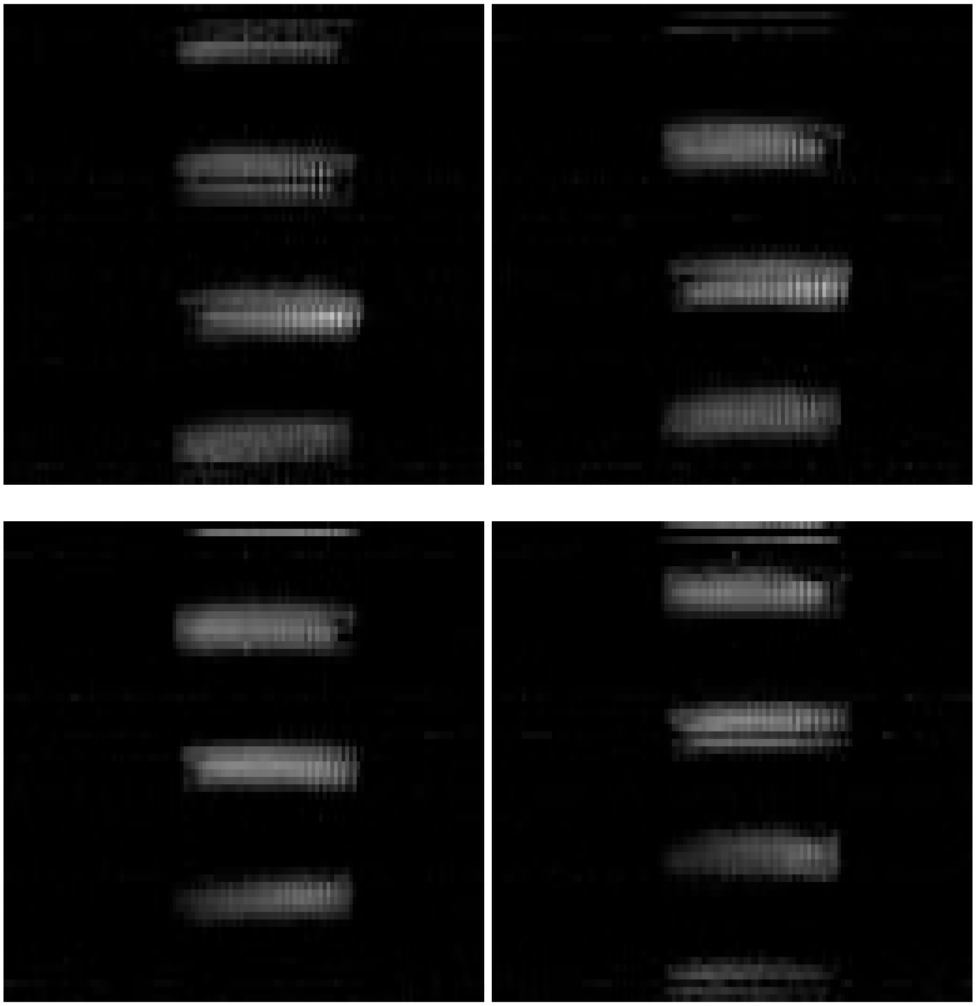

Figure 7.16 A Few Frames from a 200 Frames Per Second Movie Showing the Surface of a Rotational Phantom.

CHAPTER VIII

DISCUSSIONS AND CONCLUSIONS

While the system is built and tested and some TR images were taken, there are still other potential applications that are yet to be explored. Possible improvements are also discussed should another similar system is to be built.

VIII.1 Possible Improvements

If the system would ever be built again from scratch, there are hundreds if not thousands different things that could be improved, making the system very different from this implementation. This system was built in a lot of rush. Here are just a few examples of what could have been done better.

Many of the cables are made by new students without proper training and that caused a lot of problems. Combined with cold soldering joints, almost a whole year of time was wasted on debugging the system because many of the problems are intermittent. A couple of hundred bad cables were discovered, together with at least one hundred board failures caused by cold soldering points on circuit boards. While some of them are easy to find, many more gives intermittent problems and were difficult to debug. If the system was designed in a way to allow easy access to those debugging points which are already there but simply difficult to reach, the debugging process would be much easier.

The current implementation uses a large number of RF interconnects. This represents a large expense and number of potential failure points. Modifying the circuit board designs to eliminate cable runs to enclosure walls is one way of reducing the problem. It may also be possible to reduce the number of digital and DC power cables needed by changing the architecture of the subsystems. Manufacturability could also be improved by revising the board layouts. With care it may be possible to reduce the occurrence of cold and dry solder joints.

Using a microcontroller based control is also possible to replace the expensive NI DAQ system. This was investigated by Stang et al with successful result [46]. This would make the transmit SENSE system much more affordable in larger channels.

The output power, 100W for each channel, might not be enough for some applications. When fewer channels but more power is needed, it is possible to reconfigure the system to meet the requirement. Figure 8.1 shows a possible configuration for eight-channel, 800W per channel transmit SENSE system by adding a few modulators, RF power splitters and combiners.

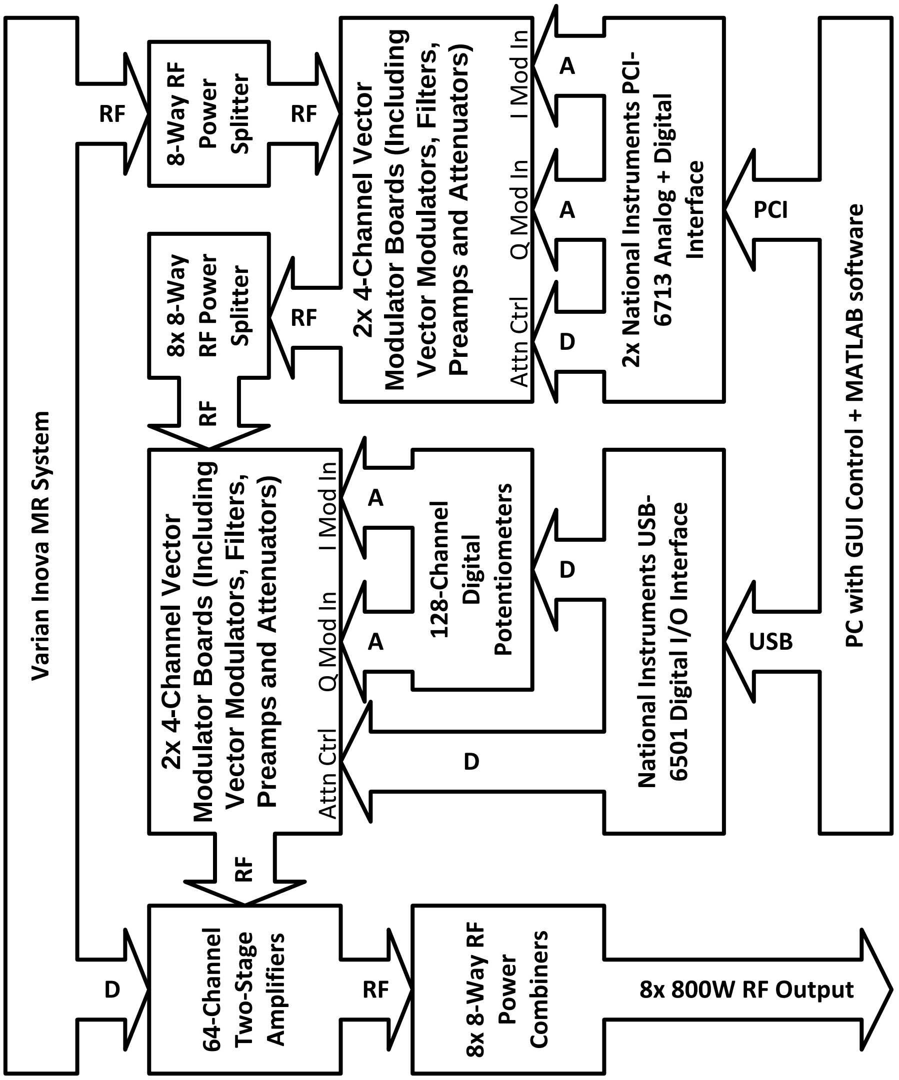

Figure 8.1 Channel Combining for Increased Power Level for Transmit SENSE. Using a few added components, it is possible to have an eight-channel parallel transmitter, with 800W per channel, by adding a few components.

Single channel transmitted pattern is shown in Figure 8.2. This pattern shows strong coupling. This image was made using a modified spin echo sequence, with 90°

pulses transmitted by a single SEA coil element, and 180° pulse by a volume coil. The receiving was done by the same volume coil. Measurements indicate that the coupling is mainly from the coil. The coupling between the neighboring channels was -12dB, while the transmitter has a coupling of -30dB. Using a current source would great reduce the coupling.

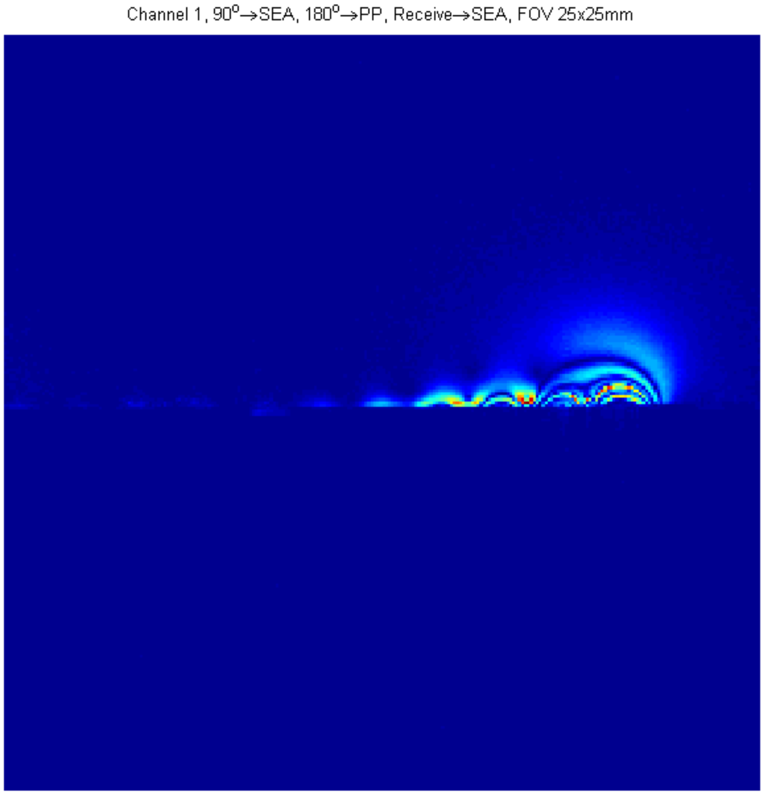

Channel 1, 90°→SEA, 180°→PP, Receive→SEA, FOV 25x25mm

Figure 8.2 Single Channel Transmitted Pattern Showing Coupling. Strong coupling is shown, which is mainly from coil and not the transmitter system.

VIII.2 Potential Application

The current implementation used planar pair arrays for the RF coil. Raised leg designed has been investigated in the past (McDougall et al, unpublished), and shows increased penetration depth and SNR. It can be used in TR SEA mode. Power requirement would decrease, making it possible to eliminate the expensive second stage amplifier.

The system is fully capable of B1 shimming for large arrays. By constructing a TEM array [38, 48], it is possible to build an array that functions similarly to a birdcage coil but with more accurate control for each rung. This would not only provide more uniform B1 field, but also removes the end ring.

Larger, flexible arrays could enable imaging of fast response BOLD signals on the surface of the brain[17]. T/R SEA could be used to capture this biological process. High speed flow imaging can be used for transient or non-periodic phenomenon such or chaotic flow, tissue tearing or cutting.

VIII.3 Conclusions

The existing SEA system was converted into T/R mode by adding a 64-channel parallel transmitter with independent amplitude and phase control of RF pulse for each channel. Requirement for phase compensation gradient in R/O SEA imaging is eliminated because phase departed during transmit is refocused during receiving, freeing the method to imaging on curved slices. The first 64-channel parallel transmitter for MRI in the world was constructed in this work, which includes both hardware and software for control of phase and amplitude for each channel through National Instruments DAQ system. Simulations and images were done to synthesize transmit patterns in a unique way for MRI. Testing results show that the system is capable of 100W per channel simultaneously for transmitting. Using this system, transmit field can be synthesized by varying the phase and amplitude across channel without traditionally required complicated pulse sequences involving simultaneous RF and gradient fields. Curved slice excitation has conventionally been considered a difficult task for MRI, achievable only through complicated pulses sequences. Using this system and flexible array wrapped around the subject to be imaged, the system is able to excite curved slice using one shot which has been traditionally considered very complicated. TR images indicate that the system is capable of high speed surface imaging at 200 frames per second following the surface of a flexible SEA array coil which has not been achieved using other methods in MRI.

REFERENCES

[1] J. Tsao, P. Boesiger, and K. P. Pruessmann, "k t BLAST and k t SENSE: dynamic MRI with high frame rate exploiting spatiotemporal correlations," *Magn. Reson. Med.,* vol. 50, pp. 1031-1042, 2003.

[2] S. M. Wright, M. P. McDougall, K. Feng, N. A. Hollingsworth, J. C. Bosshard, and C. W. Chang, "Highly parallel transmit / receive systems for dynamic MRI," in *31st Ann. Int. Conf. IEEE Eng. Med. Biol. Soc.*, Minneapolis, MN, 2009, pp. 4053-4056.

[3] V. Rasche, R. W. D. Boer, D. Holz, and R. Proksa, "Continuous radial data acquisition for dynamic MRI," *Magn. Reson. Med.,* vol. 34, pp. 754-761, 1995.

[4] D. K. Sodickson, “Massively parallel MRI,” in *Second International Workshop on Parallel MRI*, Zurich, Switzerland, 2004, pp. 64-65.

[5] D. K. Sodickson and W. J. Manning, "Simultaneous acquisition of spatial harmonics (SMASH): fast imaging with radiofrequency coil arrays," *Magn. Reson. Med.,* vol. 38, pp. 591-603, 1997.

[6] K. P. Pruessmann, M. Weiger, M. B. Scheidegger, and P. Boesiger, "SENSE: sensitivity encoding for fast MRI," *Magn. Reson. Med.,* vol. 42, pp. 952-962, 1999.

[7] M. A. Griswold, P. M. Jakob, R. M. Heidemann, M. Nittka, V. Jellus, J. Wang, B. Kiefer, and A. Haase, "Generalized autocalibrating partially parallel acquisitions (GRAPPA)," *Magn. Reson. Med.,* vol. 47, pp. 1202-10, 2002.

[8] M. A. Griswold, P. M. Jakob, M. Nittka, J. W. Goldfarb, and A. Haase, "Partially parallel imaging with localized sensitivities (PILS)," *Magn. Reson. Med.,* vol. 44, pp. 602-609, 2000.

[9] J. A. Bankson and S. M. Wright, "Simulation-based investigation of partially parallel imaging with a linear array at high accelerations," *Magn. Reson. Med.,* vol. 47, pp. 777-786, 2002.

[10] Y. Jiraraksopakun, M. P. McDougall, S. M. Wright, and J. Ji, "A regularized flow quantification method using MRI tagging and Single Echo Acquisition imaging," in *30th Ann. Int. Conf. IEEE Eng. Med. Biol. Soc.*, Vancouver, Canada, 2008, pp. 3397-3400.

[11] S. M. Wright and M. P. McDougall, "Single echo acquisition MRI using RF encoding," *NMR Biomed.*, vol. 22, pp. 982-993, 2009.

[12] S. M. Wright, M. P. McDougall, and D. G. Brown, "Single echo acquisition of MR images using RF coil arrays," in *24th Ann. Int. Conf. IEEE Eng. Med. Biol. Soc.*, Houston, TX, 2002, pp. 1181-1182.

[13] J. Reilly, "Peripheral nerve stimulation by induced electric currents: exposure to time-varying magnetic fields," *Med. Biol. Eng. Comput.,* vol. 27, pp. 101-110, 1989.

[14] C. Ham, J. Engels, G. Van de Wiel, and A. Machielsen, "Peripheral nerve stimulation during MRI: effects of high gradient amplitudes and switching rates," *J. Magn. Reson. Imag.,* vol. 7, pp. 933-937, 1997.

[15] E. Amparo, C. Higgins, D. Farmer, G. Gamsu, and M. McNamara, "Gated MRI of cardiac and paracardiac masses: initial experience," *Am. J. Roentgenology,* vol. 143, p. 1151, 1984.

[16] J. Pirolo, B. Branham, L. Creswell, W. Perman, M. Vannier, and M. Pasque, "Pressure-gated acquisition of cardiac MR images," *Radiology,* vol. 183, p. 487, 1992.

[17] S. Ogawa, T. M. Lee, A. S. Nayak, and P. Glynn, "Oxygenation-sensitive contrast in magnetic resonance image of rodent brain at high magnetic fields," *Magn. Reson. Med.,* vol. 14, pp. 68-78, 1990.

[18] S. M. Wright, M. P. McDougall, and D. G. Brown, "Single echo acquisition (SEA) MR imaging," in *Proc. 11th Sci. Mtg., Int. Soc. Magn. Reson. Med.*, Toronto, Canada, 2003, p. 23.

[19] M. P. McDougall, "Single echo acquisition magnetic resonance imaging," PhD Dissertation, Electrical Engineering, Texas A&M University, College Station, TX, 2004.

[20] M. P. McDougall and S. M. Wright, "64-channel array coil for single echo acquisition magnetic resonance imaging," *Magn. Reson. Med.,* vol. 54, pp. 386-392, 2005.

[21] S. Wright and M. McDougall, "MR Imaging at Sub-millisecond frame rates," in *Proc. 17th Sci. Mtg., Int. Soc. Magn. Reson. Med.*, Honolulu, HI, 2009, p. 3026.

[22] M. P. McDougall and S. M. Wright, "Overcoming phase effects of voxel-sized coils in planar and cylindrical arrays," in *26th Ann. Int. Conf. IEEE Eng. Med. Biol. Soc.,* San Francisco, CA, 2004, pp. 1060-1013.

[23] M. McDougall and S. Wright, "Coil phase compensation for single echo acquisition (SEA) imaging," in *Proc. 17th Sci. Mtg., Int. Soc. Magn. Reson. Med.*, Kyoto, Japan, 2004, P. 330.

[24] D. G. Brown, "Instrumentation for parallel magnetic resonance imaging," PhD Dissertation, Electrical Engineering, Texas A&M University, College Station, TX, 2005.

[25] D. G. Brown, M. P. McDougall, and S. M. Wright, "A receiver design for parallel imaging with large arrays," in *Proc. 10th Sci. Mtg., Int. Soc. Magn. Reson. Med.*, Honolulu, HI, 2002, p. 863.

[26] S. Wright, M. McDougall, and N. Yallapragada, "Rapid flow imaging using single echo acquisition MRI," in *Proc. 13th Sci. Mtg., Int. Soc. Magn. Reson. Med.*, Miami Beach, FL, 2005, p. 289.

[27] S. M. Wright, M. P. McDougall, and J. C. Bosshard, "Progress in visualizing turbulent flow using single-echo acquisition imaging," in *28th Ann. Int. Conf. IEEE Eng. Med. Biol. Soc.*, New York, NY, 2006, pp. 4877-4880.

[28] N. Yallapragada, "A 64-channel personal computer based image reconstruction system and applications in single echo acquisition magnetic resonance elastography and ultra-fast magnetic resonance imaging," PhD Dissertation, Electrical Engineering, Texas A&M University, College Station, TX, 2008.

[29] J. Bosshard, N. Yallapragada, M. McDougall, and S. Wright, "High Speed MR Elastography Using SEA Imaging," in *Proc. 16th Sci. Mtg., Int. Soc. Magn. Reson. Med.*, Toronto, Canada, 2008, p. 831.

[30] M. McDougall, J. Knight, E. Eigenbrodt, S. Wright, and C. Chang, "A simple approach to overcoming mutual coupling effects in some transmit array coils for magnetic resonance imaging," in *30th Ann. Int. Conf. IEEE Eng. Med. Biol. Soc.*, Vancouver, Canada 2008, pp. 2043-2046.

[31] M. P. McDougall, S. M. Wright, and D. G. Brown, "A 64 channel planar RF coil array for parallel imaging at 4.7 tesla," in *Proc. 16th Sci. Mtg., Int. Soc. Magn. Reson. Med.*, Toronto, Canada, 2008, p. 472.

[32] S. M. Wright, D. B. Brown, and M. P. McDougall, "Magnetic Resonance Imaging Using a Reduced Number of Echo Acquisitions," US Patent 6771071 B1, 2004.

[33] M. P. McDougall and S. M. Wright, "Investigation of coil phase compensation in 3D imaging at very high acceleration factors," *J. Magn. Reson. Imag.,* vol. 25, pp. 1305-1311, 2007.

[34] M. P. McDougall and S. M. Wright, "Phase compensation in single echo acquisition (SEA) imaging: phase effects of voxel-sized coils in planar and cylindrical arrays," *IEEE Eng. Med. Bio. Soc. Mag.*, vol. 24, pp. 17-22, 2005.

[35] J. S. Hyde, W. Froncisz, A. Jesmanowicz, and J. B. Kneeland, "Planar-pair local coils for high-resolution magnetic resonance imaging, particularly of the temporomandibular joint," *Med. Phys.,* vol. 13, pp. 1-7, 1986.

[36] D. Hoult, "The principle of reciprocity in signal strength calculations - a mathematical guide," *Concept. Magn. Reson.,* vol. 12, pp. 173-187, 2000.

[37] J. R. Keltner, J. W. Carlson, M. S. Roos, S. T. S. Wong, T. L. Wong, and T. F. Budinger, "Electromagnetic fields of surface coil in vivo NMR at high frequencies," *Magn. Reson. Med.,* vol. 22, pp. 467-480, 1991.

[38] J. T. Vaughan, H. P. Hetherington, J. O. Otu, J. W. Pan, and G. M. Pohost, "High frequency volume coils for clinical NMR imaging and spectroscopy," *Magn. Reson. Med.,* vol. 32, pp. 206-218, 1994.

[39] A. Kangarlu, B. A. Baertlein, R. Lee, T. Ibrahim, L. Yang, A. M. Abduljalil, and P. M. L. Robitaille, "Dielectric resonance phenomena in ultra high field MRI," *J. Comp. Assist. Tomogr.,* vol. 23, p. 821, 1999.

[40] D. Hoult, "Sensitivity and power deposition in a high-field imaging experiment," *J. Magn. Reson. Imag.,* vol. 12, pp. 46-67, 2000.

[41] J. Vaughan, L. DelaBarre, C. Snyder, M. Garwood, G. Adriany, P. Bolan, C. Akgun, J. Strupp, P. Andersen, and P. van de Moortele, "How to do RF at high fields," in *Int. Soc. Magn. Reson. Med. Workshop*, Miami, FL, 2005.

[42] F. Schick, "Whole-body MRI at high field: technical limits and clinical potential," *Eur. Radio.,* vol. 15, pp. 946-959, 2005.

[43] P. Cunningham, M. Law, and M. Schweitzer, "High-field MRI," *Orthop. Clin. North Am.,* vol. 37, p. 321, 2006.

[44] E. Boskamp, "Transmit and Receive RF Subsystems," *Int. Soc. Magn. Reson. Med. Workshop*, Kyoto, Japan, 2004.

[45] G. Scott, P. Stang, W. Overall, A. Kerr, and J. Pauly, "A Vector Modulation Transmitt Array System," in *Proc. 15th Sci. Mtg., Int. Soc. Magn. Reson. Med.*, Seattle, WA, 2006, p. 128.

[46] P. Stang, A. Kerr, J. Pauly, and G. Scott, "An extensible transmit array system using vector modulation and measurement," in *Proc. 16th Sci. Mtg., Int. Soc. Magn. Reson. Med.*, Toronto, Canada, 2008, p. 145.

[47] S. K. Singh, *Magnetic field due to current in straight wire*, Connexions, Sept. 2009. [Online]. Available: http://cnx.org/content/m31103/latest/ [Accessed: 28 July 2011].

[48] G. Adriany, P. Van de Moortele, J. Ritter, S. Moeller, E. Auerbach, C. Akgun, C. Snyder, T. Vaughan, and K. Ugurbil, "A geometrically adjustable 16-channel transmit/receive transmission line array for improved RF efficiency and parallel imaging performance at 7 Tesla," *Magn. Reson. Imag*, vol. 59, pp. 590-597, 2008.

VITA

Ke Feng received his Bachelor of Science degree in physics from Shandong University at Jinan, China in June 2001. He joined the Physics Department at Texas A&M University in September 2002 and received his Master of Science degree in December 2005. Afterward, he joined the Electrical and Computer Engineering Department at Texas A&M University and received his Doctor of Philosophy degree in August 2011. His research interests include MRI system hardware and software design and testing as well as simulations for transmit and receive arrays.

Dr. Feng can be reached at C/O Steven M. Wright, Electrical and Computer Engineering, Texas A&M University, College Station, TX 77843-3128. He can also be reached by email: jnfengke@gmail.com.